THESIS FOR THE DEGREE OF LICENTIATE OF ENGINEERING

Astrochemical Investigations of Complex Organics in Cold Molecular Cloud Cores

Tadeus Carl

CHALMERS
UNIVERSITY OF TECHNOLOGY

Department of Space, Earth and Environment
Chalmers University of Technology
Gothenburg, Sweden, 2024

Astrochemical Investigations of Complex Organics in Cold Molecular Cloud Cores

Tadeus Carl

Front cover image: Carina Nebula by JWST
Credit: `science.nasa.gov/mission/webb/multimedia/images/`
Date of retrieval: 14 February 2024

This thesis has been prepared using LaTeX.

Department of Space, Earth and Environment
Chalmers University of Technology
SE-412 96 Gothenburg, Sweden
Phone: +46 (0)31 772 1000
`www.chalmers.se`

Printed by Chalmers Reproservice
Gothenburg, Sweden, February 2024

"Everything existing in the universe is the fruit of chance and necessity."

- Democritus (460 – 370 BC)

Abstract

Astrochemistry is the study of the formation and evolution of molecules in the interstellar medium (ISM) of the Milky Way and other galaxies. Molecules start to accumulate in the coldest and densest regions of the ISM, namely molecular clouds, and as of this date, 307 interstellar molecules are identified. The major focus of this thesis is on a particular group of interstellar molecules, so-called complex organic molecules (COMs), i.e., carbon-bearing molecules composed of at least six atoms. Interstellar COMs and other molecules are studied by a combination of observations, experiments, and models, with the focus of this thesis being on observations. Another focus will be on observations of COMs in very cold ($< 10\,\mathrm{K}$) and dense ($> 10^5\,\mathrm{cm}^{-3}$) molecular cloud regions.

This thesis is separated into two parts: part I is giving an overview about various important concepts and methods related to the detection, identification, and analysis of interstellar molecules (chapters 1 – 4), and part II is presenting the published paper this thesis is based on. Chapter 1 provides some background to my motivation to obtain a degree in astrochemistry, and to some basic concepts related to the formation of interstellar molecules. Some fundamental physical concepts widely used throughout this work will be introduced in that chapter as well. Chapter 2 introduces some important concepts and methods related to the derivation of molecular abundances from radio astronomical observations. Chapter 3 then gives a brief summary of the published paper this thesis is based on. Lastly, chapter 4 introduces some currently running and future projects (which I am part of) with the goal to add to the overall understanding of COM formation in the cold ISM.

Keywords: ISM – molecules, ISM – molecular clouds, dark clouds, astrochemistry, astrobiology

List of Publications

This thesis is based on the following publications:

[A] **Tadeus Carl**, Eva S. Wirström, Per Bergman, Steven B. Charnley, Yo-Ling Chuang, Yi-Jehng Kuan, "Deep search for glycine conformers in Barnard 5".

Acknowledgments

Completing this thesis would not have been possible without the assistance, inspiration, and friendly words from many people. I therefore would like to first thank my PhD supervisors Prof. Eva Wirström and Dr. Per Bergman for hours of fruitful and interesting discussion (looking forward to more), as well as my friendly colleagues at SEE for a warm welcome in the cold North. Additional thanks goes to my former geochemistry docent Prof. Harry Becker for first awakening my interest in cosmochemistry and astrochemistry, to my former petrology docent Dr. Ralf Milke (who is no longer with us) and HiWi supervisor Dr. Vera Fernandes for being of great assistance in my transition from archaeology to geology and planetology, to Prof. Lena Noack for her exciting and insightful lectures on planetary physics, to Prof. Paola Caselli for giving me the opportunity to transition from planetology to astrochemistry, to Dr. Jaime Pineda and Dr. Anika Schmiedeke for supervision of my master thesis project at MPE, to Prof. John Black and Prof. Cathy Horellou for the discussion of key concepts related to the theory and observation of spectral line emission, and finally, to my close relatives and friends who always supported me in all possible ways to pursue my career in science and to stay the course in life.

Acronyms

ALI:	Accelerated Lambda Iteration
COM:	Complex Organic Molecule
ER:	Eley-Rideal
ESA:	European Space Agency
HGBS:	Herschel Gould Belt Survey
ISM:	Interstellar Medium
JWST:	James Webb Space Telescope
LTE:	Local Thermodynamic Equilibrium
LH:	Langmuir-Hinshelwood
MC:	Monte Carlo
NASA:	National Aeronautics and Space Administration
NIST:	National Institute of Standards and Technology
OSO:	Onsala Space Observatory
RD:	Reactive Desorption
RE:	Rate Equation
RT:	Radiative Transfer
SE:	Statistical Equilibrium

Contents

Part I

Overview

CHAPTER 1

Preliminary Thoughts and Motivation

Molecules in the interstellar medium can be studied for very different reasons: they can give insights into physical processes and conditions, but can also be intriguing study objects in their own right. Interstellar molecules can therefore be regarded as auxiliary tools in the field of astrophysics, but as the main objects of study in the field of astrochemistry, where the focus is on building an understanding for the formation and evolution of molecules in the Milky Way and other galaxies.

Section 1.1 of this chapter summarizes my motivation to obtain a doctoral degree in the field of astrochemistry, which is largely based on the unique way in which this field relates input from astronomy, astrophysics, chemistry, biology, geology, and planetology. Section 1.2 then provides a rather broad overview about the process of molecule formation in the interstellar medium, as studied by observation, experiment, and theory. Lastly, section 1.3 introduces some crucial physical concepts that are used throughout the following chapter 2.

1.1 From Molecular Clouds to Stars, Planets, and Life – An Astrochemical Perspective

Since the time of the ancient Greek philosophers, it has become increasingly more apparent that every bit of visible matter in the cosmos is constructed out of the very same building blocks. From the chemical perspective, these building blocks are the elements which can occur in different states (ionized or neutral, atomic or molecular) and in different phases (plasma, gas, liquid, solid), depending on the ambient physical conditions. On terrestrial planets like the Earth, most of the available matter is compressed into silicate-bearing minerals that surround a core of metal, mostly iron. At the surface, gravity can bind lighter, volatile elements to form an atmosphere of gases, which might be able to partly condense to form a hydrosphere, or to crystallize to form a cryosphere. If the conditions are right, molecules can even come together to form self-sufficient and replicating living organisms. What these conditions are and what particular molecules are required to induce this process is still not very well understood[1]. Some very basic facts, ideas, and principles related to those questions are discussed throughout this section.

On other planetary bodies, the conditions can be very similar but also extremely different from what we know from Earth. For example, deep inside the interior of Jupiter, the pressure becomes so high that hydrogen, Jupiter's main constituent, is forced into a liquid, forming the largest "ocean" of the solar system (NASA, 2023c). Under the icy crust of Jupiter's moon Europa (Fig. 1.1, left) lies another ocean which might contain twice the amount of water of Earth's oceans combined (NASA, 2023a). Saturn's moon Titan is the only solar system body other than Earth with an active hydrosphere. However, the liquid is not water but methane and ethane that fall as rain, carve rivers into the solid H_2O bedrock, and accumulate in lakes (NASA, 2023e). Interestingly enough, on Earth, living organisms are found in the most curious and hostile places one could imagine, including sea ice, hyperacidic lakes, volcanoes, and even inside of Chernobyl's collapsed nuclear reactor (Merino et al., 2019; Royal Society of Biology, 2023). This gives strong reason to believe that (primitive) life might have settled on other planetary bodies where

[1] Even less is understood about the process behind the actual transition from non-living to living matter (Pross, 2016).

conditions are similar to those observed in extreme environments on Earth. In the solar system, the most promising candidates to look for signs of ancient or present life are Mars and the icy-ocean worlds around Jupiter and Saturn (NASA, 2023d).

The vast number of 5 557 identified exoplanets and 10 028 exoplanet candidates around other stars (as of 23-12-16; NASA, 2023b) drastically increases the range of planetary conditions, as well as the number of potentially habitable bodies in the Milky Way. First and foremost, the habitability of a planetary body is confined by a combination of parameters that govern the availability of liquid water and the protection from harmful radiation. The general term "habitable zone" is defined as the zone around a star in which liquid water can be stable solely based on the radiative power of the star[2]. One major goal of exoplanetary research is to increase the number of Earth-like exoplanets located in that zone. According to a conservative estimate, 24 such exoplanets are identified (as of 23-12-16; University of Puerto Rico at Arecibo, 2023) and available for more detailed studies of e.g., exoplanetary atmospheres with state-of-the-art instruments like the James Webb Space Telescope (JWST). In combination with a planetary magnetic field, an atmosphere can provide crucial protection of the planetary surface from harmful radiation. It can furthermore increase the surface temperature of a body by means of the greenhouse effect, and thereby extend the range of circumstellar distance at which liquid water might be stable. Lastly, if life has settled on a planet, organisms can alter the composition of the atmosphere by adding characteristic chemicals, so-called bio-signatures, that can indicate the presence of life.

Further important parameters that define the habitability of a planetary body are the availability of a stable energy source to drive metabolic reactions, as well as the availability of biotic molecules. It is known from Earth that living organisms can use different forms of energy, mainly sunlight (photosynthesis) and chemical energy (chemosynthesis), to drive metabolic reactions. It is assumed that potential ocean life on Europa or Enceladus, just

[2] As is the case for some of the moons of Jupiter and Saturn, tidal heating between a giant planet and a small satellite can provide the energy to heat the interior of the satellite sufficiently to allow for the presence of liquid water in circumstellar zones well outside the habitable zone of a star (Breuer and Moore, 2015; Hussmann, 2015).

like some deep-sea life on Earth, would entirely depend on chemosynthesis. In this scenario, living organisms could develop in hydrothermal vent systems at the ocean floor, using minerals and chemicals coming through the vents and out of the body's interior (Fig. 1.1, right). In fact, the first living organisms on Earth could have formed by means of exactly this scenario (Weiss et al., 2016), but there are other possibilities like the early development in so-called warm little ponds (Pearce et al., 2017).

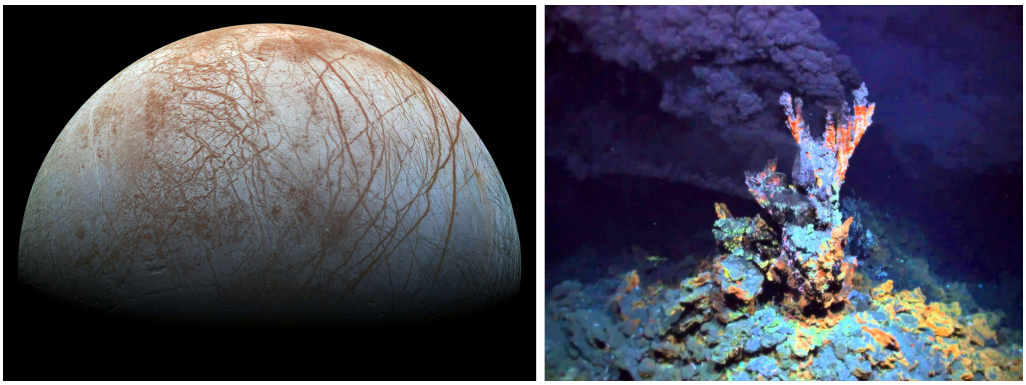

Figure 1.1: Left: Jupiter's moon Europa as captured by Galileo. Credit: NASA (2023a). **Right:** deep-sea hydrothermal vent. Credit: Science News (2019).

There is also no consensus about the origin of the biotic molecules required for the development of life. These molecules include different sugars, amino acids, nucleobases, and phosphor compounds. The main theories suggest that they might have been created inside of Earth's primordial atmosphere (Lazcano and Bada, 2003), or that they have been delivered by organic-rich bodies during Earth's accretion (Botta and Bada, 2002). Of course, also a combination of both mechanisms is feasible. Experiments have shown that a number of biotic amino acids and nucleobases could have formed from simple precursor species such as CO, H_2O, CH_4, and NH_3 inside of Earth's early atmosphere (Borquez et al., 2005; Cleaves et al., 2008; Ferus et al., 2017; Johnson et al., 2008, 2009; Miller, 1953). In addition, analyses of meteoritic samples have revealed a wealth of extraterrestrial amino acids, including many biotic ones, all five canonical nucleobases, and various types of sugars, including the RNA sugar ribose (Callahan et al., 2011; Cooper and Rios, 2016; Furukawa et al., 2019; Koga and Naraoka, 2017; Kvenvolden et al., 1970; Oba et al., 2022; Pearce and Pudritz, 2015). Observations of the comae of

comets 67P/Churyumov–Gerasimenko and 81P/Wild 2 have further revealed the presence of the simplest biotic amino acid glycine and different phosphor compounds (Altwegg et al., 2016; Elsila et al., 2009; Hadraoui et al., 2019). Different chemical pathways could lead to the in-situ formation of amino acids and nucleobases in sub-surface layers of meteoritic host bodies (Ioppolo et al., 2021; Lee et al., 2009; Pearce and Pudritz, 2015). However, there is evidence that e.g., the glycine in comet 67P might be inherited from a time before the formation of the Sun (Hadraoui et al., 2019).

Conceptually, what relates all minor and major planetary bodies of the solar system as well as the exoplanets around other stars of the Milky Way, is the fact that they are all made of the very same interstellar material as their host star. This basic principle was first formulated as a hypothesis, called the Kant-Laplace theory, more than 200 years ago (Lissauer and de Pater, 2013). Today, there is no doubt that planetary bodies form in so-called circumstellar disks of gas and dust around young stars on timescales of millions of years (Fig. 1.2, top). However, the details of this process are still not completely understood. In recent models, it is assumed that hydrothermal instabilities can cause over-dense filamentary structures in a disk, which can gravitationally collapse to form planetesimals very quickly. In volatile-rich outer disk regions, the planetesimals can then grow to gas and ice giants by pebble and gas accretion[3]. In the volatile-poor inner disk, terrestrial planets can form by planetesimal collisions and pebble accretion (Drążkowska et al., 2023; Johansen et al., 2021). It can be assumed that the flux of meteorites and comets onto terrestrial protoplanets is much higher than what is observed in the solar system today. Impacting meteorites and comets can thereby deliver organic materials and water to a growing protoplanet. In addition, the pebble accretion model assumes a constant flux of pebbles from outer to inner disk regions, which can further add significant amounts of water and organics. Thereby, observations of organics in meteorites and micrometeorites, simulations of cometary impacts, and recent pebble accretion models show that large amounts of water and organics can survive the entry into a protoplanetary atmosphere (Botta and Bada, 2002; Johansen et al., 2021).

[3]Pebbles are solid particles that are not defined based on size but based on aerodynamic properties, coupling them to the surrounding gas (Drążkowska et al., 2023). Therefore, the gas drag assumes a key role in the pebble accretion model of planet formation (Lambrechts and Johansen, 2012).

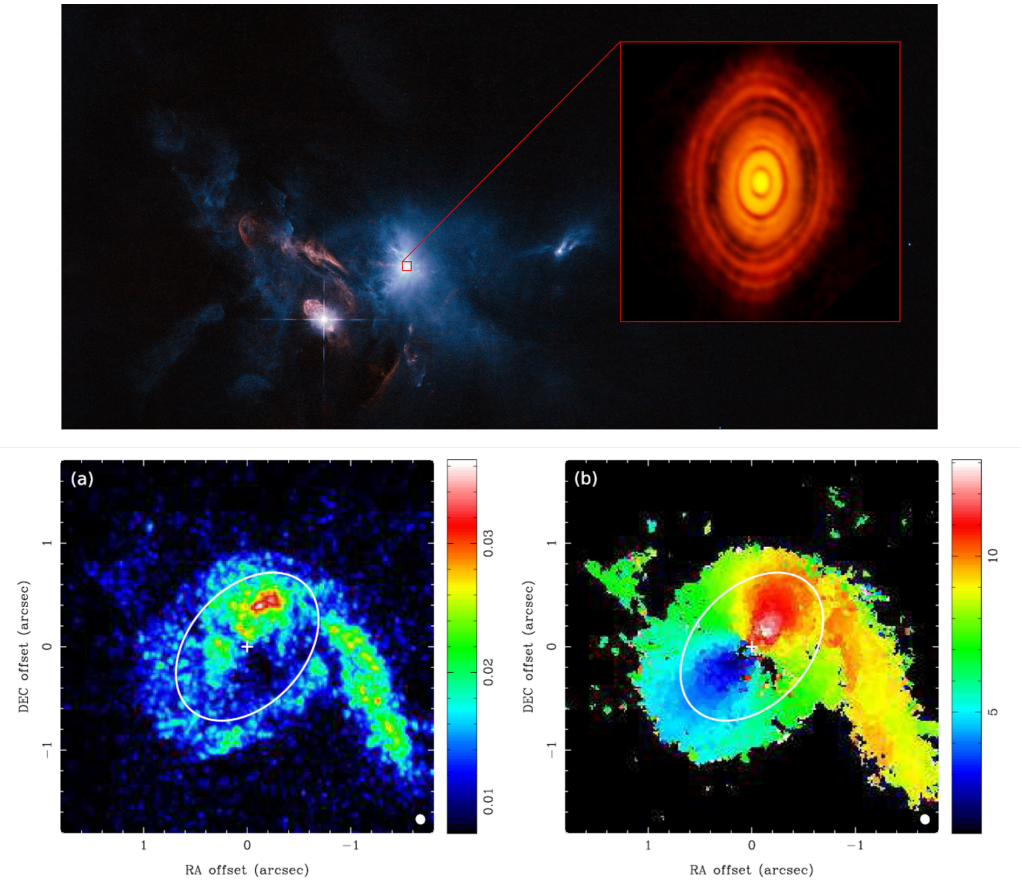

Figure 1.2: Top: the background image shows the surroundings of the young protostar HL Tauri as seen by HST (Hubble Space Telescope). The image in the box shows the circumstellar disk around HL Tauri as seen by ALMA (Atacama Large Millimeter/submillimeter Array). Credit: ESA (2023). **Bottom:** streamer is feeding the HL Tauri circumstellar system. Images are created from ALMA $HCO^+(3-2)$ data. Image (a) shows the peak intensities, and image (b) shows the velocities of the intensity peaks. The white cross marks the location of the HL Tauri protostar, and the white ellipse indicates the extension of the surrounding disk. Credit: Yen et al. (2019).

In the Milky Way, new stars are continuously formed within the coldest ($10-50\,\mathrm{K}$) and densest ($\sim 10^4\,\mathrm{cm}^{-3}$) large-scale structures of the interstellar medium, i.e., molecular clouds (see also Tab. 1.1). Observations have shown that molecular clouds are pervaded by networks of over-dense filaments that can gravitationally collapse to spheroidal dense cores, if a certain (critical)

mass per unit length is exceeded (André et al., 2010) (Fig. 1.3). If the density is high enough, such cores will further collapse to form a protostar at their center. Observations show that young protostars (class 0/I), which are embedded in an envelope of gas and surrounded by a circumstellar disk, gets fed by so-called streamers with material from the surrounding filament (Hsieh et al., 2023; Pineda et al., 2020; Valdivia-Mena et al., 2022, 2023; Yen et al., 2019) (Fig. 1.2, bottom). It can be assumed, that the process of planet formation has already started at this stage (Drążkowska et al., 2023). This means that circumstellar systems around young protostars are far from being isolated units (Max-Planck-Gesellschaft, 2023), but that there is a direct transfer of chemical compounds from the interstellar medium to planet forming regions.

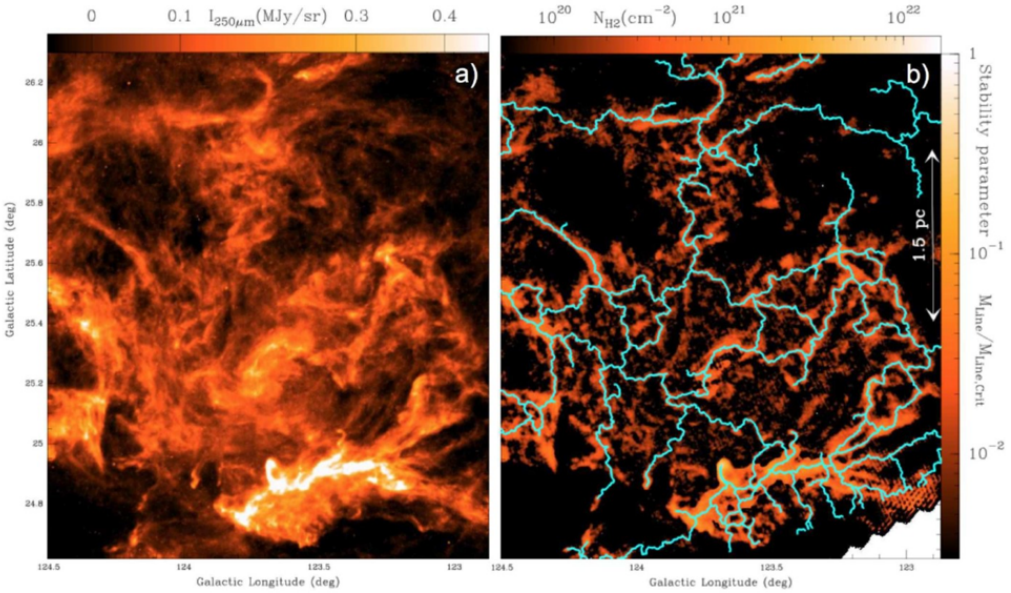

Figure 1.3: .**(a):** HSO (Herschel Space Observatory) 250 µm dust continuum map of a part of the Polaris Flare. **(b):** corresponding H_2 column density map. The light blue lines indicate a network of over-dense filaments. The critical mass per unit length is expressed in terms of the stability parameter $M_{\mathrm{Line}}/M_{\mathrm{Line,Crit}}$. Credit: André et al. (2014).

In the outer mid-plane-regions of a circumstellar disk, where temperatures are low, it can be assumed that interstellar material gets incorporated into pebbles and minor planetary bodies without being strongly altered. Astro-

nomical observations have shown that so-called complex organic molecules (COMs), defined as carbon-bearing molecules composed of at least six atoms[4], can be present in dense molecular cloud cores even before the formation of a protostar (see following section). Major goals of recent astrochemical research are to understand (i) the formation pathways of such COMs at very low temperatures prevalent in "star-less" environments (see following section), as well as (ii) their degree of alteration through subsequent phases of star and planet formation. In addition, since the first detection of amino acids in meteorites it has been speculated that biotic organic molecules might partly originate from interstellar space (Ehrenfreund and Charnley, 2000; Hoyle and Wickramasinghe, 1977), which would have important astrobiological consequences. Since several decades, astronomers are therefore searching the interstellar medium for signs of such molecules. In this regard, interesting recent detections include hydroxylamine (NH_2OH) and urea (NH_2CONH_2), which have been observed in the giant molecular cloud G+0693-0.027 near the galactic center (Jiménez-Serra et al., 2020; Rivilla et al., 2020b). Both species can be considered precursors of RNA ribonucleotides. In addition, the important cell membrane molecule ethanolamine ($NH_2CH_2CH_2OH$) has been tentatively detected in the same source as well (Zeng et al., 2021). Some other studies have revealed the presence of comparatively high amounts of phosphorous monoxide (PO) in the star-forming regions W51, W3, and AFGL 5142 (Rivilla et al., 2016, 2020a). Paper A of this thesis presents a deep-search for the simplest amino acid glycine (NH_2CH_2COOH) in the cold low-mass source Barnard 5 in Perseus. In a second paper, which is currently in preparation, we further investigate possible COM formation mechanisms by studying the distribution of COMs in the same source (see following section and chapter 4).

1.2 Molecule Formation in the Interstellar Medium

The term "interstellar medium" (ISM) includes all baryonic matter in a galaxy that is not bound in active stars, brown dwarfs, or stellar remnants, i.e., roughly 10 % of the matter in the Milky Way. Measurements have shown that the ISM of the Milky Way is composed of 70 % hydrogen, 28 % helium, and 2 % heavier elements. Around half of the heavier elements is bound in dust

[4]This definition is quite loose because sometimes, also species like formaldehyde (H_2CO) or ketene (CH_2CO) are listed as COMs in the literature.

grains, leading to an average dust-to-gas mass ratio of about 0.01 (Bennett et al., 2010; Palme et al., 2014; Yamamoto, 2017).

Depending on the ambient temperature and density, the ISM gas assumes different states in different regions (see Tab. 1.1). In shock-heated and strongly photoionized regions (hot ionized medium and H-II regions), temperatures are extremely high and densities extremely low, such that atoms occur in their ionized form. Going to regions with lower temperatures and higher densities (H-I regions), atoms start to become neutral (Draine, 2011). Only at temperatures $< 100\,\mathrm{K}$ and densities $> 100\,\mathrm{cm}^{-3}$ (diffuse clouds), atoms start to form first simple molecules such as H_2, CO, CN, CH, OH, or NH. In the coolest and densest regions of the ISM (molecular clouds), newly formed molecules are efficiently shielded from harmful radiation by the presence of interstellar dust or by means of "self-shielding", leading to the first long-term accumulations of molecules and the progressive evolution to remarkably complex molecular species. In regions of ongoing star formation (protostellar cores and circumstellar disks), high temperatures and strong stellar radiation fields give rise to even more chemical pathways and a very rich molecular inventory (Caselli and Ceccarelli, 2012; Draine, 2011; Yamamoto, 2017).

Table 1.1: ISM regions with their typical temperatures T, densities $n(\mathrm{H})$, and states of matter (SOMs). Values from: Draine (2011); van Dishoeck et al. (2013).

	T [K]	$n(\mathrm{H})$ [cm^{-3}]	SOMs
hot ionized medium	$> 10^5$	~ 0.004	at.; ion.
H-II regions	$\sim 10^4$	~ 0.3	at.; ion.
H-I regions	$100-5000$	$0.6-30$	at.; ion., neut.
diffuse clouds	$30-100$	$\sim 10^2$	at., mol.; ion., neut.
molecular clouds	$10-50$	$\sim 10^4$	at., mol.; ion., neut.
starless cores	$7-15$	$> 10^5$	
protostellar cores	$7-200$	10^5-10^9	
circumstellar disks	$7-3000$	10^6-10^{15}	

at.: atomic; mol.: molecular; ion.: ionized; neut.: neutral

As of February 2024, 307 molecules have been clearly identified in interstellar and circumstellar regions (Universität zu Köln, 2024). Most of these are di- and triatomic molecules, but there are also many with seven to ten atoms, and several with more than twelve atoms. The gas phase formation of even the most basic (as most abundant) interstellar molecule, i.e., molecular hydrogen (H_2), can be very challenging at the low densities prevalent in diffuse and molecular clouds[5]. This comes down to the fact that the reaction energy released during the formation of a di-atomic molecule can disrupt the molecule right away if it is not carried away by a third body. However, the probability that three gas phase atoms meet at the same spot at low densities is vanishingly small, such that three-body gas phase reactions do virtually not occur in the ISM (Yamamoto, 2017). For that reason, interstellar dust grains (carbon and silicates) play a crucial role for the formation of interstellar molecules, as they provide the surface on which chemical reactions can take place. They can be regarded as both catalysators for chemical reactions as well as the third body for three body reactions (Cuppen et al., 2017; Yamamoto, 2017). Fig. 1.4 (left) summarizes the fundamental principles related to gas-grain interactions: gas phase atoms and molecules, simply called "particles" in the following, can attach to a dust grain, move across its surface, and react when close enough to a reaction partner. Particles move across a grain surface mainly by means of thermal diffusion, but also quantum tunneling can be important (Cuppen et al., 2017; Nyman, 2021; Taquet, 2013; Vasyunin et al., 2017). Reactions proceed mainly by the so-called Langmuir-Hinshelwood mechanism, in which particles have to move to encounter a reaction partner. Alternatively, particles can react immediately upon accretion via the so-called Eley-Rideal mechanism, i.e., when a gas phase particle directly accretes at the site of a reaction partner (Cuppen et al., 2017; Taquet, 2013; Yamamoto, 2017). A set of further non-diffusive reaction mechanisms was introduced in Jin and Garrod (2020), as discussed in chapter 4. Particles can also desorb back into the gas phase before, after, or upon reaction by means of (i) thermal desorption, (ii) photo-desorption, (iii) cosmic ray desorption, and (iv) chemical desorption (Cuppen et al., 2017; Taquet, 2013; Yamamoto, 2017).

[5] Even though molecular clouds are high-density ISM regions, densities of around $10^4\,\mathrm{cm}^{-3}$ correspond to high vacuum conditions in terrestrial terms.

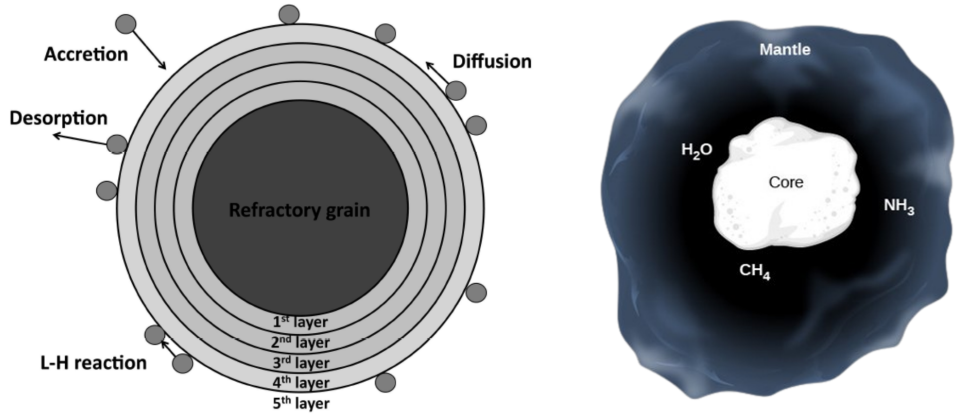

Figure 1.4: Left: gas-grain interactions (accretion, diffusion, reaction, and desorption) lead to the build up of solid ices at the surface of refractory, interstellar dust grains. Credit: Taquet et al. (2012). **Right:** early ice species include H_2O, CH_4, and NH_3, that form by subsequent hydrogenation of O, C, and N. Credit: College Sidekick (2024).

Observations, experiments, and models over the past decades have demonstrated that, by the process of gas-grain interactions, interstellar dust grains in cold molecular clouds get covered by comparatively thick ice mantles (see Fig. 1.4, right). The average radius of the bare grains is approximately 0.1 µm, and the ice mantles can reach a thickness of a quarter to a third of that[6] (Caselli and Ceccarelli, 2012; Taquet et al., 2012). Infrared observations towards stellar background sources show that interstellar ice mantles are mainly composed of water (H_2O), carbon monoxide (CO), carbon dioxide (CO_2), methane (CH_4), ammonia (NH_3), and methanol (CH_3OH). Through all phases of ice evolution, the overall ice composition is always dominated by H_2O (Boogert et al., 2008, 2015; Yamamoto, 2017). It is assumed that the formation of H_2O, CO_2, CH_4, and NH_3 starts at $T < 90\,\mathrm{K}$ and $n(\mathrm{H}) \geq 10^3\,\mathrm{cm}^{-3}$ (Boogert et al., 2015; Chuang et al., 2022), i.e., at the transition from diffuse clouds to molecular clouds. The formation of H_2O, CH_4, and NH_3 likely proceeds by the subsequent hydrogenation of O, C, and N, respectively (Boogert et al., 2015; Chuang et al., 2018, 2022; Yamamoto, 2017), while CO_2 is assumed to be formed mainly via $\mathrm{CO} + \mathrm{OH}$ (Boogert et al., 2015). CO is mostly formed in the gas phase, and widely distributed in diffuse clouds and molecu-

[6] Fig. 1.4 (right) clearly overestimates the mantle thickness.

lar clouds. The accretion rate of CO onto grains is generally increasing with decreasing temperature and increasing density, such that a layer of CO forms on top of the earlier ice layer inside of molecular clouds at $\sim 10^4\,\mathrm{cm}^{-3}$. At even higher densities $> 10^5\,\mathrm{cm}^{-3}$, prevalent in cold dense cloud cores, a "catastrophic" CO freeze-out is observed. This ultimately leads to a third ice layer that is dominated by CH_3OH, which forms by subsequent hydrogenation of CO[7] (Boogert et al., 2008, 2015; Caselli and Ceccarelli, 2012; Tielens et al., 1991; Yamamoto, 2017). The above picture of interstellar ice formation is very general, and it should be kept in mind that local variations in gas composition can alter the final ice composition (Boogert et al., 2015). The JWST has the potential to deepen our understanding of the composition of interstellar ices, tremendously, thanks to its excellent capabilities to observe in the infrared (McClure et al., 2023).

After the fist detections of gas phase COMs in high-mass star forming regions and around young protostars, it was first assumed that they are mainly the product of thermal/radiative processing of interstellar ices (Caselli and Ceccarelli, 2012; Yamamoto, 2017). However, the detection of gas phase COMs in cold molecular cloud environments (Bacmann et al., 2012; Friberg et al., 1988; Jiménez-Serra et al., 2016; Marcelino et al., 2007; Matthews et al., 1985; Taquet et al., 2017; Vastel et al., 2014), where temperatures can be $< 10\,\mathrm{K}$, has shown that this picture cannot account for all observations. The presence of COMs such as acetaldehyde (CH_3CHO), di-methyl ether (CH_3OCH_3), and methyl formate (CH_3OCHO) at such low temperatures and in the absence of surrounding stellar sources indicates that (i) the formation of COMs starts even before the onset of star formation, and (ii) that efficient non-thermal formation and desorption pathways must exist for those COMs. In this regard, recent models favor scenarios in which chemical desorption is key[8]. The details of these scenarios can be however quite different, and one can roughly separate between two major scenarios. The first assumes the formation of COMs at the surface of ice-covered grains, followed by the

[7] Especially at low temperatures, H atoms are the only mobile species on dust grain surfaces, which is the reason why hydrogenation reactions are so important. However, other species can become mobile at higher temperatures, thereby decreasing the importance of hydrogenation reactions (Yamamoto, 2017).

[8] Chemical desorption (or reactive desorption) describes the process in which the chemical energy of an exothermic reaction is used to overcome the bonds of a reaction product to the ice surface. This process is discussed in some more detail in section 4.1.

immediate release into the gas phase by chemical desorption (Jin and Garrod, 2020). The second assumes the formation of precursor molecules and radicals at grain surfaces, followed by chemical desorption and COM formation in the gas phase (Vasyunin et al., 2017). Of course, also a combination of both scenarios could be feasible (Chuang et al., 2018). We aim to set constraints on these scenarios with observations of gas phase COMs and radicals around the methanol hotspot in Barnard 5 (see chapter 4).

In view of the possible existence of biotic COMs in the interstellar medium, it is interesting to note that possible formation pathways for many biotic species have been revealed in laboratory and theoretical studies. For example, experiments indicate that the sugars of both RNA and DNA, i.e., ribose and 2-dioxyribose, can be formed during UV irradiation of interstellar ice analogues, which translates to the warm-up stage of star formation (Nuevo et al., 2018). Furthermore, a combined experimental and theoretical study has shown that the simplest biotic amino acid glycine can be formed on interstellar ices even in the absence of any energetic irradiation (Ioppolo et al., 2021). The latter study is a key reference in our publication on the search for glycine in the cold molecular cloud source Barnard 5 (see paper A).

1.3 Basic Concepts

This section introduces the basic equations of some fundamental physical concepts used throughout the following chapter 2, i.e., the Boltzmann distribution (section 1.3.1), Planck's law of thermal radiation (section 1.3.2), and the absorption and emission of radiation by atoms and molecules (section 1.3.3).

1.3.1 The Boltzmann Distribution

One of the most fundamental concepts in physical chemistry is the Boltzmann distribution. It is a measure of how the energy of a collection of particles (e.g., atoms, ions, or molecules) is distributed in thermal equilibrium at a certain temperature. The term "thermal equilibrium" describes a steady state in the energy distribution, meaning that there is no net change of energy between the particles (see also section 2.3.2).

Assuming a total number of particles n_{tot} of the same kind, the Boltzmann distribution calculates the number of particles n_i with energy E_i as a fraction of n_{tot} and as a function of temperature T, i.e.,

$$\frac{n_i}{n_{\text{tot}}} = \frac{1}{q} \exp\left(-\frac{E_i}{k_{\text{B}}T}\right), \tag{1.1}$$

where q is a partition function (acting as a normalization constant), defined as

$$q = \sum_i \exp\left(-\frac{E_i}{k_{\text{B}}T}\right), \tag{1.2}$$

and k_{B} is the Boltzmann constant (Atkins et al., 2018). It can be seen that, as the temperature increases, higher energy states are populated at the expense of states with lower energy (see Fig. 1.5).

The Boltzmann distribution can also be used to calculate the number of particles in one state with energy E_i relative to the number of particles in another state with energy $E_j > E_i$ (Atkins et al., 2018), i.e.,

$$\frac{n_i}{n_j} = \exp\left(-\frac{(E_j - E_i)}{k_{\text{B}}T}\right) = \exp\left(-\frac{\Delta E}{k_{\text{B}}T}\right). \tag{1.3}$$

Here, it becomes apparent that the relative population of any two states decreases as the energy separation between the considered states increases.

It is furthermore important to note the distinction between energy states and energy levels (Atkins et al., 2018). Eq. (1.3) calculates populations of energy states, but several states might have the same energy, and any one of these states has the same population. This effect can be considered when instead calculating the relative population of energy levels, by taking into account the degeneracies (statistical weights) g_i and g_j of the levels with energies E_i and E_j. Eq. (1.1) then becomes

$$\frac{n_i}{n_{\text{tot}}} = \frac{g_i}{Q} \exp\left(-\frac{E_i}{k_{\text{B}}T}\right) \tag{1.4}$$

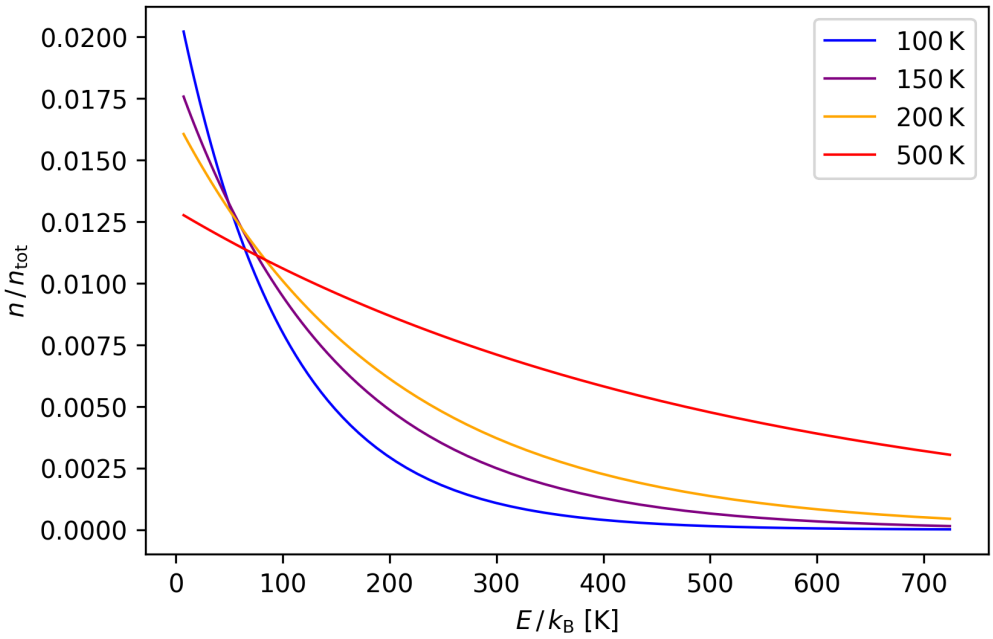

Figure 1.5: Arbitrary Boltzmann distribution for a collection of particles at different temperatures, according to Eq. (1.1) and assuming a continuous range of energies. With increasing temperature, the number of particles in higher energy states increases at cost of the number of particles in lower energy states.

with partition function

$$Q = \sum_i g_i \exp\left(-\frac{E_i}{k_{\mathrm{B}}T}\right), \tag{1.5}$$

while Eq. (1.3) becomes

$$\frac{n_i}{n_j} = \frac{g_i}{g_j} \exp\left(-\frac{\Delta E}{k_{\mathrm{B}}T}\right). \tag{1.6}$$

1.3.2 Planck's Law of Thermal Radiation

Another important concept that is frequently used for the interpretation and modelling of astronomical data is Planck's law of thermal radiation, describing the properties of blackbody radiation. Conceptually, a blackbody is an object in thermal equilibrium with its surroundings, absorbing all electromagnetic

radiation it receives. In order to stay in equilibrium, a blackbody has to emit radiation at the same rate as it absorbs it (Atkins et al., 2018; University of California San Diego, 2023). Although perfect blackbodies do not exist in nature, the radiation emitted by many natural objects like stars, planets, light bulbs, and also humans can be approximated to a high degree as blackbody radiation in a certain frequency range (Bennett et al., 2010).

Assuming a spherical blackbody at a certain distance from an observer, Planck's law of thermal radiation can be used to calculate the spectral intensity $B_\nu(T)$ of the body. The spectral intensity gives the emitted energy E per unit time t, per unit frequency ν[9], per unit solid angle Ω, received per unit area A, i.e.,

$$B_\nu(T) = \frac{\mathrm{d}E}{\mathrm{d}t\,\mathrm{d}\nu\,\mathrm{d}\Omega\,\mathrm{d}A}\,, \tag{1.7}$$

such that it has dimensions of $\mathrm{J\,s^{-1}\,Hz^{-1}\,sr^{-1}\,m^{-2}}$. The emitted energy, which is proportional to the number of photons emitted per unit solid angle, is the same in each direction of space. However, the received energy, proportional to the number of photons collected per unit area, depends on the distance to the observer. The emitted energy furthermore depends on the considered frequency range. According to Planck's law, the spectral intensity is calculated as

$$B_\nu(T) = \frac{2h\nu^3}{c^2}\left[\exp\left(\frac{h\nu}{k_\mathrm{B}T}\right) - 1\right]^{-1}\,, \tag{1.8}$$

where h is the Planck constant, ν is the frequency, c is the speed of light, k_B is the Boltzmann constant, and T is the temperature. The explicit units of $B_\nu(T)$ are $\mathrm{J\,m^{-2}}$, which means that the remaining units, i.e., $\mathrm{s^{-1}\,Hz^{-1}\,sr^{-1}}$, are implicit[10]. Integrating the spectral intensity over frequency gives the total intensity $B(T)$ of the body, i.e.,

$$B(T) = \int_0^\infty B_\nu(T)\mathrm{d}\nu\,. \tag{1.9}$$

Fig. 1.6 shows the spectral intensity of blackbody radiation for a range of frequencies and different temperatures. It can be seen that, as the temperature

[9] Equivalent expressions can be given in terms of wavelength or wavenumber.
[10] Even though the units of time and frequency cancel each other, they should be kept to keep track of the complete physical setting.

increases, the peak spectral intensity is shifting towards higher frequencies (Wien's displacement law) while the total intensity, described by Eq. (1.9), increases.

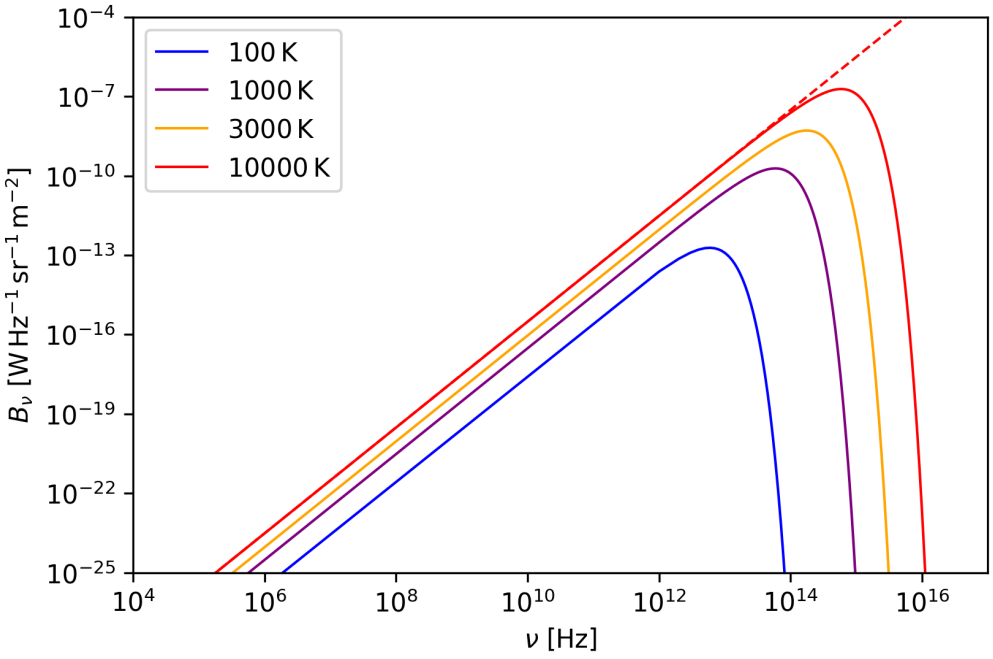

Figure 1.6: Spectral intensity $B_\nu(T)$ of blackbody radiation for a range of frequencies and different temperatures, calculated from Eq. (1.8). With increasing temperature, the peak spectral intensity shifts towards higher frequencies while the total intensity ($\int B_\nu(T)\mathrm{d}\nu$) increases. The red dashed line indicates the Rayleigh-Jeans approximation (Eq. 1.10) for 10 000 K.

An important approximation to Planck's law often used in radio astronomy is the so-called Rayleigh-Jeans approximation. It is a good approximation to the spectral intensity of a blackbody in the limit $h\nu \ll k_\mathrm{B}T$, i.e., in the linear part of the graphs in Fig. 1.6, and is simply written as

$$B_\nu(T) = \frac{2k_\mathrm{B}T\nu^2}{c^2} \tag{1.10}$$

(Condon and Ransom, 2016). In fact, before Planck's invention of energy quantization, the Rayleigh-Jeans approximation was the best theoretical description of experimentally derived blackbody spectra. However, it is only a

good description at low frequencies, while the modelled intensities are going to infinity at higher frequencies (see red dashed line in Fig. 1.6). This behavior became known as the "ultra-violet catastrophe" (Atkins et al., 2018). Essentially, Planck's law can also be written as a combination of the Rayleigh-Jeans approximation and a quantum correction factor α, i.e.,

$$B_\nu(T) = \frac{2k_\mathrm{B}T\nu^2}{c^2}\alpha\,, \tag{1.11}$$

with

$$\alpha = \frac{h\nu}{k_\mathrm{B}T}\left[\exp\left(\frac{h\nu}{k_\mathrm{B}T}\right) - 1\right]^{-1}. \tag{1.12}$$

One can conclude that the intensity of a blackbody is well described by the Rayleigh-Jeans approximation only if $\alpha \to 1$ (Condon and Ransom, 2016).

1.3.3 Absorption and Emission of Radiation

Observations of molecules in interstellar space are based on the analysis of molecular emission and absorption spectra. Such spectra are the result of photons being emitted or absorbed during transitions between different molecular energy levels. The corresponding absorption and emission processes can be broken down to the following three:

(1) stimulated absorption,

(2) stimulated emission,

(3) spontaneous emission.

Stimulated absorption describes the process in which a transition from a lower energy level l to an upper energy level u is driven by the absorption of a photon whose energy equals the energy difference between both levels ($\Delta E = h\nu$). Thereby, the rate of absorption is proportional to the spectral intensity I_ν of the incident radiation at the absorption frequency $\nu = \Delta E/h$. That is, the greater the radiation intensity the greater the number of photons impinging on the molecule and the greater the probability that a photon will be absorbed. The rate is also proportional to the number of molecules in the lower level n_l, because the greater the population of that level, the more

likely it is that a photon will encounter a molecule in that level. The rate of stimulated absorption can therefore be written as

$$W_{\mathrm{lu}} = B_{\mathrm{lu}} n_{\mathrm{l}} I_{\nu} \,, \tag{1.13}$$

where B_{lu} is the so-called Einstein coefficient of stimulated absorption (Atkins et al., 2018).

Stimulated emission is the process in which a photon is emitted during a transition from an upper energy level to a lower energy level. The rate of stimulated emission is proportional to the intensity of incident radiation at the transition frequency as well as to the number of molecules in the upper energy level n_{u}, i.e.,

$$W'_{\mathrm{ul}} = B_{\mathrm{ul}} n_{\mathrm{u}} I_{\nu} \,, \tag{1.14}$$

where B_{ul} is the Einstein coefficient of stimulated emission. Finally, in spontaneous emission, a molecule can spontaneously emit a photon by making the transition from an upper energy level to a lower energy level even in the absence of radiation. The rate of spontaneous emission is therefore only proportional to the number of molecules in the upper state and can be written as

$$W''_{\mathrm{ul}} = A_{\mathrm{ul}} n_{\mathrm{u}} \,, \tag{1.15}$$

where A_{ul} is the Einstein coefficient of spontaneous emission. When both spontaneous and stimulated emission are taken into account, the total rate of emission is

$$W_{\mathrm{ul}} = A_{\mathrm{ul}} n_{\mathrm{u}} + B_{\mathrm{ul}} n_{\mathrm{u}} I_{\nu} \tag{1.16}$$

(Atkins et al., 2018).

Assuming thermal equilibrium, the rates of emission and absorption are equal (Kirchhoff's law of thermal radiation; Yamamoto, 2017), which means that the rate of change from one energy level to another is zero. Furthermore, the spectral intensity of radiation can be expressed in terms of blackbody radiation at temperature T. Considering the above expressions for the transition rates, this can be written exemplary for the lower energy level as

$$\frac{\mathrm{d}n_{\mathrm{l}}}{\mathrm{d}t} = A_{\mathrm{ul}} n_{\mathrm{u}} + B_{\mathrm{ul}} n_{\mathrm{u}} B_{\nu}(T) - B_{\mathrm{lu}} n_{\mathrm{l}} B_{\nu}(T) = 0 \,, \tag{1.17}$$

which can be re-arranged to give an expression for the blackbody radiation, i.e.,

$$B_\nu(T) = \frac{A_{\mathrm{ul}}}{\frac{n_{\mathrm{l}}}{n_{\mathrm{u}}} B_{\mathrm{lu}} - B_{\mathrm{ul}}} \,. \tag{1.18}$$

Here, the relative population of energy levels $n_{\mathrm{l}}/n_{\mathrm{u}}$ can be expressed in terms of a Boltzmann distribution (Eq. 1.6), such that the above equation can be expressed as

$$B_\nu(T) = \frac{A_{\mathrm{ul}}}{B_{\mathrm{ul}}} \left[\frac{g_{\mathrm{l}}}{g_{\mathrm{u}}} \frac{B_{\mathrm{lu}}}{B_{\mathrm{ul}}} \right]^{-1} \left[\exp\left(\frac{h\nu}{k_{\mathrm{B}} T} \right) - 1 \right]^{-1} . \tag{1.19}$$

Comparing this to Planck's law for the spectral intensity of a blackbody (Eq. 1.8), one can conclude that, at thermal equilibrium,

$$g_{\mathrm{u}} B_{\mathrm{ul}} = g_{\mathrm{l}} B_{\mathrm{lu}} \tag{1.20}$$

and

$$A_{\mathrm{ul}} = \frac{2h\nu^3}{c^2} B_{\mathrm{ul}} \,. \tag{1.21}$$

If follows that, if the value of only one Einstein coefficient is known, the values of the other two coefficients can be directly derived from it.

CHAPTER 2

Derivation of Molecular Abundances from Observations

This chapter introduces the physical background and the basic methods employed for the derivation of molecular abundances from astronomical observations. According to the focus of the attached scientific work, the focus of this chapter will be on molecules in cold molecular cloud sources.

Section 2.1 gives a broad overview about the field of rotational spectroscopy, which forms the very basis of observational studies focusing on gas phase molecules in cold molecular clouds. Section 2.2 then discusses the physical parameters that govern the shape and width of molecular spectral lines. In section 2.3, it is discussed how the population of molecular (rotational) energy levels depends on the ambient physical conditions. Section 2.4 introduces some of the most basic concepts related to the measurement, modelling, and interpretation of spectral line emission from molecular clouds. Lastly, section 2.5 covers the basic equations and methods to derive molecular column densities from measured spectral line intensities.

2.1 Rotational Spectroscopy

At very low temperatures, characteristic for cold ($< 10-50\,\mathrm{K}$) molecular cloud sources, molecules are mostly in their electronic and vibrational ground states, and only their rotational energy levels are populated. Therefore, the radiation from cold molecular clouds is mainly produced by transitions between distinct molecular rotational energy levels[1]. Photons associated with such transitions have frequencies in the radio range of the electromagnetic spectrum, and can be observed with single-dish radio telescopes or interferometers. In the following, I will first briefly introduce the classification scheme of molecules in the framework of rotational spectroscopy (section 2.1.1). Then, the basic equations for the calculation of rotational energy levels and spectra are discussed along with some crucial related concepts (section 2.1.2).

2.1.1 Molecular Classification

In the framework of rotational spectroscopy, molecules can be separated into five major classes, based on their moment of inertia (MoI). The MoI of any 3D body is described by a symmetric, second-rank tensor $\boldsymbol{I}$. If it is assumed for an arbitrary molecule that the underlying coordinate system (with origin at the center of mass) rotates when the molecule rotates (molecule-fixed axes), the MoI tensor becomes diagonal, and is written as

$$\boldsymbol{I} = \begin{pmatrix} I_a & 0 & 0 \\ 0 & I_b & 0 \\ 0 & 0 & I_c \end{pmatrix} , \tag{2.1}$$

where I_a, I_b, and I_c are the principal MoI components (Gordy and Cook, 1984; Hollas, 1998, 2004; Yamamoto, 2017). Using the principal axes theorem, the MoI tensor can be further transferred into its quadric form, which describes the surface of an ellipsoid, i.e.,

$$f(\mathbf{x}) = \left(\frac{x_1}{\sqrt{1/I_a}} \right)^2 + \left(\frac{x_2}{\sqrt{1/I_b}} \right)^2 + \left(\frac{x_3}{\sqrt{1/I_c}} \right)^2 . \tag{2.2}$$

[1] It is also possible to observe rotational transitions of molecules in their first excited vibrational states at relatively low temperatures, but I will neglect this possibility and focus on pure rotational spectra.

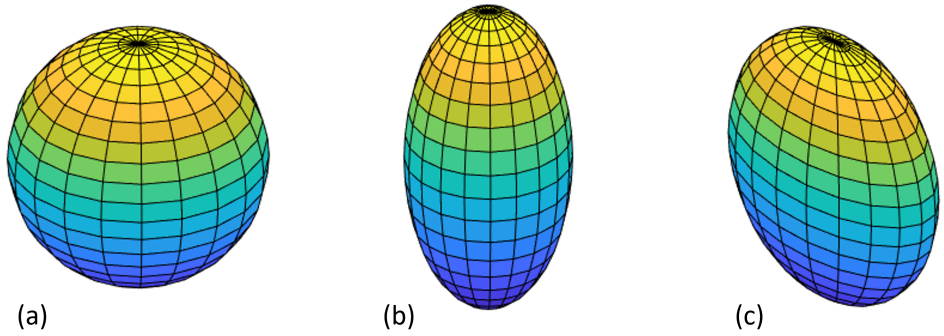

Figure 2.1: Ellipsoidal quadric surfaces resulting from different, relative MoI components (I_a, I_b, and I_c) in Eq. (2.2): (a) sphere ($I_c = I_b = I_a$), (b) prolate spheroid ($I_c = I_b > I_a$), (c) oblate spheroid ($I_c > I_b = I_a$). A triaxial ellipsoid ($I_c \neq I_b \neq I_a$) is a mixture of figures (b) and (c).

In rotational spectroscopy, it is convention to chose that

$$I_c \geq I_b \geq I_a \tag{2.3}$$

(Atkins et al., 2018; Hollas, 2004). In that case, and depending on the actual values of the principal MoI components, the quadric surface representing the MoI tensor will assume different shapes (Hollas, 1998, see Fig. 2.1):

(1) if $I_c = I_b = I_a$, the quadric surface is a sphere,

(2) if $I_c = I_b > I_a$, the quadric surface is a prolate spheroid,

(3) if $I_c > I_b = I_a$, the quadric surface is an oblate spheroid, and

(4) if $I_c \neq I_b \neq I_a$, the quadric surface is a triaxial ellipsoid.

The classification of molecules in rotational spectroscopy follows directly from the four cases above (Hollas, 1998, 2004; Yamamoto, 2017):

(1) molecules with $I_c = I_b = I_a$ are called spherical rotors,

(2) molecules with $I_c = I_b > I_a$ are called prolate symmetric rotors,

(3) molecules with $I_c = I_b > I_a = 0$, i.e., special cases of (2), are called linear rotors,

(4) molecules with $I_c > I_b = I_a$ are called oblate symmetric rotors, and

(5) molecules with $I_c \neq I_b \neq I_a$ are called asymmetric rotors.

In fact, those five classes can be reduced to three when summing up classes (2), (3), and (4) under the term symmetric rotors (Atkins et al., 2018). As can be seen, the symmetry of molecules decreases from class (1) to class (5). Based on that, the equations for the calculation of rotational energies become increasingly more complex with increasing molecular asymmetry.

2.1.2 Rotational Energy Levels, Spectra, and Selection Rules

The rotational energy of a molecule is a quantized property, and the rotational energy eigenvalues can be obtained by solving the time-independent Schrödinger equation with the rotational Hamiltonian operator. This way, analytical expressions for the calculation of rotational energies can be found for all molecular classes, except asymmetric rotors. For that class, it is necessary to use the concepts of matrix mechanics to derive approximate solutions[2] (Atkins et al., 2018; Gordy and Cook, 1984; Hollas, 2004; Yamamoto, 2017). In this section, I will not cover the explicit equations for the calculation of rotational energies for the different molecular classes, but rather give a broad overview about some important concepts and approaches.

As a first order approximation, molecules in rotational spectroscopy can be considered as point-masses connected by stiff (rigid) interatomic axes with fixed lengths. This picture of a molecule is summarized under the term rigid rotor approximation. However, the interatomic axes of a molecule are actually not rigid, but undergo lengthening due to centrifugal forces upon rotation. Considering this effect in the calculation of rotational energies requires the use of molecule-dependent rotational distortion constants (Atkins et al., 2018; Gordy and Cook, 1984; Yamamoto, 2017). Distortion constants are a measure of stiffness along the bonds in a molecule (Atkins et al., 2018) and tabulated values (derived from experiments or theory) can be found for many molecules in the literature or in databases.

[2] In matrix mechanics, quantum mechanical operators are treated as matrices, and the problem of solving the Schrödinger equation is shifted to a matrix diagonalization problem (Gordy and Cook, 1984).

The rotational energies of all molecular classes are described by at least two good quantum numbers $J = 0, 1, 2, \ldots$ and $M_J = \pm 1, \pm 2, \ldots, \pm J$, which are the respective spectroscopic equivalents of the total angular momentum quantum number and the magnetic quantum number, defined for the general case of a rotating quantum object. In the absence of a surrounding electromagnetic field, the rotational energies of a molecules do not directly depend on the value of M_J. However, each level is $(2J + 1)$-fold degenerate because there are $2J + 1$ values of M_J for each value of J. The independence of the rotational energy on quantum number M_J can be interpreted in the sense that the energy is independent of the direction of rotational motion (Atkins et al., 2018). The quantum numbers J and M_J are sufficient for the description of spherical and linear rotor molecules. However, additional quantum numbers are required for more complex molecules with lower symmetry (i.e., prolate and oblate rotors and asymmetric rotors), and if spectral fine and hyperfine structures are considered (Atkins et al., 2018; Gordy and Cook, 1984; Hirota, 2011; Hollas, 2004; Yamamoto, 2017).

In the presence of an external electromagnetic field, interactions between a molecule and the field electrons can give rise to fine-splittings in molecular rotational spectra due to effects like the Zeemann effect (magnetic field) or the Stark effect (electric field) (Gordy and Cook, 1984). For example, the Stark effect partly removes the degeneracy associated with the quantum number $M_J = 0, \pm 1, \pm 2, \ldots, \pm J$ such that the rotational energy levels of a molecule become split into J sub-levels, where each sub-level except the one associated with $M_J = 0$ is doubly degenerate (Atkins et al., 2018; Hollas, 2004). In addition to interactions with external field electrons, "internal" coupling interactions of the electron spin and orbital angular momenta among themselves as well as with the nuclear spin angular momentum and the total molecular angular momentum can cause fine and hyperfine splittings of rotational energy levels. Such interactions occur in molecules with one or more unpaired electrons (often in radicals such as OH^*, CH^*, or CN^*) and/or non-zero electron orbital angular momentum, as well as in molecules with at least one nucleus with non-zero nuclear spin angular momentum. Examples for the latter case include molecules that contain e.g., H ($I = 1/2$), D ($I = 1$), ^{13}C ($I = 1/2$), N ($I = 1$), or ^{15}N ($I = 1/2$); I is the nuclear spin quantum number (Hirota, 2011; Mangum and Y.L. Shirley, 2015; Yamamoto, 2017).

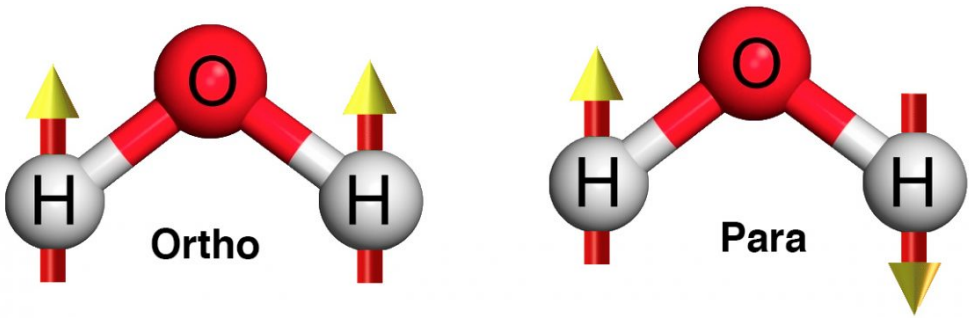

Figure 2.2: Parallel and anti-parallel spins of the otherwise identical hydrogen nuclei in water give rise to two spectroscopically separable forms of water, i.e., ortho-H_2O and para-H_2O. Credit: Natur'Eau Quant (2014).

An important point to note is that some molecules (including H_2, H_2O, CH_3OH, and CH_4) can be spectroscopically separated into two or more symmetry forms based on the relative nuclear spin of their constructing hydrogen nuclei (Chapovsky and Hermans, 1999). For example, the two hydrogen nuclei in water can have parallel spins or anti-parallel spins, leading to the definitions of ortho-H_2O and para-H_2O, respectively (see Fig. 2.2). These two forms of water have not only different rotational energies but also different physical properties (including differences in melting point, boiling point, thermal conductivity, and magnetic properties; London South Bank University, 2009). In addition to such variations, molecules can also have multiple stable atomic configurations (conformers), giving rise to a slightly different rotational behavior, and therefore, different rotational energies. One example is glycine (NH_2CH_2COOH), which has several stable conformers (see also Fig. 1 in paper A; Hu et al., 1993).

In the matrix mechanics formalism, the rotational energy eigenvalues E_J of a molecule can be found by diagonalization of the Hamiltonian matrix for rotational motion $\hat{\boldsymbol{H}}_{\mathbf{r}}$, i.e., (neglecting centrifugal distortion)

$$E_J = \langle \psi_{J,M_J} | \, \hat{\boldsymbol{H}}_{\mathbf{r}} \, | \psi_{J,M_J} \rangle = \langle J, M_J | \, \hat{\boldsymbol{H}}_{\mathbf{r}} \, | J, M_J \rangle \, . \tag{2.4}$$

For a molecule-fixed coordinate system with principal axes a, b, and c, the

rotational Hamiltonian matrix has the form

$$\hat{\boldsymbol{H}}_{\mathbf{r}} = \frac{1}{2}\left(\frac{\hat{\boldsymbol{L}}_a^2}{I_a} + \frac{\hat{\boldsymbol{L}}_b^2}{I_b} + \frac{\hat{\boldsymbol{L}}_c^2}{I_c}\right) = \frac{\hat{\boldsymbol{L}}^2}{2I}\,, \tag{2.5}$$

where $\hat{\boldsymbol{L}}$ is the total angular momentum operator. It can be shown that its corresponding eigenvalues are

$$\langle J, M_J|\, \hat{\boldsymbol{L}}\, |J, M_J\rangle = \hbar J(J+1)\,. \tag{2.6}$$

Furthermore, the eigenvalues of the square magnitude of angular momentum are

$$\langle J, M_J|\, \hat{\boldsymbol{L}}^2\, |J, M_J\rangle = \hbar^2 J(J+1)\,. \tag{2.7}$$

The exact form of the Hamiltonian matrix changes for the different classes of molecules based on their symmetry and the related moment of inertia components (Atkins et al., 2018; Gordy and Cook, 1984; Hollas, 2004; Yamamoto, 2017).

In spectroscopy, the quantity that is actually measured is not energy but frequency[3]. Therefore, energies are commonly converted to so-called term values with dimensions of frequency (Atkins et al., 2018; Yamamoto, 2017). In general, assuming a set of discrete rotational energies $\boldsymbol{E}_{\mathbf{rot}}$, the corresponding term values $\boldsymbol{F}$ are calculated as

$$\boldsymbol{F} = \frac{\boldsymbol{E}_{\mathbf{rot}}}{h}\,. \tag{2.8}$$

Furthermore, using the term value expression, the transition frequency ν for a transition between any two levels with F_i and F_j (where $F_i > F_j$) is given by

$$\nu = F_i - F_j\,. \tag{2.9}$$

A set of such transition frequencies is what generally defines a rotational spectrum. Of course, similar expression are found for electronic or vibrational energies.

[3]Units of wavelength or wavenumber are also used in some spectroscopic disciplines, but I will stick to frequency, which is the commonly used unit in rotational spectroscopy (Hollas, 1998).

It is important to stress that all molecules have a *theoretical* rotational spectrum, but not necessarily an *observable* rotational spectrum. This is due to the fact that not all possible transitions are also allowed. In general, time-dependent perturbation theory is used to derive the spectroscopic selection rules that govern which transitions are allowed and forbidden. Thereby, if the transition rate between two distinct energy levels is zero, this transition is called forbidden. Conversely, all transitions with non-zero transition rates are allowed transitions. By using semi-classical radiation theory, it can be shown that all possible transitions between rotational energy levels of molecules without a permanent electric dipole moment have zero transition rates. Therefore, such molecules are usually not able to produce an observable rotational spectrum. However, even a molecule without a permanent electric dipole moment can produce observable rotational spectral lines if it has e.g., a non-zero magnetic dipole moment or an electric quadrupole moment. The transition rates related to such higher-order poles are however very low. The requirement that a molecule needs to have a permanent electric dipole moment in order to produce an observable rotational spectrum is therefore called the electric dipole approximation (Haken and Wolf, 2006; Norwegian University of Science and Technology, 2023; University of California, Berkeley, 1997). Examples of molecules with higher-order poles observed in the ISM are O_2 and H_2, which both lack an electric dipole moment, but O_2 has a non-zero magnetic dipole moment and H_2 has a non-zero electric quadrupole moment [J. Black; priv. comm.]. In general, most homo-nuclear, di-atomic molecules and all spherical rotor molecules have no permanent electric dipole moment and therefore, no observable rotational spectrum in the electric dipole approximation. However, some spherical molecules like silane (SiH_4) can become sufficiently distorted during rotation to acquire a small electric dipole moment, resulting in observable spectral lines (Atkins et al., 2018).

In addition to entire classes of molecules that have no observable rotational spectra, most pairs of molecular energy levels are characterized by zero transition rates, even for molecules that do have an observable rotational spectrum. For all symmetric rotor molecules, and for the good quantum numbers J and M_J, it can be found that the selection rules for allowed transitions in the

electric-dipole approximation are generally

$$\Delta J = \pm 1 \tag{2.10}$$

and

$$\Delta M_J = 0, \pm 1 \tag{2.11}$$

(Atkins et al., 2018; Gordy and Cook, 1984; Griffiths, 1995; Hollas, 2004; Norwegian University of Science and Technology, 2023; Yamamoto, 2017). There are additional selection rules for prolate and oblate symmetric rotors and asymmetric rotors, as those molecules are governed by additional quantum numbers (see e.g., Atkins et al., 2018; Gordy and Cook, 1984; Hollas, 2004; Yamamoto, 2017).

2.2 Spectral Line Shape

Spectral lines are not actual, infinitely narrow "lines" at one single frequency, but have a width that spreads over a range of frequencies. This width directly depends on the ambient physical conditions, most importantly pressure and temperature, but is also affected by fundamental quantum effects. In the following, the effects of lifetime broadening (section 2.2.1), pressure broadening (section 2.2.2), and thermal Doppler broadening (section 2.2.3), are introduced and discussed for the CO$(1-0)$ spectral line. Only in this section, I will use the symbols "v" for velocity and "f" for frequency, to not confuse v and ν.

2.2.1 Lifetime Broadening and Natural Linewidth

A gas phase molecule that is in a certain state at a certain instant will not remain in that state indefinitely. It will rather change its state by interactions with radiation or other particles (compare sections 1.3.3 and 2.3.1). The lifetime τ and the energy E of a state are related to each other by the uncertainty principle as

$$\Delta\tau \Delta E \approx \hbar\,. \tag{2.12}$$

That is, the energy is uncertain (spread out) as $\Delta E \approx \hbar/\Delta\tau$, from which it follows that the associated frequency f is also spread out over a range of

frequencies as

$$\Delta f = \frac{\Delta E}{h} \approx \frac{1}{2\pi\Delta\tau} \,. \tag{2.13}$$

If the lifetime is very well determined the spread in frequency is at its maximum and the spread in lifetime can be replaced by the value τ, i.e.,

$$\Delta f \approx \frac{1}{2\pi\tau} \,. \tag{2.14}$$

As can be seen, the spread in frequency increases with decreasing lifetime. Spectral lines that result from transitions involving the considered state will be accordingly spread out in frequency. This phenomenon is known as the lifetime broadening of spectral lines (Atkins et al., 2018; Gordy and Cook, 1984; University of St Andrews, 2023).

If it is assumed that a molecule is completely isolated from radiation or other particles it can only change from an excited state u by means of spontaneous emission, characterized by the corresponding Einstein coefficient A_{ul} (see section 1.3.3). The lifetime of the molecule in state u is then given as

$$\tau_{\mathrm{u}} = \frac{1}{A_{\mathrm{ul}}} \,, \tag{2.15}$$

and the resulting spread in frequency of a spectral line is called its natural linewidth (Atkins et al., 2018; Gordy and Cook, 1984; University of St Andrews, 2023).

Considering only the effect of lifetime broadening, the frequency profile of a spectral line $\phi(f)$ is Lorentzian with

$$\phi(f) = \frac{z/4\pi^2}{(f - f_0) + (z/4\pi)^2} \,, \tag{2.16}$$

where

$$z = \sum_{j<i} A_{ij} \,, \tag{2.17}$$

and f_0 is the rest frequency of a given transition. A_{ij} is the Einstein coefficient of spontaneous emission for transitions between levels i and j. Furthermore, in the presence of radiation, the rates of stimulated emission have to be added

as well (University of St Andrews, 2023). The blue line in Fig. 2.3 shows the natural linewidth of the CO$(1-0)$ spectral line with $\nu_0 = 115.271\,\mathrm{GHz}$ and $z = A_{\mathrm{ul}} = 7.2 \times 10^{-8}\,\mathrm{s}^{-1}$, calculated from Eq. (2.16).

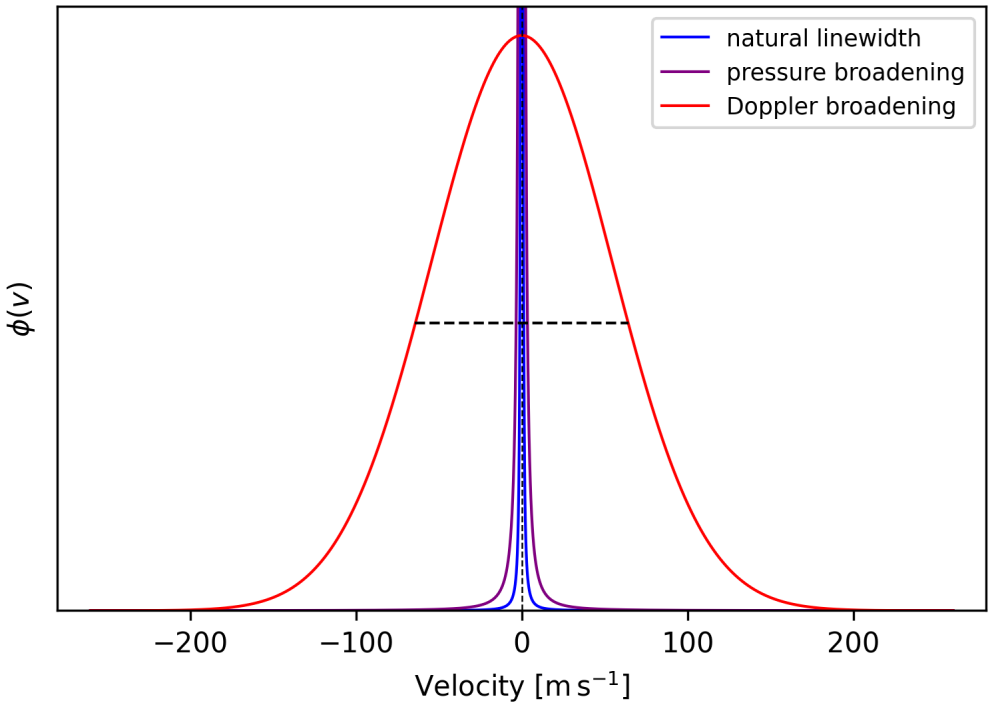

Figure 2.3: Effects of lifetime broadening (Eqs. 2.16 and 2.17; blue line), pressure broadening (Eqs. 2.16 and 2.19; purple line), and thermal Doppler broadening (Eqs. 2.23 and 2.24; red line) on the shape of a CO$(1-0)$ spectral line (see text for further explanations). The frequency axis was converted to velocity by using $v = c(f_0 - f)/f_0$. The vertical dashed black line marks the CO$(1-0)$ rest frequency f_0 at $v = 0$, and the horizontal dashed black line marks the Doppler line width.

2.2.2 Pressure Broadening

Collisions between molecules in the gas phase are an efficient way to induce changes in molecular states (compare section 2.3.1). Considering a collisional de-excitation rate C_{ul} from level u to level l, the collisional lifetime of a state can be defined as

$$\tau_{\mathrm{col}} = \frac{1}{C_{\mathrm{ul}}}\,. \tag{2.18}$$

The associated contribution to the width of a spectral line is referred to as collisional broadening or, because the collision frequency is proportional to pressure, as pressure broadening (Atkins et al., 2018; Gordy and Cook, 1984; University of St Andrews, 2023). Taking into account both the natural linewidth and pressure broadening, the frequency profile $\phi(f)$ is still described by Eq. (2.16), but now

$$z = \sum_{j<i} (A_{ij} + 2C_{ij}) \tag{2.19}$$

(Gordy and Cook, 1984; University of St Andrews, 2023). The purple line in Fig. 2.3 shows the profile of a pressure broadened CO$(1-0)$ line, calculated from Eqs. (2.16) and (2.19). For collision partner H_2, the CO$(1-0)$ collisional rate coefficient is $\gamma_{ul} = 3.3 \times 10^{-11}\,\mathrm{cm^3\,s^{-1}}$ at $T_k = 10\,\mathrm{K}$ (Leiden University, 2023; Schöier et al., 2005). The collisional de-excitation rate is then given as $C_{ul} = n(H_2)\gamma_{ul}$, where $n(H_2)$ is the volume density of H_2. A value of $n(H_2) = 10^{12}\,\mathrm{cm^{-3}}$ has been chosen for the example in Fig. 2.3. At lower values, the pressure broadened line profile coincides with the natural line profile[4]. It follows that the process of pressure broadening is negligible for spectral lines produced by molecules in molecular clouds where H_2 densities are typically in the range of $10^4 - 10^7\,\mathrm{cm^{-3}}$ (van Dishoeck et al., 2013).

2.2.3 Thermal Doppler Broadening

The molecules in a gas mixture move at different velocities v and in different directions relative to an observer at rest. In thermal equilibrium, the velocities are distributed according to a Maxwell-Boltzmann distribution, that depends on the gas temperature. Along the line of sight of the observer, some molecules will approach while others will recede. According to the Doppler effect, the frequency of emitted radiation from the molecules will be different depending on weather they approach or recede. For molecules moving perpendicular to the line of sight, the radiation frequency will be unaffected (Atkins et al., 2018; Gordy and Cook, 1984). Assuming a transition rest frequency f_0 and non-relativistic velocities $v \ll c$, the frequency of radiation emitted by approaching

[4] Considering the collisional rate coefficient for higher temperatures does not change this, as the value of γ_{ul} for CO$(1-0)$ increases only slightly to $3.8 \times 10^{-11}\,\mathrm{cm^3\,s^{-1}}$ at the maximum available temperature of 3 000 K (Leiden University, 2023; Schöier et al., 2005)

and receding molecules is given by

$$f_{\text{app}} = (1 + \frac{v}{c}) f_0 \tag{2.20}$$

and

$$f_{\text{rec}} = (1 - \frac{v}{c}) f_0 \,, \tag{2.21}$$

respectively. That is, the observed frequency will be higher than the rest frequency for approaching molecules, but lower than the rest frequency for receding molecules. The corresponding shift between observed frequency and rest frequency (due to the Doppler effect) is therefore

$$\Delta f_{\text{D}} = f_{\text{obs}} - f_0 = \pm \frac{v}{c} f_0 \tag{2.22}$$

(Atkins et al., 2018). Considering only one velocity component, say v_x, the molecular velocities are Gaussian distributed, from which it follows that the observed frequency shifts will be also Gaussian distributed[5]. Furthermore, the width of the velocity distribution depends on temperature, such that the frequency distribution depends on temperature as well. It is generally increasing with increasing temperature. The broadening of spectral lines due to the described shift of observed frequencies is therefore called (thermal) Doppler broadening (Atkins et al., 2018; Gordy and Cook, 1984; University of St Andrews, 2023).

The frequency profile $\phi(f)$ of a Doppler broadened spectral line is described by the Gaussian profile

$$\phi(f) = \frac{\exp(-\Delta f_{\text{D}}^2 / \delta f_{\text{D}}^2)}{\delta f_{\text{D}} \sqrt{\pi}} \,, \tag{2.23}$$

where

$$\delta f_{\text{D}} = \frac{f_0}{c} \sqrt{\frac{2 k_{\text{B}} T}{m}} \tag{2.24}$$

is the (Doppler) linewidth at half maximum (Atkins et al., 2018; Gordy and Cook, 1984; University of St Andrews, 2023). Turbulent gas motions can be

[5] The consideration of only one velocity component is sufficient for the characterization of the line-of-sight molecular velocities (University of St Andrews, 2023).

considered as well by adding a term for the root-mean square of the turbulent gas velocity s_{turb} to the Doppler linewidth, which then becomes

$$\delta f_{\mathrm{D}} = \frac{f_0}{c}\sqrt{\frac{2k_{\mathrm{B}}T}{m} + s_{\mathrm{turb}}^2} \tag{2.25}$$

(University of St Andrews, 2023). The red line in Fig. 2.3 shows the shape of a Doppler broadened CO$(1-0)$ spectral line. It is calculated from Eqs. (2.23) and (2.24), i.e., without added turbulence, for a temperature of 10 K, typical for cold molecular cloud environments. The horizontal dashed black line shows the Doppler line width. As can be seen, the effect of Doppler broadening clearly dominates over the effects of lifetime broadening and pressure broadening at typical molecular cloud conditions.

The frequency profile of a spectral line considering the combined effect of lifetime broadening, pressure broadening, and Doppler broadening is described by a Voigt profile (convolution of a Lorentzian and a Gaussian profile), which has no simple analytical form. Most basically, a Lorentzian profile falls off slower than a Gaussian profile such that the core of a spectral line is best described by a Gaussian while the wings are better described by a Lorentzian (University of St Andrews, 2023). However, as indicated above, spectral lines emitted by molecules in molecular cloud environments are usually well fitted by simple Gaussians, as their shape is largely dominated by Doppler broadening.

2.3 Population of Molecular Energy Levels

Assuming a large total number of molecules of a particular kind within a molecular cloud source, the physical conditions of the source, most importantly its H_2 density and kinetic temperature, determine the most probable distribution of particles among the distinct rotational energy levels of the molecule. This distribution is commonly referred to as the level population. For a given set of conditions, and within a resulting population, some energy levels are much higher populated than others, meaning that some transitions are much more likely to occur than others. This directly effects the relative strength (or intensity) of spectral lines in a molecular rotational spectrum. In the following, I will briefly describe the basic excitation and de-excitation

processes that govern the level population at each instant, starting from a two-level system (section 2.3.1). Then, the concepts of local thermodynamic equilibrium (LTE; section 2.3.2) and maser emission (section 2.3.3) will be introduced. Lastly, the formulations for the two-level system are expanded to multi-level systems at LTE and non-LTE conditions (sections 2.3.4 and 2.3.5, respectively).

2.3.1 The Two-Level System

In general, only two types of processes can drive transitions between the different energy levels of a molecule, i.e.,

(1) radiative processes,

(2) collisional processes.

Fig. 2.4 summarizes all possible radiative and collisional processes in terms of the involved coefficients. Shown is an exemplary two-level system, consisting of a lower energy level l and an upper energy level u, separated by an energy ΔE.

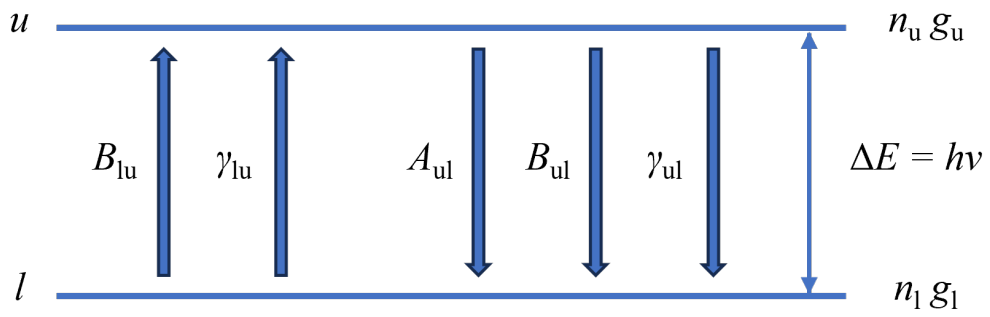

Figure 2.4: Transitions between the energy levels of a two-level system are driven by radiative processes (B_{lu}, B_{ul}, and A_{ul}) and collisional processes (γ_{lu} and γ_{ul}). ΔE is the energy separation between both levels, n_u and n_l are the numbers of molecules in the upper and lower levels, respectively, and g_u and g_l are the statistical weights of both levels.

An overview about radiative processes, in which photons are either absorbed or emitted during transitions between energy levels, is already given in section 1.3.3. As a recap, and assuming there is some radiation to interact

with the molecules, radiative processes can either cause excitation $l \rightarrow u$ by means of stimulated absorption, or de-excitation $u \rightarrow l$ by means of stimulated and spontaneous emission. Thereby, the rates of absorption and total emission depend on (i) the spectral intensity of incoming radiation at the transition frequency $\nu = \Delta E/h$, (ii) the number of particles in the lower level n_l (absorption) or in the upper level n_u (emission), and (iii) a coefficient that depends on the molecular species and the considered level pair, i.e., B_lu (absorption), B_ul (stimulated emission), and A_ul (spontaneous emission).

Collisional processes are those in which excitation and de-excitation is driven by collisions between molecules with other particles in the gas phase, typically other molecules, atoms, ions, or electrons. Unlike radiative transitions, collisional transitions are generally not confined by strict selection rules (Tennyson and Faure, 2019), such that collisional transitions can, in principle, also occur between distant pairs of J-levels. However, it can be generally assumed that the collisional transition probability decreases with increasing ΔJ, i.e., with increasing ΔE, such that a large number of transitions with very low transition probability can be excluded from the set of possible transitions [P. Bergman; priv. comm.].

The rates of collisional excitation and de-excitation between two levels u and l, i.e., C_lu and C_ul, respectively, are highly species dependent and related to each other as

$$\frac{g_\mathrm{l} C_\mathrm{lu}}{g_\mathrm{u} C_\mathrm{ul}} = \exp\left(-\frac{h\nu}{k_\mathrm{B} T_\mathrm{k}}\right), \tag{2.26}$$

where T_k is the kinetic temperature (Yamamoto, 2017). Values of C_ul can be derived from tabulated values of so-called collisional rate coefficients γ_ul as

$$C_\mathrm{ul} = n(\mathrm{X})\gamma_\mathrm{ul}\,, \tag{2.27}$$

where $n(\mathrm{X})$ is the number volume density of the collision partner (van der Tak et al., 2007). Commonly, γ_ul has units of $\mathrm{cm}^3\,\mathrm{s}^{-1}$, and tabulated values can be found in databases for different collision partners, kinetic temperatures, and level pairs. Obtained values of C_ul can then be related to C_lu via Eq. (2.26). Most basically, collisional rate coefficients are calculated from the potential energy surface of interaction between the collision partners, which is then used

in a quantum scattering calculation to derive collisional cross sections $\sigma_{\rm ul}$ for transitions between levels u and l. The thermal average of the cross sections is then calculated over a range of collisional energies $E_{\rm c}$, and used as a major input to calculate the rate coefficient as

$$\gamma_{\rm ul}(T_{\rm k}) = \left[\frac{8}{\pi\mu(k_{\rm B}T_{\rm k})^3}\right]^{1/2} \int_0^\infty E_{\rm c}\sigma_{\rm ul}(E_{\rm c}) \exp\left(-\frac{E_{\rm c}}{k_{\rm B}T_{\rm k}}\right) {\rm d}E_{\rm c}\,, \tag{2.28}$$

where $\mu = m_A m_B/(m_A + m_B)$ is the reduced mass of collision partners A and B, having masses m_A and m_B (Dagdigian, 2019; Lique et al., 2020). Collisional coefficients are extremely difficult to measure in the laboratory and astronomical models rely almost exclusively on theoretical calculations (Faure, 2019). If collisional coefficients are not available in a database for a certain molecule it is common to use the coefficients for a similar-sized molecule. For a typical molecular cloud environment, it is often assumed that collisional excitation and de-excitation is entirely driven by collisions between a target molecule and molecular hydrogen, because H_2 is by far the most abundant other molecule in the gas phase. However, also collisions with hydrogen atoms and electrons can be important under certain circumstances[6] (Yamamoto, 2017).

Considering all radiative and collisional excitation and de-excitation processes for a two-level system, affected by a radiation field with spectral intensity I_ν, the number of molecules n in the lower level changes over time according to

$$\frac{{\rm d}n_{\rm l}}{{\rm d}t} = A_{\rm ul}n_{\rm u} + B_{\rm ul}n_{\rm u}I_\nu + C_{\rm ul}n_{\rm u} - B_{\rm lu}n_{\rm l}I_\nu - C_{\rm lu}n_{\rm l}\,. \tag{2.29}$$

By using the relations between the Einstein coefficients (Eqs. 1.20 and 1.21), as well as the relation between the collisional excitation and de-excitation rates (Eq. 2.26), Eq. (2.29) can simply be written as

$$\frac{{\rm d}n_{\rm l}}{{\rm d}t} = \beta n_{\rm l} + \delta n_{\rm u} = 0\ , \tag{2.30}$$

[6] Even collisions with water molecules can be important e.g., in cometary comae [P. Bergman, E. Wirström; priv. comm.].

where

$$\beta = -\frac{g_\mathrm{u}}{g_\mathrm{l}}\left[A_\mathrm{ul}\frac{c^2}{2h\nu^3}I_\nu + C_\mathrm{ul}\exp\left(-\frac{h\nu}{k_\mathrm{B}T_\mathrm{k}}\right)\right] \tag{2.31}$$

and

$$\delta = A_\mathrm{ul}\frac{c^2}{2h\nu^3}I_\nu + A_\mathrm{ul} + C_\mathrm{ul}\,. \tag{2.32}$$

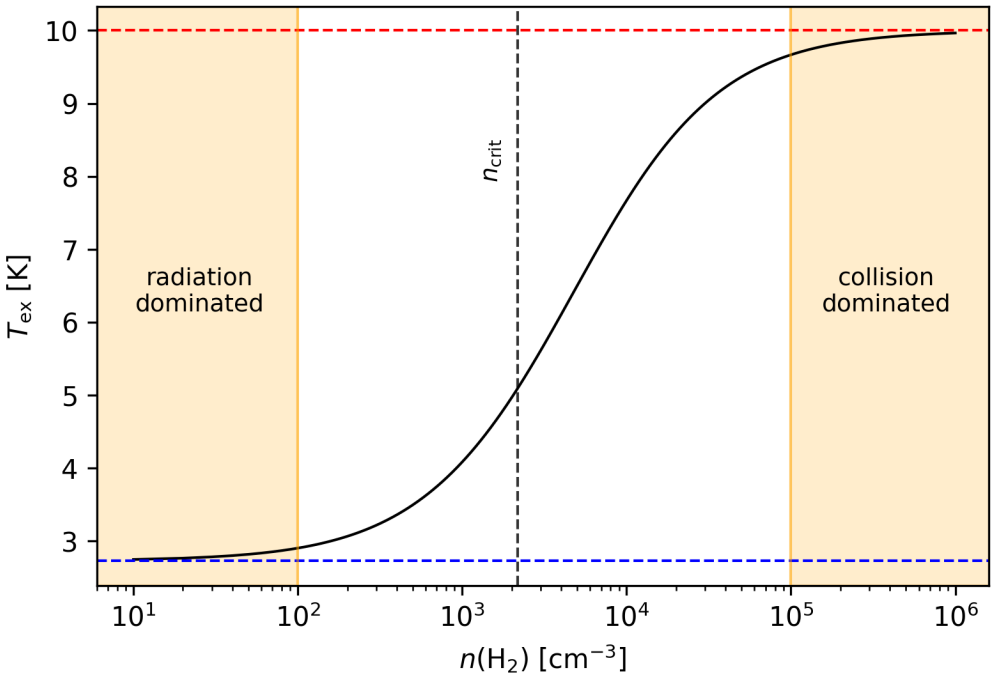

Figure 2.5: Excitation temperature T_ex corresponding to the level population $n_\mathrm{u}/n_\mathrm{l}$ of the CO$(1-0)$ two-level system as a function of H_2 density, calculated from Eq. (2.34). The population of levels is calculated from Eqs. (2.30) and (2.33). As can be seen, T_ex approaches the assumed background temperature (2.725 K; dashed blue line) at low densities, but the assumed kinetic temperature (10 K; dashed red line) at high densities. The shaded orange areas mark the approximate densities at which the underlying population of levels is dominated by either radiation or collisions. The vertical dashed black line labelled "n_crit" marks the critical density of CO$(1-0)$, as calculated from Eq. (2.37).

It is furthermore assumed that a steady state is obtained for the energy level population ($\mathrm{d}n_\mathrm{l}/\mathrm{d}t = 0$). When considering particle conservation, i.e.,

the requirement that

$$n_\mathrm{l} + n_\mathrm{u} = n_\mathrm{tot}\,, \tag{2.33}$$

Eqs. (2.30) and (2.33) give a system of equations that can be solved for n_l and n_u [P. Bergman; priv. comm.].

This is done in the following for the CO$(1-0)$ two-level system, which is characterized by $g_\mathrm{u}/g_\mathrm{l} = 3$, $\nu = 115.271\,\mathrm{GHz}$, $A_\mathrm{ul} = 7.2 \times 10^{-8}\,\mathrm{s}^{-1}$, and $\gamma_\mathrm{ul} = 3.2 \times 10^{-11}\,\mathrm{cm}^3\,\mathrm{s}^{-1}$ (for collisions with H_2 at $T_\mathrm{k} = 10\,\mathrm{K}$) (Leiden University, 2023; Schöier et al., 2005). The spectral intensity of radiation is assumed to be described in terms of blackbody radiation at temperature $T_\mathrm{bg} = T_\mathrm{CMB} \approx 2.725\,\mathrm{K}$, i.e., $I_\nu = B_\nu(T_\mathrm{bg})$, where T_CMB is the temperature of the cosmic microwave background. Level populations are calculated for this system for $n_\mathrm{tot} = 100\,\mathrm{cm}^{-3}$, $T_\mathrm{k} = 10\,\mathrm{K}$, and $n(H_2) \in [10, 10^6]\,\mathrm{cm}^{-3}$. The value of $n(H_2)$ determines the collisional de-excitation rate C_ul via Eq. (2.27), and eventually, each value of $n(H_2)$ gives a unique level population $n_\mathrm{u}/n_\mathrm{l}$, which is related to one specific "excitation" temperature T_ex via the Boltzmann distribution (Eq. 1.6) as

$$\frac{n_\mathrm{u}}{n_\mathrm{l}} = \frac{g_u}{g_l} \exp\left(-\frac{h\nu}{k_\mathrm{B} T_\mathrm{ex}}\right)\,. \tag{2.34}$$

Fig. 2.5 shows the change in excitation temperature as a function of H_2 density. As can be seen, T_ex approaches T_bg at low densities, but T_k at high densities. This is due to the fact that in Eqs. (2.31) and (2.32), the terms including A_ul dominate at low densities, whereas the terms including C_ul dominate at high densities. In these two limits, the relative population of levels n_u and n_l can therefore be approximated as

$$\frac{n_\mathrm{u}}{n_\mathrm{l}} \approx \frac{g_u}{g_l} \exp\left(-\frac{h\nu}{k_\mathrm{B} T_\mathrm{bg}}\right)\,, \tag{2.35}$$

and

$$\frac{n_\mathrm{u}}{n_\mathrm{l}} \approx \frac{g_u}{g_l} \exp\left(-\frac{h\nu}{k_\mathrm{B} T_\mathrm{k}}\right)\,, \tag{2.36}$$

respectively. That is, in the low density limit, the level population is thermalized by the background radiation, while in the high density limit, the level population is thermalized by collisions between particles in the gas (shaded orange areas in Fig. 2.5). In intermediate areas, the level population is deter-

mined by a combination of radiation and collisions (Yamamoto, 2017).

In order to observe emission from an interstellar molecule, and to prevent cooling by radiation, the upper energy level of a specific transition must be sufficiently populated by collisions. The H_2 density necessary to fulfill that criterion can be estimated (to an order-of-magnitude) by equilibrating the collision and emission rates, i.e., $C_{\rm ul} = A_{\rm ul}$. The so-called critical H_2 density then follows from Eq. (2.27) as

$$n_{\rm crit}(H_2) = \frac{A_{\rm ul}}{\gamma_{\rm ul}} \tag{2.37}$$

(Yamamoto, 2017). The critical H_2 density for the CO(1 − 0) two-level system is plotted as the vertical dashed black line in Fig. 2.5. Critical densities can be directly related to the typical spatial distribution of observed emission for certain interstellar molecules. For example, the $J = 1 - 0$ transitions of HCN has a spontaneous emission coefficient of $2.4 \times 10^{-5}\,{\rm s}^{-1}$ and a collisional rate coefficient of $2.4 \times 10^{-11}\,{\rm cm}^3\,{\rm s}^{-1}$. Therefore, the critical density of HCN(1−0) is $\sim 1 \times 10^6\,{\rm cm}^{-3}$, as compared to $\sim 2 \times 10^3\,{\rm cm}^{-3}$ for CO(1 − 0). This means that CO(1 − 0) emission can arise from regions with far lower density compared to HCN(1 − 0) (Yamamoto, 2017).

The described excitation and de-excitation processes can be directly transferred to multi-level systems, as is done in sections 2.3.4 and 2.3.5. Thereby, the set of allowed collisional transitions is always larger than the set of allowed radiative transitions, because collisional transitions are not confined by strict selection rules.

2.3.2 Local Thermodynamic Equilibrium

Assuming a system of molecules of the same kind and a large number of energy levels (i.e., a multilevel system), we can separate three possible equilibrium cases:

(1) statistical equilibrium,

(2) thermal equilibrium,

(3) thermodynamic equilibrium.

In each of these cases, no net change is observed in the total energy level population over time, i.e., there is a constant number of molecules in each energy level i, giving $\mathrm{d}n_i/\mathrm{d}t = 0$. Then, each pair of energy levels $n_\mathrm{u}/n_\mathrm{l}$ is characterized by an excitation temperature T_ex, according to Eq. (2.34). If the excitation temperature changes from one level pair to another, the system is in statistical equilibrium. If, on the other hand, the excitation temperature is constant for all level pairs, the system is in thermal equilibrium, and the level population is well described by a Boltzmann distribution (Eq. 1.6) at that temperature. The system is furthermore in thermodynamic equilibrium, if the constant temperature is equal to the thermodynamic temperature T of the system. It is common to separate a large system into subsystems, and to allow for variations in e.g., temperature and pressure between the subsystems, while assuming that each subsystem for itself is in so-called local thermodynamic equilibrium (LTE).

Based on the above definitions, both the low-density and high-density limits introduced in the previous section via Eqs. (2.35) and (2.36), respectively, are describing systems in thermal equilibrium. In the low-density limit, where the level population is determined by the radiation background temperature T_bg, the thermal equilibrium can be further specified as a radiative equilibrium. Systems in the high-density limit, characterized by the (H_2) kinetic temperature T_k of the system, are often assumed to be not only in thermal equilibrium but in (local) thermodynamic equilibrium. Therefore, whenever discussing "LTE conditions" in the following text, it will be assumed that $T_\mathrm{ex} = T_\mathrm{k} = T$. However, because this equality is often just an approximation, I will not make the replacements in the equations. Furthermore, whenever discussing "non-LTE conditions", I am referring to conditions in which a system is neither in thermodynamic nor in thermal equilibrium, but in statistical equilibrium, i.e., to conditions in which T_ex must be considered as a variable. It should be however noted that the possibility of having thermal equilibrium is not strictly excluded from the term "non-LTE conditions", when considering that a system can be in thermal equilibrium without being in thermodynamic equilibrium.

In astrochemical studies of molecular clouds, it is common to start from the assumption of LTE conditions. However, if LTE conditions are evidently not

met for a molecular species in a certain source region, non-LTE treatments must be considered[7]. As will be discussed in section 2.5.4, the population diagram method can be used as an indicator if LTE conditions are met. In general, the distinction between LTE and non-LTE conditions is crucial for the analysis and modelling of spectral line data, and will be discussed further at various places in the following sections.

2.3.3 Maser Emission

Usually, the lower energy level of a pair of levels is higher populated than the upper level, giving $n_{\rm u}g_{\rm l}/n_{\rm l}g_{\rm u} < 1$. However, for certain level pairs and under specific conditions, the upper level can become higher populated than the lower level, i.e., $n_{\rm u}g_{\rm l}/n_{\rm l}g_{\rm u} > 1$, which is called population inversion. This arises from highly non-LTE conditions because, according to Eq. (2.34), an inverted population always corresponds to a negative excitation temperature. Population inversion results in an exponential amplification of stimulated emission by the background radiation, and the corresponding phenomenon is known as microwave amplification of stimulated emission of radiation (maser). However, population inversion only occurs for certain molecules, for a limited number of level pairs, and in a limited range of physical conditions. Therefore, maser emission, though very bright, often originates from localized source regions. In the interstellar medium, maser emission has been observed for some transitions of e.g., OH, SiO, H_2O, H_2CO, and CH_3OH (Yamamoto, 2017).

2.3.4 Multilevel Systems at LTE Conditions

At LTE conditions, the energy level population of a multi-level system is simply described in terms of a Boltzmann distribution at (thermodynamic) temperature $T = T_{\rm ex}$, which is often assumed as the (H_2) gas kinetic temperature $T_{\rm k}$ in a molecular cloud setting. Thereby, the population n_i of the energy level with energy E_i relative to the population n_j of another energy level with $E_j < E_i$, as well as relative to the total particle population $n_{\rm tot}$ is

[7] Because excitation and de-excitation rates are highly species-dependent, it can differ from species to species if LTE conditions are met or not.

respectively determined from Eqs. (1.6) and (1.1), written slightly adjusted as

$$\frac{n_i}{n_j} = \frac{g_i}{g_j} \exp\left(-\frac{h\nu}{k_\mathrm{B} T_\mathrm{ex}}\right) \tag{2.38}$$

and

$$\frac{n_i}{n_\mathrm{tot}} = \frac{g_i}{Q_\mathrm{rot}} \exp\left(-\frac{E_i}{k_\mathrm{B} T_\mathrm{ex}}\right), \tag{2.39}$$

where Q_rot is the so-called rotational partition function, defined via Eq. (1.5) as

$$Q_\mathrm{rot} = \sum_i g_i \exp\left(-\frac{E_i}{k_\mathrm{B} T_\mathrm{ex}}\right). \tag{2.40}$$

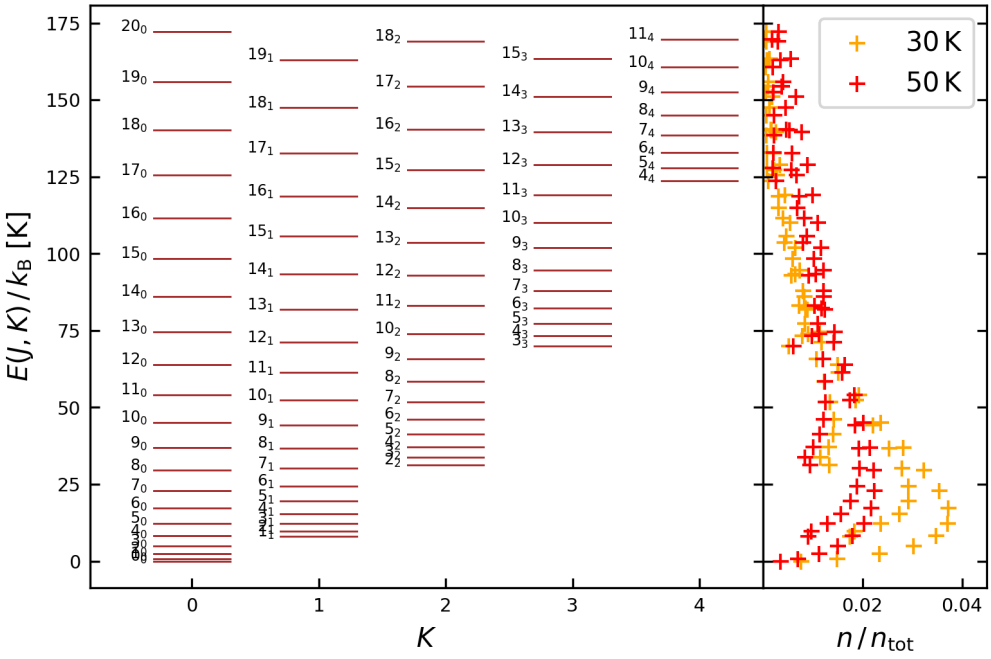

Figure 2.6: Left: rotational energy level diagram of the prolate rotor methyl acetylene (CH_3CCH), created from tabulated values in CDMS (Cologne Database for Molecular Spectroscopy; https://cdms.astro.uni-koeln.de/; Müller et al., 2001, 2005), and showing energy levels with $E(J, K) < 175\,\mathrm{K}$. **Right:** equilibrium energy level population, calculated from Eq. (2.39) for two different excitation temperatures T_ex, i.e., 30 K (orange marks) and 50 K (red marks). Credit: P. Bergman (OSO) for providing the PYTHON-code used to create this plot.

The left panel of Fig. 2.6 shows the rotational energy level diagram of methyl acetylene (CH_3CCH) for energy levels with $E(J, K) < 175\,\mathrm{K}$. Furthermore, the right panel shows the equilibrium population of energy levels, calculated from Eq. (2.39) for two different excitation temperatures T_{ex}, i.e., 30 K (orange marks) and 50 K (red marks). As can be seen, higher energy levels get populated at the expense of lower energy levels as the temperature increases. Because the population in a certain upper level is directly proportional to the emission rate of photons during transitions $u \rightarrow l$, the equilibrium temperature directly affects the set and relative strengths of observable spectral lines (see discussion of the population diagram method in section 2.5.4). In the particular case shown in Fig. 2.6 (right) for 30 K, the level population is narrow and concentrated in the lower energy level range. This leads to a relatively small set of observable spectral lines with comparatively high individual intensities. On the other hand, at 50 K, the level population is broader, leading to a larger set of spectral lines with lower individual intensities. That is, the total intensity of CH_3CCH emission gets distributed over a larger number of spectral lines with increasing temperature. However, under the assumption of thermal radiation, the total intensity is still increasing with increasing temperature.

2.3.5 Multilevel Systems at non-LTE Conditions

Assuming that the system of molecules is neither in LTE nor in thermal equilibrium, but in statistical equilibrium (SE), each pair of energy levels in the total energy level population has its own characteristic excitation temperature, according to Eq. (2.34). In this case, there is no trivial, analytical way to determine the total energy population for a (rotational) energy level system. Instead, numerical approaches have to be used that aim to solve a set of differential equations, where each equation is similar to the one stated for the two-level system (Eq. 2.29). The basic principle is the same: each equation considers the change in the population of one level over time according to the rates of radiative and collisional transitions. However, in the case of a multilevel system, there are a multitude of possible excitation and de-excitation processes, especially considering that significant collisional transitions can be caused between many pairs of levels. Most basically, assuming a total number of N energy levels and a radiation source with spectral intensity I_ν to interact

with the molecules, the set of differential equations to be solved can be written compactly as

$$\frac{\mathrm{d}n_i}{\mathrm{d}t} = \sum_{j\neq i}^{N} n_j P_{ji} - n_i \sum_{j\neq i}^{N} P_{ij} = 0\,, \tag{2.41}$$

where

$$P_{ij} = \begin{cases} A_{ij} + B_{ij} I_\nu + C_{ij} & \text{, if } i > j \\ B_{ij} I_\nu + C_{ij} & \text{, if } i < j \end{cases} \tag{2.42}$$

(Rybicki and Hummer, 1991; van der Tak et al., 2007). In the case of a multilevel system and a total number of molecules n_{tot}, particle conservation requires that

$$\sum_{i}^{N} n_i = n_{\mathrm{tot}}\,. \tag{2.43}$$

It will be discussed in section 2.4.5 how the above set of equations can be implemented into physical models describing the radiation intensity from cold molecular cloud sources at non-LTE conditions.

2.4 Observing Radiation From Cold Molecular Clouds

Molecules in cold molecular cloud environments are emitting radiation as spectral lines over narrow frequency intervals. In order to analyse the abundances of molecules in a certain source region, the emitted spectral intensity I_ν from that source must be captured with a radio telescope in a certain bandwidth. Some background to the measurement and calibration of radio signals is given in section 2.4.1, focusing on observations with single-dish telescopes. An introduction to the radiative transfer equations used to describe the intensity from a source is then given in section 2.4.2. Afterwards, the equations for the description of spectral line radiation are specified in section 2.4.3. Lastly, sections 2.4.4 and 2.4.5 are covering the treatment and interpretation of spectral line radiation for the cases of having molecules at LTE and non-LTE conditions, respectively.

2.4.1 Temperature Intensity Scale and Instrumentation Effects

Radio astronomers are often operating in the limit $h\nu \ll k_{\mathrm{B}}T$, such that the received intensity I_ν from a source can be well described by the Rayleigh-Jeans approximation (Eq. 1.10) (Condon and Ransom, 2016; Yamamoto, 2017). By using this relation, the source intensity at a certain frequency ν can also be expressed in terms of the corresponding source temperature T_{S} as

$$T_{\mathrm{S}}(\nu) = \frac{I_\nu c^2}{2k_{\mathrm{B}}\nu^2}\,. \tag{2.44}$$

However, when measured with a radio antenna, the source signal is superimposed on signals from the cosmic microwave background (T_{CMB}), other radio background sources in the sky (T_{sky}), the atmosphere (T_{atm}), the ground beneath the antenna (T_{ground}), and the receiver system (T_{RX})[8]. The overlay of the measured signals is what defines the total system temperature, i.e.,

$$T_{\mathrm{sys}} = T_{\mathrm{S}} + T_{\mathrm{CMB}} + T_{\mathrm{sky}} + T_{\mathrm{atm}}\left[1 - \mathrm{e}^{\tau_\nu^{\mathrm{atm}}}\right] + T_{\mathrm{ground}} + T_{\mathrm{RX}} + \dots\,, \tag{2.45}$$

where τ_ν^{atm} is the optical depth of the atmosphere at frequency ν (Condon and Ransom, 2016). Of course, the system temperature and all contributions to it are frequency-dependent, but for simplicity, this dependence is neglected in the notation above. The system temperature further defines the RMS (root mean square) noise temperature σ_T, which is approximately given by the ideal radiometer equation as

$$\sigma_T \approx \frac{T_{\mathrm{sys}}}{\sqrt{\Delta\nu t_{\mathrm{int}}}}\,, \tag{2.46}$$

where t_{int} is the integration time, and $\Delta\nu$ is the bandwidth (Condon and Ransom, 2016). As can be seen, the system noise can be largely reduced by using longer integration times. In addition, different calibration and switching methods are used to minimize the effects from distracting signals, and to filter out the desired source signal.

When targeting an astronomical source with a telescope inside of Earth's

[8] Additional noise sources arise from artificial radio frequency interference (RFI) from e.g., television, radio, and mobile network.

atmosphere, the source signal gets attenuated by the optical depth of the atmosphere at the observed wavelength. However, the optical depth is not strictly constant, but changes over time due to short-term changes in atmospheric conditions, including temperature, pressure, and humidity. An integral part of all observation runs is therefore the repeated determination of those parameters, followed by the calibration of the receiver system to the determined values. Thereby, the intervals between calibration measurements depend on the actual weather conditions. In radio astronomy, a common calibration method is the so-called chopper-wheel method (Jewell, 2002; Wilson, 2013).

In Eq. (2.45), the contribution from the receiver system is commonly minimized by cooling it to cryogenic temperatures. Effects from the CMB, other radio background sources, the atmosphere, and the ground, are furthermore minimized by using different switching methods like position-switching, beam-switching, and frequency-switching. In position- and beam-switching, the signal from a reference position at a certain offset from the source is measured in repeating intervals during an observation run, and then subtracted from the source signal. Thereby, the offset to the source position must be large enough such that it is completely free of any target radiation. In position-switching, the main reflector of the telescope is moved to switch between both positions, while in beam-switching, only the sub-reflector is moved. Therefore, the offset can be arbitrary in position-switching, but is limited in beam-switching due to mechanical reasons. The switching is faster and more stable with beam-switching, but the maximum offset must be considered when observing very extended sources. It is common to observe the same time on-source and off-source. In frequency switching, the center frequency is switched to an offset frequency for half of the observation time, and the spectra observed at the offset frequency are then subtracted from those observed at the center frequency. This switching method can save plenty of observation time as the spectra at offset frequency still contain the signal and can be integrated together with the spectra at center frequency after some processing. However, this method is most suitable for observations of a limited number of known target signals, because there is otherwise the risk of loosing signal during subtraction [E. Wirström, P. Bergman, C. Horellou; priv. comm.].

The underlying principle in the three switching methods is essentially the same. That is, during approximately half of the observation time, either the on-source or on-frequency intensity I_ν^{on} is measured in a certain bandwidth, while the remaining observation time is used to observe the off-source or off-frequency intensity I_ν^{off}. The intensity difference

$$\Delta I_\nu = I_\nu^{\mathrm{on}} - I_\nu^{\mathrm{off}} \tag{2.47}$$

is then obtained and converted to the corresponding radiation temperature T_{R}, which is given as

$$T_{\mathrm{R}}(\nu) = \frac{\Delta I_\nu c^2}{2k_{\mathrm{B}}\nu^2} \tag{2.48}$$

in the Rayleigh-Jeans limit (Mangum and Y.L. Shirley, 2015; Wilson, 2013; Yamamoto, 2017). This temperature is now very close to the desired source temperature as would be measured by a radio telescope outside of Earth's atmosphere.

It is important to note that the source temperature T_{S} is related to the spatial extension of the source on the sky via the source solid angle Ω_{S}. That is, the effective units of source spectral intensity in the temperature scale are $\mathrm{K\,sr^{-1}}$. It follows that also the radiation temperature T_{R} measured for a source against a reference position depends on the solid angle of the source. Thereby, the source temperature distribution is usually described in terms of a Gaussian distribution. Furthermore, the actually measured antenna temperature of a telescope is given as

$$T_{\mathrm{A}}(\nu) = \frac{P_\nu}{k_{\mathrm{B}}}\,, \tag{2.49}$$

where P_ν is the received spectral power. Essentially, the antenna temperature is an average over the beam solid angle Ω_{A}, which is frequency-dependent and has Gaussian shape (see next paragraph). When pointing an antenna at a source with Ω_{S}, the antenna temperature, radiation temperature, source solid angle, and beam solid angle are related as

$$\frac{T_{\mathrm{A}}(\nu)}{T_{\mathrm{R}}(\nu)} = \frac{\Omega_{\mathrm{S}}}{\Omega_{\mathrm{A}}(\nu)} = f\,, \tag{2.50}$$

where f is called the filling factor (Condon and Ransom, 2016; Mangum and

Y.L. Shirley, 2015; Wilson, 2013). That is, if a source fills the entire antenna beam, $f = 1$, and the measured antenna temperature is a good measure of the source temperature distribution, i.e., $T_{\rm A} = T_{\rm R}$. On the other hand, if the source solid angle is smaller than the beam solid angle (e.g., for a point source), $f < 1$, and the measured antenna temperature is only a fraction of the source temperature, i.e., $T_{\rm A} = fT_{\rm R}$. This effect is commonly called beam dilution. However, for extended sources in nearby molecular clouds, it can often be assumed that $f = 1$ (Wilson, 2013). Nevertheless, the effect of beam size must be considered with care when dealing with e.g., emission from more complex molecules that might originate from only a small sub-region of a source, or with maser emission, which always originates from very small sub-regions (see section 2.3.3) [E. Wirström, P. Bergman; priv. comm.]. Choosing a single-dish telescope with a higher angular resolution (smaller beam) or an interferometer can be appropriate in such cases.

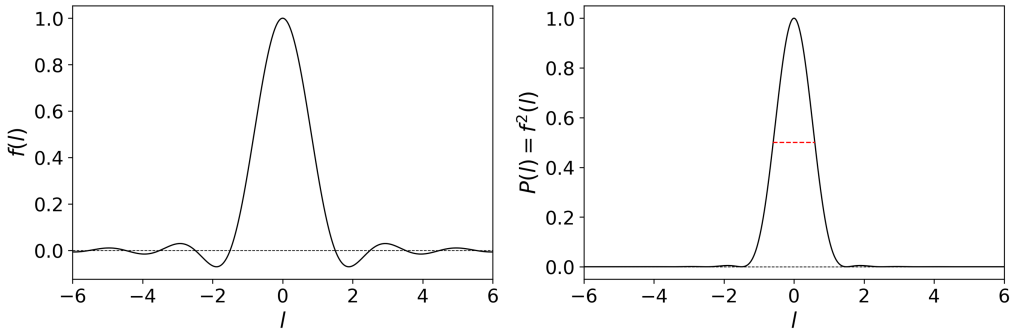

Figure 2.7: Left: field pattern $f(l)$ of a parabolic reflector, calculated from Eq. (2.51). **Right:** power pattern $P(l) = f^2(l)$ of a parabolic reflector.

The beam size of a single-dish antenna is derived from the power pattern of a parabolic reflector, which is given by the square of the electric field pattern. Assuming a cosine-tapered illumination by incoming plane waves from a far distant source, the electric field pattern of a parabolic reflector can be written as

$$f(l) = \frac{\cos \pi l}{1 - 4l^2}\,, \tag{2.51}$$

where l is a measure of the reflection angle at different points of the reflector (Condon and Ransom, 2016). Fig. 2.7 shows a plot of the field pattern (left), and the corresponding power pattern $P(l) = f^2(l)$ (right). The beam size θ

(in radian) is commonly expressed in terms of the so-called half-power beam width (HPBW), which can be approximated as

$$\theta_{\mathrm{HPBW}}(\lambda) \approx 1.2\,\frac{\lambda}{D}\,, \tag{2.52}$$

where λ is the wavelength of incoming radiation, and D is the aperture diameter (Condon and Ransom, 2016). The half-power beam width is indicated by the red dashed line in Fig. 2.7 (right). It can be furthermore shown that a two-dimensional Gaussian beam covers a solid angle of approximately

$$\Omega_{\mathrm{A}}(\lambda) \approx 1.133\,\theta_{\mathrm{HPBW}}(\lambda)^2 \tag{2.53}$$

(Condon and Ransom, 2016).

There are some further steps and requirements to make sure that the antenna gain $G(\nu, \theta, \psi)$ (which is directly proportional to the received spectral power) is always at maximum during observations. First of all, the gain depends on the surface accuracy η_{surf} of a parabolic dish, which can of course not be modified during observations but is set during telescope construction. If σ_{surf} is the surface error and λ is the wavelength of observation, the surface accuracy is given by

$$\eta_{\mathrm{surf}}(\lambda) = \exp\left[-\left(\frac{4\pi\sigma_{\mathrm{surf}}}{\lambda}\right)^2\right]. \tag{2.54}$$

Essentially, a radio telescope works reasonably well for wavelengths $\lambda > 16\sigma_{\mathrm{surf}}$ (Condon and Ransom, 2016) (see Fig. 2.8, left). Another requirement in order to maximize the gain during an observation is that the telescope is pointed straight at the source at every time with highest precision. If G_0 is the peak gain of a dish, the fractional gain G/G_0 is a function of the pointing error σ_{point}, i.e.,

$$\frac{G}{G_0} = \exp\left[-4\ln 2\left(\frac{\sigma_{\mathrm{point}}}{\theta_{\mathrm{HPBW}}}\right)^2\right] \tag{2.55}$$

(Condon and Ransom, 2016). Thus, keeping pointing errors within 10 % of the beam size ensures that the gain G is $> 97\,\%$ of the peak gain G_0 (see Fig. 2.8, right). Another important definition is the main beam solid angle

Ω_{mb}, defined via the gain as

$$\Omega_{\mathrm{mb}}(\nu) = \frac{1}{G_0} \int_{\mathrm{mb}} G(\nu, \theta, \psi)\, \mathrm{d}\Omega\,. \tag{2.56}$$

Essentially, the main beam is the region in Fig. 2.7 (right) that contains the principal response out to the first zero. Any responses outside this region are called sidelobes, or very far from it, stray radiation. The main beam solid angle is related to the (total) beam solid angle as

$$\eta_{\mathrm{mb}}(\nu) = \frac{\Omega_{\mathrm{mb}}(\nu)}{\Omega_{\mathrm{A}}(\nu)}\,, \tag{2.57}$$

where η_{mb} is called the main beam efficiency. With the definition of main beam efficiency, the measured antenna temperature is usually converted to the so-called main beam temperature

$$T_{\mathrm{mb}}(\nu) = \frac{T_{\mathrm{A}}(\nu)}{\eta_{\mathrm{mb}}(\nu)}\,, \tag{2.58}$$

which then provides a better estimate for the actual source temperature (Condon and Ransom, 2016).

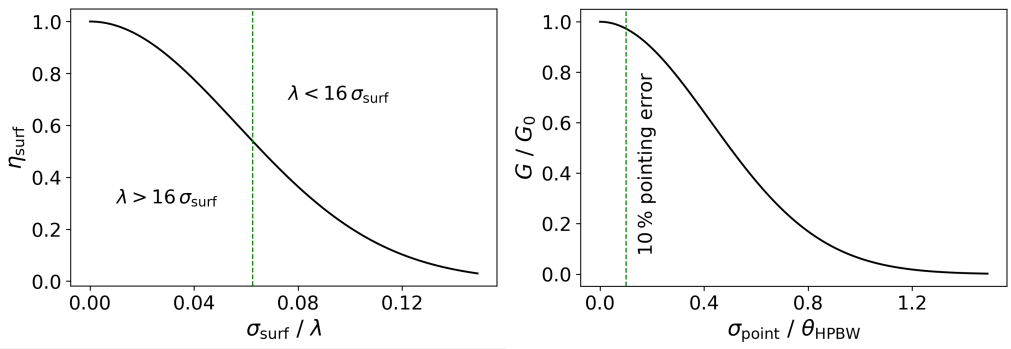

Figure 2.8: Left: surface accuracy η_{surf} of a parabolic dish, calculated from Eq. (2.54). A radio telescope works reasonably well for $\lambda > 16\sigma_{\mathrm{surf}}$. **Right:** fractional gain G/G_0 of a telescope as a function of pointing error σ_{point}.

2.4.2 Radiative Transfer and Source Intensity

The intensity from a cold molecular cloud source is conceptually defined via the equations of radiative transfer. Then, it is assumed that the cloud interacts with some background radiation field, having spectral intensity $I_\nu = B_\nu(T_{\mathrm{bg}})$. Upon entering the molecular cloud, the background radiation will start to interact with molecules inside the cloud by means of absorption and stimulated emission, causing transitions between energy levels and the absorption and emission of photons. In addition, the molecules release photons by means of spontaneous emission. Furthermore, collisions between molecules and other particles in the cloud lead to further transitions between energy levels (compare section 2.3). Thereby, every emitted photon in the cloud can interact with molecules in between the position of release and the edge of the cloud, leading to a non-trivial chain of absorption and emission processes. The effectiveness of these processes depends on the composition and physical conditions (largely density and temperature) of the cloud, but can be generally quantified in terms of the absorbance α_ν (m^{-1}) and the emissivity ϵ_ν ($\mathrm{W\,Hz^{-1}\,sr^{-1}\,m^{-3}}$), that are both position-dependent. With these two parameters, any change in spectral intensity $\mathrm{d}I_\nu$ of the radiation due to absorption and emission along an infinitesimal propagation $\mathrm{d}x$ in the cloud can be written as the following radiative transfer equation:

$$\mathrm{d}I_\nu(x) = -\alpha_\nu(x) I_\nu \,\mathrm{d}x + \epsilon_\nu(x)\,\mathrm{d}x\,. \tag{2.59}$$

The spectral intensity I_ν emerging from the cloud at $x = L$ can be obtained by integration of Eq. (2.59) over all positions x along the path through the cloud, i.e.,

$$\int_0^L \mathrm{d}I_\nu(x) = I_\nu(L) - I_\nu(0) = \int_0^L \Big[-\alpha_\nu(x) I_\nu + \epsilon_\nu(x)\Big]\,\mathrm{d}x\,, \tag{2.60}$$

from which it follows that

$$I_\nu(L) = I_\nu(0) + \int_0^L \Big[-\alpha_\nu(x) I_\nu + \epsilon_\nu(x)\Big]\,\mathrm{d}x\,. \tag{2.61}$$

This means that the spectral intensity at $x = L$ is given by the initial spectral intensity of the background plus an integral factor taking into account the absorption of incoming radiation by molecules in the cloud as well as the

intrinsic emission of the molecules.

It is common to rewrite Eq. (2.59) in terms of the so-called source function S_ν with dimensions of spectral intensity ($\mathrm{W\,Hz^{-1}\,sr^{-1}\,m^{-2}}$) as well as the (differential) optical depth $\mathrm{d}\tau_\nu$ (dimensionless), respectively defined as

$$S_\nu(x) = \frac{\epsilon_\nu(x)}{\alpha_\nu(x)} \tag{2.62}$$

and

$$\mathrm{d}\tau_\nu(x) = \alpha_\nu(x)\,\mathrm{d}x\,. \tag{2.63}$$

Assuming a physically and chemically homogeneous medium inside the cloud, both the emissivity and the absorbance as well as the source function and differential optical depth do not longer depend on position, but are constant everywhere, i.e.,

$$S_\nu = \frac{\epsilon_\nu}{\alpha_\nu} \tag{2.64}$$

and

$$\mathrm{d}\tau_\nu = \alpha_\nu\,\mathrm{d}x\,. \tag{2.65}$$

Dividing now both sides of Eq. (2.59) by α_ν while inserting Eqs. (2.64) and (2.65) yields

$$\mathrm{d}I_\nu = -I_\nu\,\mathrm{d}\tau_\nu + S_\nu\,\mathrm{d}\tau_\nu\,. \tag{2.66}$$

The integration to derive the final spectral intensity is therefore no longer over position but over optical depth τ_ν, i.e.,

$$\int_0^{\tau_\nu^L} \mathrm{d}I_\nu, \tag{2.67}$$

where τ_ν^L is the optical depth at $x = L$, defined as

$$\tau_\nu^L = \alpha_\nu L\,, \tag{2.68}$$

while, in general, the optical depth at any depth x into the cloud is defined as

$$\tau_\nu = \alpha_\nu x\,, \tag{2.69}$$

such that the initial optical depth at $x = 0$ is zero.

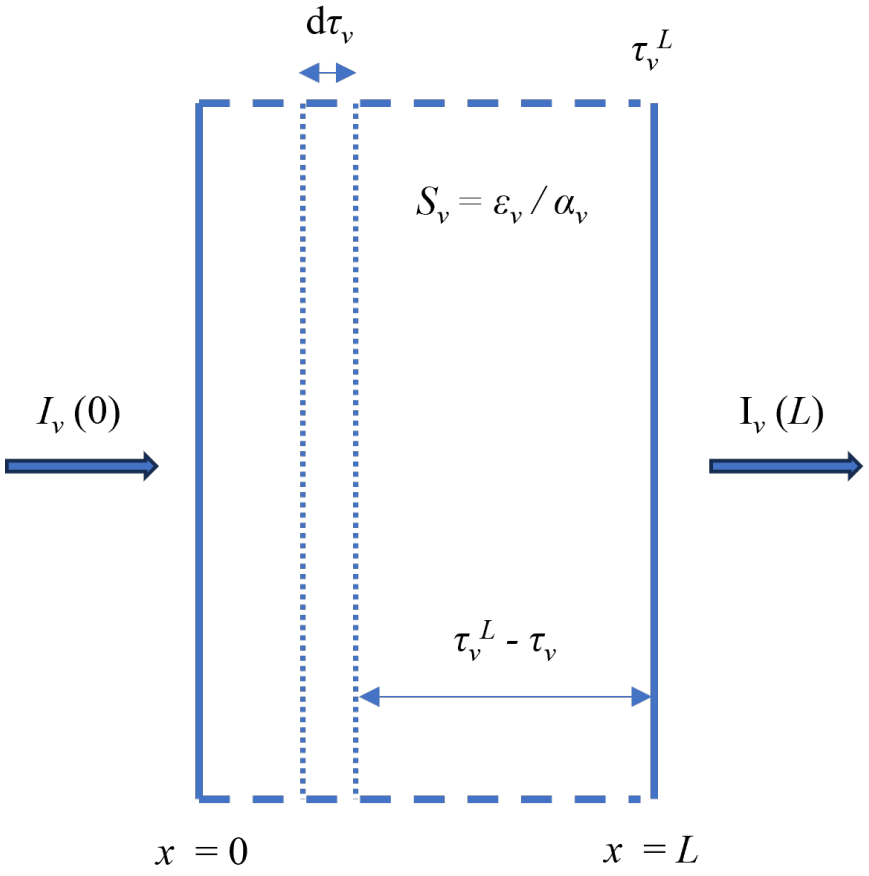

Figure 2.9: When background radiation with spectral intensity $I_\nu(0) = B_\nu(T_{\rm bg})$ enters a molecular cloud at $x = 0$, it starts to interact with molecules via absorption and stimulated emission. The source function S_ν considers the ratio of emissivity ϵ_ν and absorbance α_ν at a certain position. Based on the optical depth τ_ν of the medium, Eq. (2.74) calculates the final spectral intensity $I_\nu(L)$ coming from the cloud at $x = L$, taking into account all possible processes of emission, absorption, and re-absorption.

The integration in Eq. (2.67) is approached by first moving $I_\nu \, {\rm d}\tau_\nu$ in Eq. (2.66) to the left while multiplying by the integration factor $\exp(\tau_\nu)$, i.e.,

$$
\begin{aligned}
{\rm e}^{\tau_\nu} \Big[{\rm d}I_\nu + I_\nu \, {\rm d}\tau_\nu \Big] &= {\rm e}^{\tau_\nu} S_\nu \, {\rm d}\tau_\nu & (2.70)\\
{\rm e}^{\tau_\nu} \, {\rm d}I_\nu + {\rm e}^{\tau_\nu} I_\nu \, {\rm d}\tau_\nu &= {\rm e}^{\tau_\nu} S_\nu \, {\rm d}\tau_\nu & (2.71)\\
{\rm d}\Big[{\rm e}^{\tau_\nu} I_\nu \Big] &= {\rm e}^{\tau_\nu} S_\nu \, {\rm d}\tau_\nu & (2.72)
\end{aligned}
$$

Integrating the last equation from the starting point $\tau_\nu = 0$ at $x = 0$ with initial value I_ν^0 gives

$$\int_0^{\tau_\nu^L} \mathrm{d}\left[\mathrm{e}^{\tau_\nu} I_\nu\right] = \mathrm{e}^{\tau_\nu^L} I_\nu(L) - I_\nu(0) = \int_0^{\tau_\nu^L} \mathrm{e}^{\tau_\nu} S_\nu \, \mathrm{d}\tau_\nu \,, \tag{2.73}$$

which can be rearranged to give

$$I_\nu(L) = I_\nu(0)\, \mathrm{e}^{-\tau_\nu^L} + \int_0^{\tau_\nu^L} \mathrm{e}^{-[\tau_\nu^L - \tau_\nu]} S_\nu \, \mathrm{d}\tau_\nu \,. \tag{2.74}$$

That is, each slab $\mathrm{d}\tau_\nu$ contributes $S_\nu \, \mathrm{d}\tau_\nu \exp\left(-\left[\tau_\nu^L - \tau_\nu\right]\right)$ to the emitted radiation, where $S_\nu \mathrm{d}\tau_\nu$ corresponds to the intrinsic emission of molecules in the cloud and $\exp\left(-\left[\tau_\nu^L - \tau_\nu\right]\right)$ corresponds to the attenuation of this radiation by molecules in between the emitting slab and the edge of the cloud at $x = L$ (see Fig. 2.9) (Draine, 2011). Assuming that the source function is constant under the integration, Eq. (2.74) simplifies to

$$I_\nu(L) = I_\nu(0)\, \mathrm{e}^{-\tau_\nu^L} + S_\nu \left[1 - \mathrm{e}^{-\tau_\nu^L}\right] \tag{2.75}$$

$$= B_\nu(T_\mathrm{bg})\, \mathrm{e}^{-\tau_\nu^L} + S_\nu \left[1 - \mathrm{e}^{-\tau_\nu^L}\right] \tag{2.76}$$

where the last expression describes the case in which $I_\nu(0)$ can be approximated as the spectral intensity of a blackbody at background temperature T_bg (Eq. 1.8). The above equations are of course valid at any depth x into the cloud, and in the following, the specification "L" will therefore be removed when writing the optical depth τ_ν and spectral intensity I_ν.

2.4.3 Spectral Line Radiation

The above equations of radiative transfer are valid for both continuum radiation over a large bandwidth as well as spectral line radiation. In general, spectral lines are associated with a drastic change of emission and absorption properties over very small frequency intervals (van der Tak et al., 2007). In the following, the focus will be on spectral line radiation, and in particular, spectral line emission.

When the focus is on the description of spectral line radiation, the absorbance and the emissivity are defined as

$$\alpha_\nu = \frac{h\nu}{4\pi}(n_\mathrm{l}B_\mathrm{lu} - n_\mathrm{u}B_\mathrm{ul})\phi(\nu) \tag{2.77}$$

and

$$\epsilon_\nu = \frac{h\nu}{4\pi}n_\mathrm{u}A_\mathrm{ul}\phi(\nu)\,, \tag{2.78}$$

respectively (van der Tak et al., 2007; Yamamoto, 2017). n_u and n_l are the populations of an arbitrary pair of upper and lower energy levels at a certain position x on the path through the cloud. Furthermore, $\phi(\nu)$ is the spectral line profile, satisfying the normalization relation

$$\int \phi(\nu)\mathrm{d}\nu = 1 \tag{2.79}$$

(Yamamoto, 2017). Here, it is assumed that the line profiles for stimulated absorption, stimulated emission, and spontaneous emission are the same. In the ISM, spectral lines are predominantly affected by Doppler broadening (van der Tak et al., 2007) (see section 2.2.3), such that they can be well approximated as Gaussians. With the above definitions of absorbance and emissivity, as well as the relations between the Einstein coefficients (Eqs. 1.20 and 1.21), the source function (Eq. 2.64) becomes

$$S_\nu = \frac{\epsilon_\nu}{\alpha_\nu} = \frac{n_\mathrm{u}A_\mathrm{ul}}{n_\mathrm{l}B_\mathrm{lu} - n_\mathrm{u}B_\mathrm{ul}} = \frac{2h\nu^3}{c^2}\left[\frac{n_\mathrm{l}}{n_\mathrm{u}}\frac{g_\mathrm{u}}{g_\mathrm{l}} - 1\right]^{-1}, \tag{2.80}$$

which is independent of the spectral line profile. Assuming statistical equilibrium (SE), the energy levels are populated according to Eq. (2.34), i.e.,

$$\frac{n_\mathrm{u}}{n_\mathrm{l}} = \frac{g_u}{g_l}\exp\left(-\frac{h\nu}{k_\mathrm{B}T_\mathrm{ex}}\right).$$

For the SE case, the source function can therefore be written as

$$S_\nu = \frac{2h\nu^3}{c^2}\left[\exp\left(\frac{h\nu}{k_\mathrm{B}T_\mathrm{ex}}\right) - 1\right]^{-1}. \tag{2.81}$$

For a system in thermal equilibrium, it is furthermore true that

$$S_\nu = B_\nu(T_{\rm ex}) \tag{2.82}$$

(see Eq. 1.8), which requires that the source function respective the spectral intensity of a blackbody can be described by a constant temperature $T_{\rm ex}$ at all frequencies. However, in SE, the value of $T_{\rm ex}$ differs with frequency, i.e., from one transition (or spectral line) to another (see section 2.3.2).

Using the relations between the Einstein coefficients, it can be furthermore found that the absorption coefficient can also be expressed as

$$\alpha_\nu = \frac{c^2}{8\pi\nu^2}\frac{g_{\rm u}}{g_{\rm l}} n_{\rm l} A_{\rm ul}\left(1 - \frac{g_{\rm l}}{g_{\rm u}}\frac{n_{\rm u}}{n_{\rm l}}\right)\phi(\nu)\,, \tag{2.83}$$

and at SE, this can be written as

$$\alpha_\nu = \frac{c^2 n_{\rm u} A_{\rm ul}}{8\pi\nu^2}\left[\exp\left(\frac{h\nu}{k_{\rm B}T_{\rm ex}}\right) - 1\right]\phi(\nu)\,. \tag{2.84}$$

Based on the general definition of optical depth (Eq. 2.69), the optical depth of a spectral line in the frequency interval defined by the line profile is obtained by integration of the absorbance over the path length through the source, i.e.,

$$\begin{aligned}
\tau_\nu &= \int_0^L \alpha_\nu(x)\,{\rm d}x && (2.85)\\
&= \frac{c^2 A_{\rm ul}}{8\pi\nu^2}\left[\exp\left(\frac{h\nu}{k_{\rm B}T_{\rm ex}}\right) - 1\right]\phi(\nu)\int_0^L n_{\rm u}(x)\,{\rm d}x && (2.86)\\
&= \frac{c^2 N_{\rm u} A_{\rm ul}}{8\pi\nu^2}\left[\exp\left(\frac{h\nu}{k_{\rm B}T_{\rm ex}}\right) - 1\right]\phi(\nu)\,. && (2.87)
\end{aligned}$$

Here, $N_{\rm u}$ is introduced as the upper level column density, which will be important again in section 2.5.1. Furthermore, with the normalization relation in Eq. (2.79), integration over the line profile yields the total optical depth

associated with the spectral line, i.e.,

$$\int \tau_\nu \, \mathrm{d}\nu = \frac{c^2 N_\mathrm{u} A_\mathrm{ul}}{8\pi\nu^2} \left[\exp\left(\frac{h\nu}{k_\mathrm{B} T_\mathrm{ex}} \right) - 1 \right] . \tag{2.88}$$

2.4.4 LTE Conditions

For the case of having LTE conditions, the source function for spectral line radiation can simply be written as $S_\nu = B_\nu(T_\mathrm{ex})$ (Eq. 2.82), where it is assumed that $T_\mathrm{ex} = T_\mathrm{k} = T$. Inserting this into Eq. (2.76) gives

$$I_\nu = B_\nu(T_\mathrm{bg}) \, \mathrm{e}^{-\tau_\nu} + B_\nu(T_\mathrm{ex}) \left[1 - \mathrm{e}^{-\tau_\nu} \right] . \tag{2.89}$$

That is, at LTE conditions, the spectral intensity of a molecular cloud source at a certain frequency ν can be described solely in terms of the (H_2) kinetic temperature $T_\mathrm{k} = T_\mathrm{ex}$, the background temperature T_bg, and the cloud optical depth τ_ν.

When carrying out observations towards a molecular cloud source, and assuming that the cloud is at LTE conditions, the above definition of spectral intensity can be used to specify the expression for the radiation intensity in Eq. (2.48). Essentially, the measured on-source/on-frequency intensity I_ν^on is then given by Eq. (2.89), while the off-source/off-frequency intensity I_ν^off can simply be taken as

$$I_\nu^\mathrm{off} = B_\nu(T_\mathrm{bg}) \, . \tag{2.90}$$

Therefore, the measured intensity difference ΔI_ν between both positions is

$$\Delta I_\nu = I_\nu^\mathrm{on} - I_\nu^\mathrm{off} = \left[B_\nu(T_\mathrm{ex}) - B_\nu(T_\mathrm{bg}) \right] \left[1 - \mathrm{e}^{-\tau_\nu} \right] \tag{2.91}$$

(Mangum and Y.L. Shirley, 2015; Yamamoto, 2017). Here, it is common to introduce the Rayleigh-Jeans equivalent temperature of blackbody radiation intensity as

$$J_\nu(T) = \frac{B_\nu(T) c^2}{2 k_\mathrm{B} \nu^2} = \frac{h\nu}{k_\mathrm{B}} \left[\frac{h\nu}{k_\mathrm{B} T} - 1 \right]^{-1} , \tag{2.92}$$

where $B_\nu(T)$ is given by Planck's law (Mangum and Y.L. Shirley, 2015), i.e

Eq. (1.8). It then follows that Eq. (2.91) can be rewritten as

$$\Delta I_\nu = \frac{2k_\mathrm{B}\nu^2}{c^2}\Big[J_\nu(T_\mathrm{ex}) - J_\nu(T_\mathrm{bg})\Big]\Big[1 - \mathrm{e}^{-\tau_\nu}\Big]\,. \tag{2.93}$$

In the Rayleigh-Jeans limit, the measured radiation temperature T_R can then be defined as

$$T_\mathrm{R}(\nu) = \frac{\Delta I_\nu c^2}{2k_\mathrm{B}\nu^2} = \Big[J_\nu(T_\mathrm{ex}) - J_\nu(T_\mathrm{bg})\Big]\Big[1 - \mathrm{e}^{-\tau_\nu}\Big]\,. \tag{2.94}$$

Under the assumption of LTE conditions, and by considering the beam filling factor f (Eq. 2.50), the relation to the measured antenna temperature is

$$T_\mathrm{A}(\nu) = fT_\mathrm{R}(\nu) = f\Big[J_\nu(T_\mathrm{ex}) - J_\nu(T_\mathrm{bg})\Big]\Big[1 - \mathrm{e}^{-\tau_\nu}\Big]\,. \tag{2.95}$$

2.4.5 Non-LTE Conditions

In order to solve the radiative transfer equations for the case of an underlying SE population of energy levels, 2D or 3D numerical models for the considered physical setting must be employed. If the considered source can be assumed to be spherically symmetric, 2D models are sufficient. In the following, the focus will be on the ALI (accelerated lambda iteration) 2D radiative transfer (RT) model by P. Bergman (OSO). Towards the end of this section, different models, approaches, and approximations are briefly discussed. In astrochemical studies, RT models are commonly used to estimate line intensities of a source before an observation, or to calculate molecular column densities for the non-LTE case, as discussed in section 2.5.5.

The ALI model is a 2D model that assumes a spherically symmetric molecular cloud source with radius R, internally separated into a number of shells, and interacting with a background radiation field $B_\nu(T_\mathrm{bg})$[9]. For simplicity, it is assumed that the cloud only consists of H_2 and a target molecule "mol", and that it has kinetic temperature T_k, volume density $n(H_2)$, and abundance $X(\mathrm{mol}) = n(\mathrm{mol})/n(H_2)$. The effect of dust opacity (i.e., absorbance) κ_d can be included as well, in which case a total source function must be formulated

[9] It is also possible to consider another blackbody source at the center of the cloud, in order to model the effect of e.g., a protostar.

that takes into account the combined effects of absorbance by molecules and dust. Many of the physical conditions, like temperature, density, and abundance, can be described with constants or with gradients. The major goal of every non-LTE RT model is to obtain the energy level population of the target molecule at every position $\mathbf{r}$ in a source. According to Eqs. (2.80), (2.83), and (2.85), the level population can then be used to determine the source function $S_\nu(\mathbf{r})$, the absorbance $\alpha_\nu(\mathbf{r})$, and the optical depth $\tau_\nu(\mathbf{r})$, respectively. Eventually, these parameters are used as the input for the RT equations introduced in section 2.4.2.

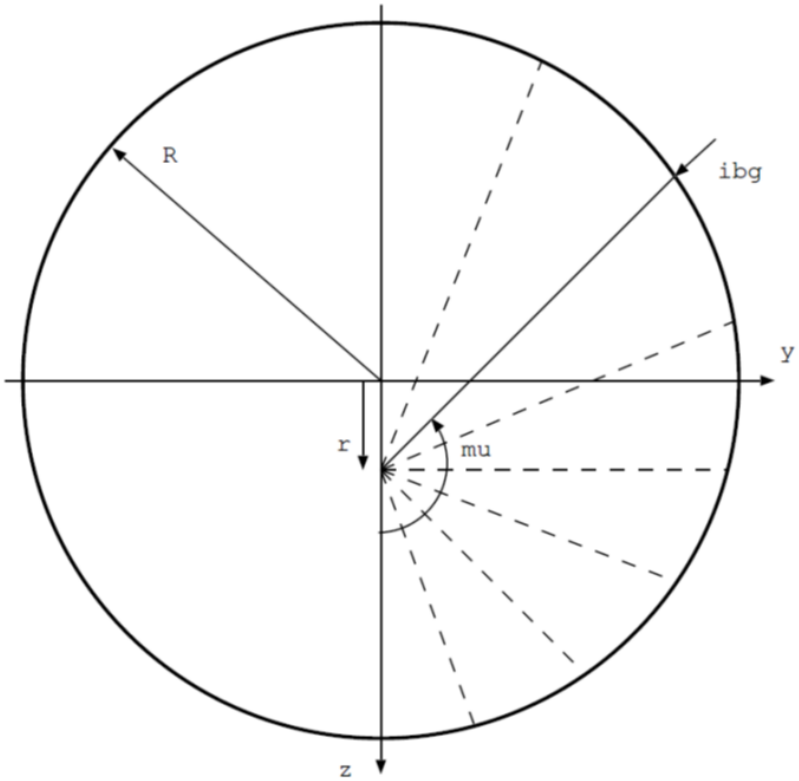

Figure 2.10: Spherically symmetric molecular cloud source (see text for explanations). Credit: P. Bergman (OSO).

With a few simple approximations, the number of positions to consider decreases significantly [P. Bergman; priv. comm.] (compare Fig. 2.10). First of all, based on the assumption that the cloud is spherically symmetric, only positions in one half of a circle, and only one position per shell must be considered

(if it is assumed that each shell is physically and chemically homogeneous). For simplicity, these positions can be taken to be points along a line through the center of the cloud (e.g., points along the z-axis), where the number of points is then given by the number of shells. The level population at every point $(0, z)$ is affected by the absorption and emission of photons, i.e., by the level populations, at other surrounding positions (y, z). To obtain the level population at exemplary point $(0, r)$, different paths at different possible angles are considered (dashed lines), through which that point receives radiation from other parts of the cloud. Along every path, is is assumed that the initial radiation intensity is the background intensity $I_\nu(0) = B_\nu(T_{\rm bg})$ ("ibg" in Fig. 2.10). When first entering the cloud, and along with particle collisions, the background radiation will produce a certain level population at a point (y, z) close to the edge, according to Eq. (2.41), written slightly adjusted as

$$\frac{\mathrm{d}}{\mathrm{d}t} n_i(y,z) = \sum_{j\neq i}^{N} n_j(y,z) P_{ji} - n_i(y,z) \sum_{j\neq i}^{N} P_{ij} = 0\,, \tag{2.96}$$

where now

$$P_{ij} = \begin{cases} A_{ij} + B_{ij} I_\nu(0) + C_{ij} & , \text{if } i > j \\ B_{ij} I_\nu(0) + C_{ij} & , \text{if } i < j\,. \end{cases} \tag{2.97}$$

The level population gives the values of $S_\nu(y, z)$, $\alpha_\nu(y, z)$, and $\tau_\nu(y, z)$, which gives a certain radiation intensity $I_\nu(y, z)$, according to Eq. (2.75), written slightly adjusted as

$$I_\nu(y,z) = I_\nu(0)\,\mathrm{e}^{-\tau_\nu(y,z)} + S_\nu(y,z)\left[1 - \mathrm{e}^{-\tau_\nu(y,z)}\right] \tag{2.98}$$

This intensity is then used as the "background intensity" $I_\nu(0)$ for the next point (y, z) along the considered path, and so forth until reaching point $(0, r)$. At that point, the average intensity $\bar{J}_\nu(0, r)$[10] considering all paths to that point, is then obtained by integration over solid angle Ω, i.e.,

$$\bar{J}_\nu(0,r) = \frac{1}{4\pi} \int I_\nu(y,z)\,\mathrm{d}\Omega\,. \tag{2.99}$$

[10] Not to be confused with the Rayleigh-Jeans equivalent temperature $J_\nu(T)$.

The final level population at that point is then obtained as

$$\frac{\mathrm{d}}{\mathrm{d}t} n_i(0,r) = \sum_{j \neq i}^{N} n_j(0,r) P_{ji} - n_i(0,r) \sum_{j \neq i}^{N} P_{ij} = 0\,, \tag{2.100}$$

with

$$P_{ij} = \begin{cases} A_{ij} + B_{ij}\bar{J}_\nu(0,r) + C_{ij} & , \text{ if } i > j \\ B_{ij}\bar{J}_\nu(0,r) + C_{ij} & , \text{ if } i < j\,. \end{cases} \tag{2.101}$$

Of course, the equations above are written for the particular point $(0,r)$, but can be written more generally for an arbitrary position $\mathbf{r}$ as

$$\frac{\mathrm{d}}{\mathrm{d}t} n_i(\mathbf{r}) = \sum_{j \neq i}^{N} n_j(\mathbf{r}) P_{ji} - n_i(\mathbf{r}) \sum_{j \neq i}^{N} P_{ij} = 0\,, \tag{2.102}$$

with

$$P_{ij} = \begin{cases} A_{ij} + B_{ij}\bar{J}_\nu(\mathbf{r}) + C_{ij} & , \text{ if } i > j \\ B_{ij}\bar{J}_\nu(\mathbf{r}) + C_{ij} & , \text{ if } i < j\,, \end{cases} \tag{2.103}$$

where

$$\bar{J}_\nu(\mathbf{r}) = \frac{1}{4\pi} \int I_\nu(\mathbf{r}')\,\mathrm{d}\Omega\,, \tag{2.104}$$

with

$$I_\nu(\mathbf{r}') = I''_\nu\,\mathrm{e}^{-\tau_\nu(\mathbf{r}')} + S_\nu(\mathbf{r}')\left[1 - \mathrm{e}^{-\tau_\nu(\mathbf{r}')}\right]. \tag{2.105}$$

In the last equation, $\mathbf{r}'$ symbolizes another position at a given distance from $\mathbf{r}$, while I''_ν symbolizes the received spectral intensity at $\mathbf{r}'$, obtained at a previous position $\mathbf{r}''$. Thereby, $\mathbf{r}$, $\mathbf{r}'$, and $\mathbf{r}''$ are lying on a line connecting the outside of the cloud with point $\mathbf{r}$.

In order to obtain a consistent statistical equilibrium (SE) throughout the cloud, the above equations must be solved iteratively, and simultaneously for all considered positions and a number of angles. This process can be separated into three major steps:

(1) Assume LTE conditions at a constant excitation temperature T_{ex}, giving the initial level populations n_i^{ini} in all shells.

(2) Solve the set of SE and RT equations (Eqs. 2.102 – 2.105) to obtain $\bar{J}_\nu$ in

every shell.

(3) Calculate new level populations n_i^{new} based on $\bar{J}_\nu$.

Then, steps (2) and (3) are repeated until convergence, i.e., until the difference between n_i^{new} and n_i^{old} is smaller than a considered boundary value[11] [P. Bergman; priv. comm.]. The accelerated lambda iteration (ALI) method is a way to speed up the underlying matrix manipulations (Rybicki and Hummer, 1991). Eventually, the consistent level populations give values for the source function S_ν and optical depth τ_ν in all shells, which can be used to model the spectral intensity coming from the cloud via the RT Eq. (2.76), i.e., by integration along lines through the cloud.

Alternative models exist for both simpler and more complex considerations. For example, in the non-LTE RT model RADEX, the direct interdependences of level populations and radiation intensities in different parts of the cloud are neglected. Instead, a global average intensity $\bar{J}_\nu$ is obtained by considering a geometrically averaged photon escape probability β, such that

$$\bar{J}_\nu = S_\nu(1-\beta)\,. \tag{2.106}$$

Essentially, β depends on the optical depth of the medium and takes different values for different approximations and geometries (van der Tak et al., 2007). An often used approximation is the so-called large velocity gradient (LVG) model, in which it is assumed that velocity gradients in the cloud are sufficiently high such that a released photon will not interact with molecules in between its point of release and the edge of the cloud. In that exemplary case,

$$\beta_{\mathrm{LVG}} = \frac{1-\mathrm{e}^{-\tau_\nu}}{\tau_\nu} \tag{2.107}$$

(de Jong et al., 1980; Gußmann, 1979; van der Tak et al., 2007), such that $\beta_{\mathrm{LVG}} \to 1$ if $\tau_\nu \ll 1$, but $\beta_{\mathrm{LVG}} \approx 1/\tau_\nu \to 0$ if $\tau_\nu \gg 1$. That is, the escape probability approaches unity for low optical depths, but assumes small values for high optical depths[12]. On the other hand, a more complex treatment is

[11] In practice, and for a smooth convergence, the current level population is often taken as $(n_i^{\mathrm{new}} + n_i^{\mathrm{old}})/2$.

[12] As will be discussed in section 2.5.3, these two cases define so-called optically thin and optically thick conditions, respectively.

provided in e.g., the non-LTE RT model LIME, which is a 3D model that can treat asymmetrical source geometries (Brinch and Hogerheijde, 2010).

2.5 Column Density Calculation

The column density of an ISM molecule is a measure of its number density per unit area along a path through the source region. Most basically, if $n(\mathrm{mol})$ is the number volume density of molecule "mol", the column density is defined as

$$N(\mathrm{mol}) = \int_0^L n(\mathrm{mol})\,\mathrm{d}x\,. \tag{2.108}$$

Knowledge about the true physical depth L of a source is often limited, which means that in such a case, only the column density of a molecule can be derived from astronomical observations. However, it is possible to calculate relative abundances for different molecules by comparing their measured column densities, and assuming their spatial distribution is the same. In the following, I will first introduce the definition of molecular column density based on the definitions of absorbance and optical depth (section 2.5.1). Afterwards, I will discuss the cases of having optically thin and optically thick spectral lines (sections 2.5.2 and 2.5.3, respectively). The population diagram method is then introduced as an alternative way to derive molecular column densities (section 2.5.4). Finally, I will discuss the calculation of column densities for non-LTE conditions (section 2.5.5).

2.5.1 Absorbance, Optical Depth, and Column Density

The basic expression for the total column density N_{tot} of a molecule can be derived from the relation between the absorbance and optical depth of a spectral line, as well as the further related (total) number of molecules in an upper energy level N_{u} (Mangum and Y.L. Shirley, 2015; Yamamoto, 2017).

The upper level column density N_{u} has been already introduced as a parameter in Eq. (2.87). It essentially gives the number of molecules in an upper energy level per unit area along a line of sight through the cloud. It can be

obtained by re-arranging Eq. (2.87), giving

$$N_{\rm u} = \frac{8\pi\nu^2}{c^2 A_{\rm ul}} \left[\exp\left(\frac{h\nu}{k_{\rm B} T_{\rm ex}} \right) - 1 \right]^{-1} \int \tau_\nu \, {\rm d}\nu \, . \tag{2.109}$$

Assuming statistical equilibrium, the upper level column density of a molecule is related to its total column density $N_{\rm tot}$ as

$$\frac{N_{\rm u}}{N_{\rm tot}} = \frac{g_{\rm u}}{Q_{\rm rot}} \exp\left(-\frac{E_{\rm u}}{k_{\rm B} T_{\rm ex}} \right) \tag{2.110}$$

(compare Eq. 2.39). Inserting Eq. (2.109) into Eq. (2.110) then gives

$$N_{\rm tot} = \frac{8\pi\nu^2}{c^2 A_{\rm ul}} \frac{Q_{\rm rot}}{g_{\rm u}} \exp\left(\frac{E_{\rm u}}{k_{\rm B} T_{\rm ex}} \right) \left[\exp\left(\frac{h\nu}{k_{\rm B} T_{\rm ex}} \right) - 1 \right]^{-1} \int \tau_\nu \, {\rm d}\nu \, . \tag{2.111}$$

In the the following sections 2.5.2, 2.5.3, and 2.5.4, it is assumed that LTE conditions are met for the molecule under consideration.

2.5.2 Optically Thin Case

As a first order approximation, it can often be assumed that the optical depth of a molecular transition is much smaller than unity. This defines the so-called optically thin approximation. Essentially, if $\tau_\nu \ll 1$, and if LTE conditions are assumed, the expression for the measured antenna temperature towards a source (Eq. 2.95) can be written as

$$T_{\rm A}(\nu) = f \left[J_\nu(T_{\rm ex}) - J_\nu(T_{\rm bg}) \right] \tau_\nu \, . \tag{2.112}$$

Inserting this into the expression for the total column density of a molecule (Eq. 2.111), yields

$$\begin{aligned} N_{\rm tot}^{\rm thin} = & \frac{8\pi\nu^2}{c^2 A_{\rm ul}} \frac{Q_{\rm rot}}{g_{\rm u}} \exp\left(\frac{E_{\rm u}}{k_{\rm B} T_{\rm ex}} \right) \left[\exp\left(\frac{h\nu}{k_{\rm B} T_{\rm ex}} \right) - 1 \right]^{-1} \\ & \frac{1}{f \left[J_\nu(T_{\rm ex}) - J_\nu(T_{\rm bg}) \right]} \int T_{\rm A}(\nu) \, {\rm d}\nu \, , \end{aligned} \tag{2.113}$$

where $\int T_{\rm A}(\nu)\,{\rm d}\nu$, i.e., the antenna temperature integrated over the emission line, is called the integrated intensity. It is allowed to remove the term including $J_\nu(T)$ from the integral, because it does not vary substantially across the frequency extent of a typical spectral line (Mangum and Y.L. Shirley, 2015). Often, $J_\nu(T_{\rm ex}) \gg J_\nu(T_{\rm bg})$, in which case $J_\nu(T_{\rm bg})$ can be neglected. However, in cold sources where $T_{\rm ex}$ is typically not much higher than $T_{\rm bg}$, $J_\nu(T_{\rm bg})$ must be considered (see e.g., discussion in paper A). Essentially, as $T_{\rm A}(\nu)$ is an average over the antenna beam (see section 2.4.1), the derived column density is also an average over the antenna beam.

2.5.3 Optically Thick Case

If a spectral line is optically thick, i.e., if $\tau_\nu \gg 1$, the total column density obtained with the optically thin approximation underestimates the true column density of a molecule. It must therefore be corrected by e.g., considering the optical depth of the line via a (first order) correction factor, i.e.,

$$C_\tau = \frac{\tau_\nu}{1 - {\rm e}^{-\tau_\nu}} = \frac{1}{\beta_{\rm LVG}}\,. \tag{2.114}$$

The total column density obtained from an optically thick line is then given as

$$N_{\rm tot} = C_\tau N_{\rm tot}^{\rm thin} \tag{2.115}$$

(Goldsmith and Langer, 1999; Mangum and Y.L. Shirley, 2015). As can be seen, the correction factor is the inverse of the photon escape probability β for the LVG model (Eq. 2.107). This basically means that optically thin and optically thick conditions directly refer to high respective low photon escape probabilities, as $\beta_{\rm LVG} \to 1$ if $\tau_\nu \ll 1$, but $\beta_{\rm LVG} \to 0$ if $\tau_\nu \gg 1$. One way to derive the optical depth of a spectral line is by using the so-called double-isotopologue method, in which the measured intensities of two isotopologues with a well established interstellar abundance ratio are required (Yamamoto, 2017). Another way is to solve Eq. (2.111) for the optical depth, starting from an estimated initial value $N_{\rm tot} = N_{\rm tot}^{\rm thin}$, and then using Eqs. (2.114) and (2.115) to iteratively update the value of $N_{\rm tot}$ until convergence [E. Wirström; priv. comm.]

2.5.4 The Population Diagram Method

Another way to derive the total column density of a molecule is by using the so-called population diagram method (Goldsmith and Langer, 1999; Yamamoto, 2017). To apply that method, the measured intensities of several spectral lines of the same molecule must be available. The basis of this method is the fact that, at LTE conditions, the (rotational) energy levels of a molecule are populated according to a Boltzmann distribution (compare section 2.3.4). As the emission rate and the resulting intensity of an emission line directly depend on the number of molecules in an upper energy level n_u, it follows that the relative intensities of a set of spectral lines are constrained by the same Boltzmann distribution. Assuming LTE conditions, the corresponding upper level column density can be derived as

$$N_\mathrm{u} = f \frac{8\pi k_\mathrm{B} \nu^2}{h c^3 A_\mathrm{ul}} \left(\frac{1 - \mathrm{e}^{-\tau_\nu}}{\tau_\nu} \right) \int T_\mathrm{A}(\nu)\, \mathrm{d}\nu \tag{2.116}$$

(Goldsmith and Langer, 1999). If the emission fills the beam (i.e., if $f = 1$), and if the considered line is optically thin (i.e., if $\tau_\nu \ll 1$), the above expression becomes

$$N_\mathrm{u}^\mathrm{thin} = \frac{8\pi k_\mathrm{B} \nu^2}{h c^3 A_\mathrm{ul}} \int T_\mathrm{A}(\nu)\, \mathrm{d}\nu \,. \tag{2.117}$$

If the line is optically thick, it has to be treated as discussed before for the case of total column density (Goldsmith and Langer, 1999).

The total column density is related to the upper state column density by Eq. (2.110), which can be rearranged to give

$$\ln\left(\frac{N_\mathrm{u}}{g_\mathrm{u}} \right) = \ln\left(\frac{N_\mathrm{tot}}{Q_\mathrm{rot}} \right) - \frac{E_\mathrm{u}}{T_\mathrm{ex}} \,. \tag{2.118}$$

This is the equation of a straight line in the $E_\mathrm{u} - \ln(N_\mathrm{u}/g_\mathrm{u})$-plane, which defines a so-called population diagram (or rotation diagram). The y-intercept of this line is $\ln(N_\mathrm{tot}/Q_\mathrm{rot})$, while the slope of the line is $-1/T_\mathrm{ex}$ (Goldsmith and Langer, 1999; Mangum and Y.L. Shirley, 2015). If integrated intensities for several lines of the same molecule are available, they can be used to derive upper state column densities, which can then be plotted in a population di-

agram (see Fig. 2.11). Thereby, it is of advantage if the corresponding upper levels have a large separation in E_u.

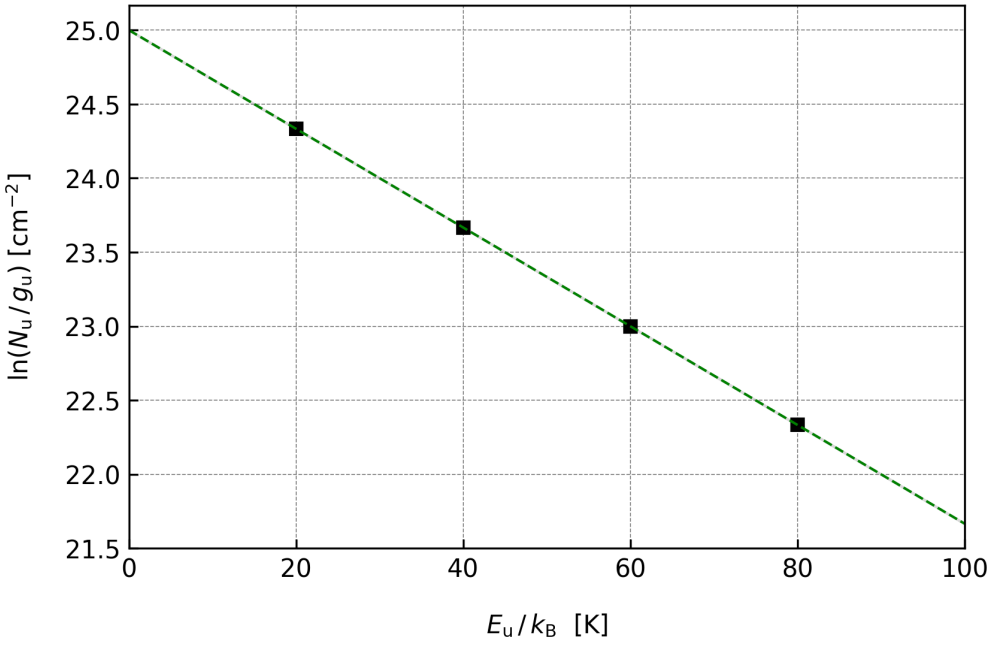

Figure 2.11: Hypothetical population diagram for perfect LTE conditions. The four data points are assumed to be calculated from Eq. (2.117) for spectral lines resulting from transitions $u \rightarrow l$ with upper level energies $E_\mathrm{u}/k_\mathrm{B}$ of 20 K, 40 K, 60 K, and 80 K. At perfect LTE conditions, the underlying population of energy levels is described by a single "equilibrium" temperature $T_\mathrm{ex} = T_\mathrm{k}$, leading to an equilibrium distribution of spectral line intensities. In that case, the excitation temperature (sometimes called rotation temperature), is perfectly constrained by the slope $-1/T_\mathrm{ex}$ of the fitted line.

At perfect LTE conditions, the data points will fall on a perfect straight line, due to the fact that the rotational energy levels are populated according to a Boltzmann distribution at the excitation temperature T_ex. In a population diagram, the value of T_ex can be derived from the slope of the line, and at perfect LTE conditions, it is equal to the H_2 gas kinetic temperature T_k in the source region. Furthermore, the total column density of the considered molecule can be derived from the y-intercept. If LTE conditions are not met for the molecule at hand, the energy level population cannot be described in terms of a Boltzmann distribution with a single excitation temperature.

Rather, each pair of energy levels is characterized by an individual excitation temperature (compare section 2.3.5). It follows that the data points in a population diagram will deviate from a straight line relation at non-LTE conditions. As follows from the discussion in that section, a set of intensities for several spectral lines of the same molecule must be measured to clearly determine if LTE conditions are met.

2.5.5 Non-LTE Conditions

If it is assumed or evident that LTE conditions are not met for a given molecule, non-LTE radiative transfer (RT) models must be employed. Just as in section 2.4.5, the focus will be on the ALI model by P. Bergman (OSO). It is a 2D model assuming a spherically symmetric source geometry. For a given set of physical and chemical parameters, i.e.,

- background spectral intensity $I_\nu(0)$,
- cloud radius R,
- H_2 gas kinetic temperature T_k,
- H_2 volume density $n(H_2)$,
- dust opacity κ_d,
- target molecule abundance $X(\mathrm{mol}) = n(\mathrm{mol})/n(H_2)$,

the model will calculate local average intensities $\bar{J}_\nu$ for spherical sub-shells, based on radiative interactions between different locations in the cloud, as well as interactions between the background radiation with molecules in the cloud. Thereby, the values of T_k, $n(H_2)$, and $X(\mathrm{mol})$ can be constant or varying with radius. The final values of $\bar{J}_\nu$ are the result of a consistent statistical equilibrium for the molecular energy level populations n_i/n_tot at all positions in the cloud. The corresponding values of fractional level populations $n_\mathrm{u}/n_\mathrm{l}$ are then used to determine values for the source function S_ν and optical depth τ_ν in all shells via Eqs. (2.80) and (2.85). Eventually, these values can be used to obtain the spectral intensity from the model cloud by integration along lines through the cloud, using the equations of radiative transfer (see section 2.4.2). Based on the modelled spectral intensity, it can be calculated what the source radiation temperature $T_\mathrm{R}(\nu)$ and corresponding antenna temperature $T_\mathrm{A}(\nu)$

would be, assuming that the source is at a certain distance from Earth and observed with a telescope in a given bandwidth and with a certain beam size (see section 2.4.1).

The obtained antenna temperature can be used to create a model spectrum for the target molecule at the considered conditions, and to calculate integrated intensities $\int T_\mathrm{A}(\nu)\,\mathrm{d}\nu$ for the modelled spectral lines. If a number of integrated intensities is measured for the source, a χ^2 analysis can be carried out to compare the measured values to the modelled values for a grid of parameters, most importantly T_k, $n(\mathrm{H_2})$, and $X(\mathrm{mol})$. The best fit parameters then give estimates for the $\mathrm{H_2}$ gas kinetic temperature and volume density of the source. Furthermore, the column density of the target molecule is directly given via Eq. (2.108) as

$$N(\mathrm{mol}) = \int_0^L n(\mathrm{mol})\,\mathrm{d}x \approx X(\mathrm{mol}) n(\mathrm{H_2}) L\,, \tag{2.119}$$

where L is the length of a line through the source. Assuming that a spherical cloud with radius R is observed with a Gaussian beam with $\theta_\mathrm{HPBW} \geq 2R$, the beam-averaged molecular column density $\langle N(\mathrm{mol})\rangle$ is approximately given as

$$\langle N(\mathrm{mol})\rangle \approx f\frac{2}{3} X(\mathrm{mol}) n(\mathrm{H_2}) 2R\,, \tag{2.120}$$

where f is the beam filling factor, defined in section 2.4.1 [P. Bergman; priv. comm.].

CHAPTER 3

Summary of Included Papers

This chapter provides a brief summary of the published paper this thesis is based on, i.e., Carl et al. (2023). The paper is attached in part II of this thesis. In the presented work, we performed a deep search for the two lowest energy conformers of glycine in the cold dark cloud Barnard 5.

3.1 Deep Search for Glycine Conformers in Barnard 5

In the following sections, I will (i) briefly summarize the motivation behind our search for interstellar glycine (3.1.1), (ii) introduce the studied source region and the observations (3.1.2), (iii) present the data analysis methods and the major results (3.1.3), and (iv) discuss some of the major results (3.1.4).

3.1.1 Background and Motivation

Our search for glycine (NH_2CH_2COOH) is generally motivated by the astrobiological hypothesis that important biotic molecules such as amino acids and nucleobases could be delivered to newly formed planets by small impacting bodies during the late stages of planet formation. It is known from observations of primitive solar system bodies (meteorites and comets) that they contain plenty of such biotic molecules, and it is assumed that some of those molecules could be partly inherited from very early phases of star formation (see also section 1). This hypothesis is investigated by astronomers since the late 1970s, when the rotational spectrum of glycine, i.e., the simplest biotic amino acid, was first assigned in the laboratory. However, despite many efforts to detect glycine in the interstellar medium, it has not yet been clearly identified.

3.1.2 Source Region and Observations

In our study, we searched for glycine in the cold dark cloud source Barnard (B)5, which is located in the Perseus molecular cloud at a distance of approximately 300 pc. B5 has a filament-like structure and contains a region of ongoing low-mass star formation in the South, including the protostar B5-IRS1 and several prestellar condensations (Fig. 3.1, left). Using the Onsala 20 m telescope, we made pointed observations towards the so-called methanol hotspot in the Northern part of B5 (Fig. 3.1, right), ending up with a total observation time of roughly 150 hours. The hotspot is a cold (< 10 K) and dense ($> 10^5$ cm^{-3}) source, characterized by very high gas phase abundances of methanol and water. It is located in between two H_2 column density peaks, called East-189 and East-286, which are however not gravitationally bound objects. As known from previous observations, the complex organic molecules

(COMs) acetaldehyde (CH_3CHO), di-methyl ether (CH_3OCH_3), and methyl formate (CH_3OCHO) are also present in the gas phase at the hotspot position. In addition to that, both the low and high energy conformers of formic acid, i.e., $t(rans)$-HCOOH and $c(is)$-HCOOH, respectively, are detected with a highly non-equilibrium abundance ratio of c/t-HCOOH $\sim 6\,\%$. This ratio might result from the fact that the hydrogenation of low energy t-HOCO* on ice surfaces (which is expected to be more abundant than its high energy form c-HOCO*) is leading to high energy c-HCOOH, and vice versa. Once desorbed into the gas phase, c-HCOOH formed by this process can drastically increase the gas phase c/t-HCOOH ratio.

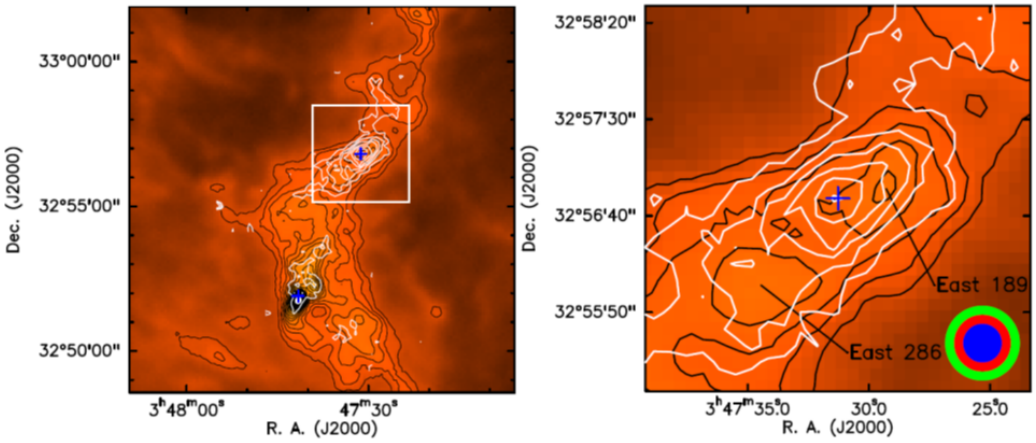

Figure 3.1: Left: Herschel/SPIRE map of the B5 dark cloud at 250 µm (orange scale and black contours) and IRAM 30 m integrated intensity map of the A^+-$CH_3OH(3_0 - 2_0)$ transition (white contours in steps of 5σ, with $\sigma = 50\,\mathrm{mK\,km\,s^{-1}}$); the blue crosses depict the positions of B5-IRS1 in the South and the methanol hotspot in the North. Credit: Taquet et al. (2017). **Right:** enlarged view on the B5 methanol hotspot (blue cross), located in between the H_2 column density peaks East-189 and East-286. The green, red, and blue circles in the bottom right corner represent the beam sizes of the OSO 20 m, IRAM 30 m, and NRO 45 m telescopes at 3 mm, respectively. Credit: Taquet et al. (2017).

We argue that the same principle can lead to an increased formation of the high energy glycine conformer NH_2CH_2COOH-II, denoted Gly-II in the following. The lower energy conformer will be denoted Gly-I. In that scenario, we assume that glycine is mostly formed on grain surfaces by reactions between radicals $NH_2CH_2{}^*$ and HOCO*, where Gly-II would then be formed from low

energy t-HOCO*. We therefore targeted a set of Gly-I and Gly-II transitions in the frequency range $\sim 70-78$ GHz, where emission from glycine is expected to be strongest at low temperatures. Our study is the first to focus on that lower frequency range. It is important to note that Gly-II not only has a higher zero-point energy compared to Gly-I, it also has a six times higher electric dipole moment, and since spectral line intensity is proportional to the square of the electric dipole moment, this results in strong Gly-II emission, making it easier to detect at low abundances.

3.1.3 Data Analysis and Results

Neither Gly-I nor Gly-II was detected in our observations towards the B5 methanol hotspot. However, we used a spectral line stacking procedure to derive sensitive upper limits for both conformers. For that, we first made spectral cut-outs around the targeted Gly-I and Gly-II lines, followed by a conversion of the intensity axis into a column density axis. We then averaged the resulting column density spectra and derived 3-σ upper limit column densities and abundances. In order to cover a range of possible excitation conditions for glycine, we calculated three sets of upper limits for excitation temperatures of 5, 7.5, and 10 K, with 7.5 K being the approximate H_2 kinetic temperature at the hotspot. Some indication of possible sub-thermal excitation comes from a rotation diagram analysis for acetaldehyde (CH_3CHO), that we performed in our study, and that gave an excitation temperature of ~ 5.7 K. Depending on the assumed excitation temperature, the ranges of upper limit abundances of Gly-I and Gly-II w.r.t. H_2 are $2-5 \times 10^{-10}$ and $0.7-3 \times 10^{-11}$, respectively. We estimate the H_2 column density at the hotspot as $\sim 1 \times 10^{22}$ cm^{-2}, based on HGBS (Herschel Gould Belt Survey) data.

3.1.4 Discussion and Conclusions

We compare the derived upper limit abundances of Gly-I and Gly-II to previously published upper limits obtained for comparable sources, and find that our Gly-II upper limits are the most stringent obtained so far, while our Gly-I upper limits are mostly on the same order than previously obtained values. We also compare our upper limits to observed gas phase abundances of other COMs at the hotspot, ranging between $\sim 2 \times 10^{-10}$ (acetaldehyde) and $\sim 2 \times 10^{-8}$ (methanol). Based on a total glycine upper limit of $2-5 \times 10^{-10}$,

we can not rule out that glycine might be present but undetected at the methanol hotspot. Jiménez-Serra et al. (2016) calculate a detection limit of $\sim 1.5 \times 10^{-11}$ for glycine in cold sources, which has not yet been reached by any study searching for glycine in a cold source.

CHAPTER 4

Work in Progress

There is no doubt that interstellar dust grains and their coupling to the gas phase play an important key role for the formation and accumulation of progressively more complex molecules in the interstellar medium. This is proven by observations of interstellar ices, experiments with interstellar ice analogues in the laboratory, and theoretical models. This chapter summarizes current projects, which I am part of, with the goal to add to the overall understanding of complex organic molecule formation in cold molecular clouds.

Section 4.1.1 first introduces some key concepts and theories related to COM formation, with a focus on theoretical models. Section 4.2 then gives an overview about the state and motivation of some running and future observational projects I am working on, focusing on gas phase COMs in the cold dark cloud Barnard 5. Finally, section 4.3 summarizes potential future work up to my PhD thesis.

4.1 COM Formation in the Cold ISM

As started being discussed in section 1.2, the detection of complex organic molecules (COMs) such as methanol (CH_3OH), acetaldehyde (CH_3CHO), di-methyl ether (CH_3OCH_3), and methyl formate (CH_3OCHO) towards cold molecular cloud sources has challenged early astrochemical models in which it was assumed that interstellar COMs are formed during the warm-up phase at the transition from the prestellar core stage to the protostellar core stage of star formation. However, state-of-the-art astrochemical models are generally able to successfully explain the formation of many COMs in low temperature environments by coupling gas phase chemistry and ice chemistry, with the latter being prevalent on and in the ice mantles around interstellar dust grains. However, important details are still not fully understood. In general, the process of reactive desorption (RD) is a promising candidate to explain the presence of gas phase COMs in environments that do not allow for efficient thermal or radiative desorption. The efficiency of this process, which depends on the considered reaction as well as on the ice surface, has to be studied in more detail in experiments, which will allow for a more accurate treatment of this process in models. Based on the concept of RD, one can furthermore separate between two different scenarios of COM formation at low temperatures. The first assumes efficient formation of COMs at the surface of ices, followed by RD, while the second assumes the formation of COM precursor molecules at the surface of ices, followed by RD and the efficient formation of COMs in the gas phase. Both scenarios are treated in astrochemical models and will be discussed in the following section 4.1.1. The focus will be on the models by Vasyunin et al. (2017), who assume efficient gas phase formation of COMs, as well as the models by Jin and Garrod (2020) and Garrod et al. (2022), who assume efficient ice surface formation of COMs. Some more details on possible gas phase and solid state formation routes for methanol, acetaldehyde, di-methyl ether, and methyl formate are discussed in sections 4.1.2 and 4.1.3. Lastly, some aspects of the discussed models and scenarios are critically discussed in section 4.1.4.

4.1.1 Gas-Grain Astrochemical Models

Over the past two decades or so, there have been drastic improvements in the performance and complexity of gas-grain astrochemical models. The models

can be separated into stochastic Monte Carlo (MC) models and more classical rate equation (RE) models. The most basic principles are the same in all types of models (as introduced in section 1.2): a gas phase particle (atom or molecule) can accrete to a grain surface to become a surface particle, which can then move across the surface by diffusion or tunneling, react with other particles at the surface, and/or desorb back into the gas phase. When running a model for a set of conditions and an initial gas phase composition, distinct ice layers (so-called monolayers) will successively build up on top of the bare grains to form ice mantles. Parts of these mantles are in turn released back into the gas phase due to different desorption mechanisms. As a result, the gas phase composition will change over time due to particle accretion onto the grains, reactions between particles in the gas and on the surface, and particle desorption back into the gas (Cuppen et al., 2017; Taquet, 2013).

In MC models, the processes of accretion, diffusion, reaction, and desorption occur in separate, traceable steps based on underlying probabilities, which drastically limits the number of simultaneously considered grains and reactions. On the other hand, this also allows to study microscopic details of the final ice mantle structure and composition, such as the exact relative positions of species in the ice, providing information about e.g., chemical layering and the porosity of the mantle (Charnley, 1998, 2001; Cuppen et al., 2009, 2017). In RE models, the mentioned processes are treated with average rate coefficients, allowing the treatment of very complex chemical networks for a large number of grains (Cuppen et al., 2017; Taquet et al., 2012; Taquet, 2013). There are also approaches to modify RE models in such a way that certain parameters are treated quasi-stochastically (Caselli et al., 1998; Cuppen et al., 2017; Garrod, 2008). In the following, the focus will be on (modified) RE models.

State-of-the-art RE models make a separation between the gas phase, the ice surface (top few monolayers), and the bulk ice (remaining, buried monolayers). 2-phase models are those in which reactions are allowed in the gas and on the ice surface, while 3-phase models further include reactions inside the bulk ice. Many theoretical and experimental studies have been conducted to better understand the influence of certain parameters on the efficiency of particle accretion, diffusion/tunneling, reaction, and desorption. This includes

parameters such as bare grain and ice surface structure (Chang et al., 2007; Cuppen and Herbst, 2005, 2007; Nyman, 2021; Taquet et al., 2012), grain size and temperature (Acharyyam et al., 2011; Gavino et al., 2021; Sipilä et al., 2020), and ice surface composition (Minissale et al., 2016a).

In astrochemical models describing cold dark cloud chemistry in the absence of any protostellar source, it is common to assume that the rates of thermal desorption and photo-desorption are very low because of low grain temperatures and low UV photon fluxes. Thermal desorption is completely negligible except for H, H_2, and He, while photo-desorption can only occur slowly via photons produced by energetic electrons. In addition, cosmic ray desorption is also limited, and is proven to be only important on large timescales for species like CO (Cuppen et al., 2017; Taquet, 2013; Vasyunin and Herbst, 2013). As discussed in the following paragraphs, state-of-the-art astrochemical models for cold dark cloud conditions are largely based on reactive desorption[1]. It can be furthermore assumed that thermal diffusion rates of species heavier than H and He are very low at low surface temperatures. In addition to thermal diffusion, it is sometimes assumed that H and H_2 can move across an ice surface by means of quantum tunneling. Reactions are commonly assumed to occur mostly via the Langmuir-Hinshelwood (LH) mechanism (reaction after diffusion/tunneling), while the Eley-Rideal (ER) mechanism (reaction upon accretion) is often neglected[2] (Cuppen et al., 2017; Taquet, 2013; Vasyunin et al., 2017). The bare grain size is often assumed as a constant, reflecting the average interstellar grain size ($\sim 0.1\,\mu m$; Sipilä et al., 2020; Taquet et al., 2012; Taquet, 2013). In the context of cold COM formation, some details of two particular RE models are discussed in the following. The basic assumptions mentioned in this paragraph are used in both models, but there are some exceptions that will be discussed. In short, both models are largely based on the concept of reactive desorption, but the treatment of this process as well as the major assumptions about the chemical pathways towards COM formation are very different. Furthermore, both models are compared to COM observations towards the prototypical prestellar core L1544, providing for a good comparability between the models. However, even though both models are

[1] It is possible that collisions between ice-covered grains might also cause significant non-thermal desorption in certain cases (see section 4.2).

[2] The ER mechanism can be important at very high accretion rates, e.g., during the phase of catastrophic CO freeze-out (Cuppen et al., 2017).

describing a very different chemistry, they are both leading to a convincing agreement with observations, making it difficult to argue for a better validity of one model over the other. In the following, the focus of discussion will be first on more general aspects of the models, while possible formation pathways for selected COMs are discussed in some detail in sections 4.1.2 and 4.1.3. In addition, some critical discussion of certain aspects of both models can be found in section 4.1.4.

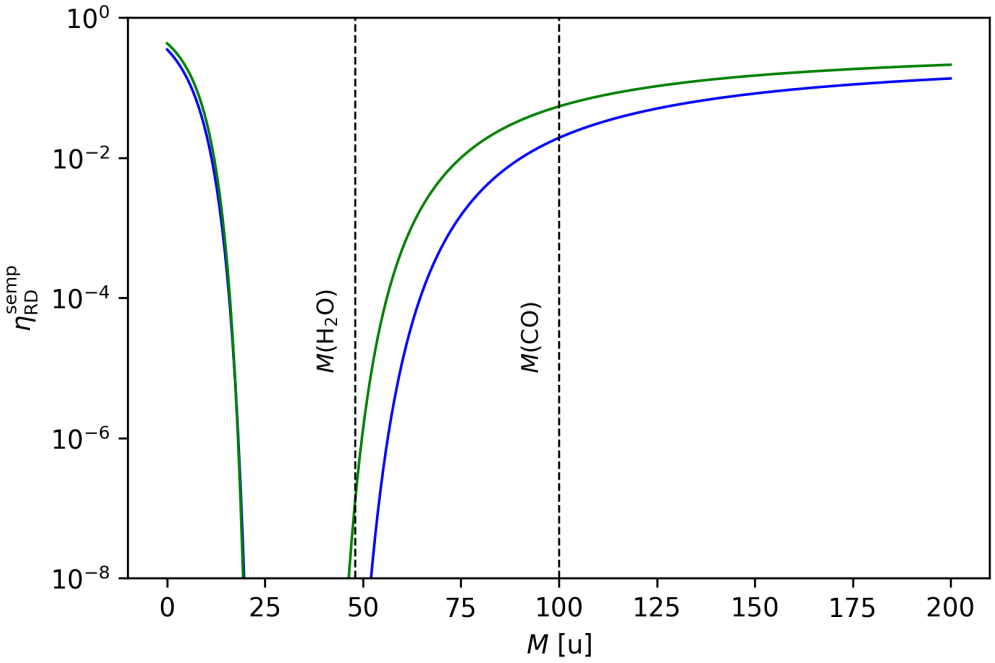

Figure 4.1: Reactive desorption efficiency $\eta_{\mathrm{RD}}^{\mathrm{semp}}$ calculated from Eq. (4.1) as a function of effective mass M for reactions $HCO^* + H \rightarrow H_2CO$ (formaldehyde; green line) and $CH_3O^* + H \rightarrow CH_3OH$ (methanol; blue line), having reaction enthalpies ΔH of 3.91 eV and 4.56 eV, respectively. The binding energies E_b of formaldehyde and methanol with water ice are used, i.e., 3200 K and 3700 K, respectively. Values of ΔH and E_b are taken from Minissale et al. (2016a). The black dashed lines indicate the effective masses of a water ice surface and a CO ice surface (values taken from Vasyunin et al., 2017).

The first model to discuss is presented in Vasyunin et al. (2017). It is a classic RE model that considers the formation of COMs via gas phase formation routes from precursor molecules, which are assumed to be released from

grain surfaces by reactive desorption (RD). The RD treatment in the model is based on experimental work by Minissale et al. (2016a), who studied the RD efficiency for different surface reactions and surface coverages. In that work, a semi-empirical ("semp") expression is derived that relates the RD efficiency $\eta_{\rm RD}^{\rm semp}$ to the enthalpy of reaction ΔH, the binding energy $E_{\rm b}$, and the internal structure of the desorbing molecules, expressed in terms of its degrees of freedom $N = 3n_{\rm atoms}$, i.e.,

$$\eta_{\rm RD}^{\rm semp} = \exp\left(-\frac{E_{\rm b}}{\epsilon \Delta H/N}\right), \tag{4.1}$$

where

$$\epsilon = \frac{(M-m)^2}{(M+m)^2} \tag{4.2}$$

is the fraction of kinetic energy retained by the reaction product with mass m colliding with a surface element with effective mass M. Fig. 4.1 shows the RD efficiency for surface reactions $HCO^* + H \rightarrow H_2CO$ (formaldehyde; green line) and $CH_3O^* + H \rightarrow CH_3OH$ (methanol; blue line) as a function of M[3]. To eventually desorb from an ice surface, a newly formed molecule has to bounce against the surface to gain velocity in the direction perpendicular to the surface. Thereby, the RD efficiency can be considered as the probability that the kinetic energy of the reaction product exceeds its binding energy to the surface. The effective mass M (in atomic mass units; u) of a surface element is typically larger than the mass of an individual surface molecule. The best fit to the experimental data for desorption of a species from a water ice surface is determined by Minissale et al. (2016a) as $M(H_2O) = 48$ u. As can be seen from Fig. 4.1, the RD efficiency for both formaldehyde and methanol from a water ice surface is predicted to be extremely low (i.e., 1.2×10^{-7} and 4.1×10^{-12}, respectively). However, as mentioned in section 1.2, and further emphasized in Vasyunin et al. (2017), the top ice layers on interstellar dust grains inside of dense molecular cloud regions are characterized by high amounts of CO, which has a larger effective mass. The value of M(CO) is yet to be determined experimentally, but Vasyunin et al. (2017) assume a value between 80 u and 120 u (based on experiments with CO-H_2CO ices by Minissale et al., 2016b), and work with $M(CO) = 100$ u. Based on that value,

[3]Here and in the following, radicals are marked with an asteriks.

the RD efficiency for desorption of formaldehyde and methanol from a CO ice surface is predicted from Fig. 4.1 as $\sim 5\,\%$ and $\sim 2\,\%$, respectively. Just as in Vasyunin et al. (2017), Fig. 4.1 is based on binding energies of formaldehyde and methanol for water ice, while the binding energy for CO ice might be lower, which would increase the RD efficiency. However, this uncertainty is not likely to exceed the uncertainty in the value of $M(\mathrm{CO})$. A general conclusion of Minissale et al. (2016a) is that RD seems to favor small molecules with low binding energies.

The model of Vasyunin et al. (2017) is a 2-phase model that is largely based on an earlier model by Vasyunin and Herbst (2013). In that earlier model, no separation was made between the ice surface and the bulk ice, and chemical reactions could occur everywhere in the ice, at any instant. The updated model by Vasyunin et al. (2017) allows only reactions at the ice surface, i.e., in the top four monolayers. For that reason, the authors had to assume efficient surface tunneling of atomic and molecular hydrogen in order to produce reasonable COM abundances. In the same work, model results are compared to observational data for the well-studied prestellar core L1544 in Taurus. The authors report very good agreement between modelled and observed abundances for acetaldehyde, di-methyl ether, and methyl formate. However, methanol is overproduced, which might be due to an overestimated RD efficiency or an overproduction of methanol on grains. Furthermore, the modelled data reproduces very well the COM peak observed at an offset position from the L1544 core center (Jiménez-Serra et al., 2016, observed offset: $\sim 0.02\,\mathrm{pc}$, modelled offset: $\sim 0.015\,\mathrm{pc}$), especially with the advanced treatment of RD, provided by the semi-empirical theory in Minissale et al. (2016a).

The second model to discuss here is presented in Jin and Garrod (2020). It is largely based on the 3-phase, modified RE model MAGICKAL (Model for Astrophysical Gas and Ice Chemical Kinetics And Layering), which itself is introduced in Garrod (2013). In contrast to the model by Vasyunin et al. (2017), the model by Jin and Garrod (2020) assumes that COMs are formed directly at the surface of dust grains before being released into the gas phase via RD. The treatment of RD in their model follows that of Garrod et al. (2007), where the RD efficiency is quantified with the Rice-Ramsperger-Kessel (RRK) theory. In that theory, the molecule-surface bond is considered as

an additional vibrational mode, and the RD efficiency is calculated via the probability P that an energy $E > E_\mathrm{b}$ is present in the bond. Assuming that the energy is provided by ΔH, P is then expressed as

$$P = \left[1 - \frac{E_\mathrm{b}}{\Delta H}\right]^{s-1} , \tag{4.3}$$

where s is the number of vibrational modes, with $s = 2$ for di-atomic species, and $s = 3n_\mathrm{atoms} - 5$ for all other non-linear molecules. If a molecule would have no other means of energy loss than through the surface-molecule bond, the RD desorption rate would be given as $\nu_\mathrm{b} P$, where ν_b is the bond frequency. However, the energy loss to the surface is assumed to be fast, and in order to obtain the RD efficiency, the competition between energy loss through the surface-molecule bond and energy loss to the surface must be considered. If ν_s is the rate at which energy is lost to the surface, the RD efficiency $\eta_\mathrm{RD}^\mathrm{RRK}$ would then be given as

$$\eta_\mathrm{RD}^\mathrm{RRK} = \frac{\nu_\mathrm{b} P}{(\nu_\mathrm{s} + \nu_\mathrm{b} P)} = \frac{aP}{1 + aP} , \tag{4.4}$$

where $a = \nu_\mathrm{b}/\nu_\mathrm{s}$. Garrod et al. (2007) use a generic value of a for all surface species, and performed model runs for different values for a. They compare model results to observations of cold cores L134N and TMC-1CP, and conclude that the use of the RD treatment according to the RRK theory generally improves the agreement between models and observations. They report an optimum value around $a = 0.03$. Minissale et al. (2016a) unsuccessfully tested the RRK treatment to fit their experimental RD data. The main issue is that this approach makes no clear separation between different surface reactions, because the value of P is typically very high, while the value of a is largely unknown and assumed to be the same for all reactions. However, Minissale et al. (2016a) find that the RD efficiency depends on both the surface reaction and the composition of the surface itself, with the latter not being considered in the RRK theory at all. The model presented in Jin and Garrod (2020) assumes a generic value of $a = 0.01$.

In contrast to Vasyunin et al. (2017), Jin and Garrod (2020) do not only include an RD treatment in their model, but also two completely new non-

diffusive surface reaction mechanisms, and it should be noted that the focus of their publication is rather on introducing these new reaction mechanisms than on highlighting the RD treatment. They assume that diffusion is solely thermal, while tunneling is completely neglected. Reactions are assumed to occur via both the LH and the ER mechanisms. It is then assumed that the product of an LH or ER reaction can further react with a possible reaction partner in the close proximity of the product, without the need of any further surface diffusion. Jin and Garrod (2020) call this mechanism the three-body (3-B) reaction mechanism. They further define another mechanism in which an LH or ER reaction product has sufficient excitation energy to overcome the activation barrier for a reaction with a nearby reaction partner. This mechanism is called the three-body excited-formation (3-BEF) mechanism. In addition to these two completely new mechanisms, they further consider a mechanism in which a newly formed photo-product may immediately react with a nearby reaction partner. This mechanism is called the photodissociation-induced (PDI) reaction mechanism, which was introduced previously in Garrod (2019). These non-diffusive mechanisms are implemented into the underlying rate equations with so-called appearance rates, considering the probability that a reaction product is in close proximity to a reaction partner. As in Vasyunin et al. (2017), Jin and Garrod (2020) compare results for different model setups to observations of gas phase COMs in L1544. In general, they find that every non-diffusive reaction mechanism, excluding ER, significantly increases the gas phase abundance of COMs, especially of di-methyl ether and methyl formate, with the latter only substantially increased via the 3-BEF mechanism. With their models, the observed COM peak at an offset of $\sim 0.02\,\mathrm{pc}$ from the core center can be reproduced, although the modelled peak offset is $\sim 0.01\,\mathrm{pc}$.

4.1.2 Formaldehyde and Methanol

Of the gas phase COMs observed in cold dark cloud sources, only the formation of methanol is rather well understood from observations, experiments, and theory: it is formed on the surface of ice-covered grains by successive hydrogenation of CO during the stage of catastrophic CO freeze-out (see also section 1.2), and then released into the gas phase by non-thermal desorption mechanism(s), like for example reactive desorption. The formation route of methanol, which has been experimentally confirmed by e.g., Fuchs et al.

(2009), can be written as

$$\mathrm{CO\,(s)} \xrightarrow{+\mathrm{H}} \mathrm{HCO^*\,(s)} \xrightarrow{+\mathrm{H}} \mathrm{H_2CO\,(s)} \xrightarrow{+\mathrm{H}} \mathrm{CH_3O^*\,(s)} \xrightarrow{+\mathrm{H}} \mathrm{CH_3OH\,(s)}\,. \quad (4.5)$$

formaldehyde is formed as a byproduct in that chain, but could be also efficiently produced in the gas phase via

$$\mathrm{CH_3{}^*\,(g) + O\,(g) \longrightarrow H_2CO\,(g) + H\,(g)}\,. \quad (4.6)$$

On the other hand, methanol has no efficient gas phase formation routes, and is solely produced on grain surfaces. However, once in the gas phase, methanol can be destroyed via e.g.,

$$\mathrm{CH_3OH\,(g) + OH^*\,(g) \longrightarrow CH_3O^*\,(g) + H_2O\,(g)} \quad (4.7)$$

(Vasyunin et al., 2017). Minissale et al. (2016b) showed that the formation of formaldehyde and methanol on grain surfaces via reaction chain (4.5) is more complex and accompanied by the "backward" H_2 abstraction reactions

$$\mathrm{HCO^*\,(s) + H\,(s) \longrightarrow CO\,(s) + H_2\,(s)} \quad (4.8)$$

and

$$\mathrm{H_2CO\,(s) + H\,(s) \longrightarrow HCO^*\,(s) + H_2\,(s)}\,, \quad (4.9)$$

effectively suppressing the formation of both formaldehyde and methanol (Vasyunin et al., 2017). These backward reactions are not included in the reaction network of Vasyunin et al. (2017), which the authors state as one possible explanation for the observed overproduction of formaldehyde and methanol. The RD efficiency of products in reaction chain (4.5) is studied in experiments by Chuang et al. (2018). Observations towards eight prestellar cores by Bacmann and Faure (2016) revealed typical gas phase abundance ratios between the species in reaction chain (4.5) of $\mathrm{HCO^*} : \mathrm{H_2CO} : \mathrm{CH_3O^*} : \mathrm{CH_3OH} \sim 10 : 100 : 1 : 100$. Vasyunin et al. (2017) report modelled abundance ratios of 5 : 480 : 1 : 270 for the prestellar core L1544, which was however not part of the sample set in Bacmann and Faure (2016). We aim to further study this characteristic set of ratios by targeting transitions of the radicals $\mathrm{HCO^*}$ and $\mathrm{CH_3O^*}$ towards the Barnard 5 methanol hotspot (see section 4.2).

4.1.3 Acetaldehyde, Di-Methyl Ether, and Methyl Formate

In contrast to methanol, the formation of larger COMs, such as acetaldehyde, di-methyl ether, and methyl formate, commonly observed towards cold molecular cloud sources, is not well understood. In the following, possible gas phase (4.1.3 a) and solid state (4.1.3 b) formation routes will be discussed for these three COMs, with the discussion largely based on the modelling work of Vasyunin et al. (2017) and Garrod et al. (2022), respectively. The latter work is based on the model by Jin and Garrod (2020), introduced in the previous section. Even though this work does not solely focus on COM formation in cold sources, and does therefore not provide a comparison of model results with observational data, it does provide a very detailed analysis of which reactions dominate at which times and conditions.

(a) Gas Phase Formation Routes

With respect to the model of Vasyunin and Herbst (2013), Vasyunin et al. (2017) altered the acetaldehyde gas phase formation by adding the following reactions to the chemical network:

$$\mathrm{CH_3OH\,(g) + CH^*\,(g)} \longrightarrow \mathrm{CH_3CHO\,(g) + H\,(g)}\,, \tag{4.10}$$

$$\mathrm{CH_3OH\,(g) + CH^*\,(g)} \longrightarrow \mathrm{CH_3{}^*\,(g) + H_2CO\,(g)}\,, \tag{4.11}$$

$$\mathrm{CH_3COH\,(g) + C\,(g)} \longrightarrow \mathrm{C_2H_4\,(g) + CO\,(g)}\,, \tag{4.12}$$

$$\mathrm{CH_3{}^*\,(g) + HCO^*\,(g)} \longrightarrow \mathrm{CH_3CHO\,(g)} + h\nu\,. \tag{4.13}$$

Based on thermodynamic arguments, a probability ratio of 10 : 1 is assigned for reaction (4.11) over reaction (4.10), and, according to the model, reaction (4.10) contributes most to the formation of acetaldehyde.

In the model of Vasyunin et al. (2017), di-methyl ether is found to be mostly produced via reaction

$$\mathrm{CH_3O^*\,(g) + CH_3{}^*\,(g)} \longrightarrow \mathrm{CH_3OCH_3\,(g)} + h\nu\,, \tag{4.14}$$

for which the rate coefficient was updated since Vasyunin and Herbst (2013). The methyl radical ($\mathrm{CH_3{}^*}$) is largely formed by dissociative recombination of

$CH_5{}^+$, assisted by the gas phase reaction

$$CH_3O^*(g) + H(g) \longrightarrow CH_3{}^*(g) + OH^*(g)\,. \tag{4.15}$$

Furthermore, it is found that about 55 % of the methoxy radical (CH_3O^*) is produced in the gas phase via reaction (4.7), while the remaining 45 % are produced by the hydrogenation of H_2CO at grain surfaces (i.e., as part of the reaction chain 4.5).

Vasyunin et al. (2017) added a chemical link between di-methyl ether and methyl formate in the gas phase, which has been proposed by Balucani et al. (2015). They find that approximately 2/3 of methyl formate is produced via

$$CH_3OCH_2{}^*(g) + O(g) \longrightarrow CH_3OCHO(g) + H(g)\,, \tag{4.16}$$

where the $CH_3OCH_2{}^*$ radical is mainly produced by destruction of di-methyl ether in the gas phase via

$$CH_3OCH_3(g) + OH^*(g) \longrightarrow CH_3OCH_2{}^*(g) + H_2O(g)\,. \tag{4.17}$$

In addition, approximately 1/3 of methyl formate is produced by reaction

$$CH_3OH_2{}^+(g) + HCOOH(g) \longrightarrow HC(OH)OCH_3{}^+(g) + H_2O(g)\,, \tag{4.18}$$

where formic acid (HCOOH) is found to be mostly formed by dissociative recombination of $HCOOH_2{}^+$, which in turn is formed via reaction

$$H_2O(g) + HCO^+(g) \longrightarrow HCOOH_2{}^+(g) + h\nu\,. \tag{4.19}$$

Vasyunin et al. (2017) find the surface formation of HCOOH to be inefficient because of the immobility of its surface reactants OH^* and HCO^*.

(b) Solid State Formation Routes

Garrod et al. (2022) performed extensive model runs to simulate the chemical evolution from the early collapse stage of star formation to the protostellar core stage. Here, the focus is on the findings for the chemical evolution from the early collapse stage to the prestellar core stage, where the temperature reaches its minimum value. To model that evolution, the gas temperature is

assumed to be constant at 10 K, while the dust temperature is assumed to decrease from 14.7 K to 8 K as a function of visual extinction, starting from an initial value of $A_V = 3$. At the same time, the total hydrogen density is assumed to increase on a free-fall timescale from 3×10^3 cm^{-3} to 2×10^8 cm^{-3}.

In the main model of Garrod et al. (2022), and at the prestellar core stage, most acetaldehyde is formed through reactions

$$CH_3{}^*(s) + HCO^*(s) \xrightarrow{\text{3-B}} CH_3CHO(s) \tag{4.20}$$

and

$$CH_2CO(s) + 2\,H(s) \xrightarrow{\text{LH}} CH_3CHO(s)\,. \tag{4.21}$$

It is furthermore found that a larger total amount of acetaldehyde is produced during the early collapse via the latter reaction, where ketene (CH_2CO) is mostly formed via

$$CH_2{}^*(s) + CO(s) \xrightarrow{\text{3-B}} CH_2CO(s)\,. \tag{4.22}$$

Garrod et al. (2022) find no substantial net formation of ketene at low temperatures due to its rapid hydrogenation, and the formation of acetaldehyde via reaction (4.21). Further acetaldehyde is produced during the early collapse by

$$H_2CO(s) + CH_2{}^*(s) \xrightarrow{77\,\%\,\text{LH},\,23\,\%\,\text{3-B}} CH_3CHO(s)\,. \tag{4.23}$$

Garrod et al. (2022) find no formation of di-methyl ether in the prestellar core stage, but significant formation during the earlier collapse stage via reaction

$$CH_2{}^*(s) + CH_3OH(s) \xrightarrow{87\,\%\,\text{LH},\,13\,\%\,\text{3-B}} CH_3OCH_3(s)\,, \tag{4.24}$$

for which it is stated that the methylene radical (CH_2^*) is sufficiently mobile to allow for efficient LH reactions. It is pointed out that Jin and Garrod (2020) had issues in producing sufficient di-methyl ether to account for the observed abundances in L1544. This might be due to the fact that much of this molecule is formed before reaching the prestellar core stage via the above reaction, which was not included in that earlier work. It is further mentioned in the text that most di-methyl ether in the gas phase results from hydro-

genation of the $CH_3OCH_2{}^*$ radical at grain surfaces, followed by RD. This is however not apparent from their Fig. (13) and the later discussion of the formation of di-methyl ether, which might be due to the fact that the plots in Fig. (13) show the total production of selected molecules in all phases (gas and ice).

In the main model of Garrod et al. (2022), and unlike acetaldehyde and di-methyl ether, no methyl formate is formed during the early collapse, but only during the prestellar core stage at the lowest temperatures. It is mainly produced by

$$CH_3O^*(s) + HCO^*(s) \xrightarrow{\text{3-B}} CH_3OCHO(s) \tag{4.25}$$

and, to a smaller extent, by

$$CH_3OCO(s) + H(s) \xrightarrow{\text{LH}} CH_3OCHO(s)\,, \tag{4.26}$$

where CH_3OCO is formed via

$$CH_3O^*(s) + CO(s) \xrightarrow{\text{3-BEF}} CH_3OCO(s)\,. \tag{4.27}$$

The findings reported in Garrod et al. (2022) regarding the most dominant surface reactions producing acetaldehyde, di-methyl ether, and methyl formate, are largely consistent with what is reported in Jin and Garrod (2020). The only exception is di-methyl ether, which was underproduced in the latter work, as mentioned above, and found to be mostly formed via

$$CH_3O^*(s) + CH_3{}^*(s) \xrightarrow{\text{3-B}} CH_3OCH_3(s)\,. \tag{4.28}$$

4.1.4 Gas Phase Formation Vs. Solid State Formation

This section is dedicated to some critical discussion of the COM formation scenarios described in the previous sections, and investigated in detail in Vasyunin et al. (2017) as well as Jin and Garrod (2020) and Garrod et al. (2022). First and foremost, the reactive desorption (RD) treatment in Jin and Garrod (2020) and Garrod et al. (2022), which is based on Garrod et al. (2007), is critically discussed in Minissale et al. (2016a), because it does not successfully separate between different surface reactions and ice surface compositions (as mentioned in section 4.1.1). In this regard, the RD treatment

in Vasyunin et al. (2017) seems superior as it is directly based on the semi-empirical theory of RD efficiency derived in Minissale et al. (2016a). The latter authors further report that RD is most efficient for small molecules with low binding energies, which might better fit a scenario in which smaller precursor molecules are released from an ice surface to form larger COMs in the gas phase.

On the other hand, the diffusion, or better, "non-diffusion" treatment in Jin and Garrod (2020) and Garrod et al. (2022) seems superior when compared to the diffusion treatment in Vasyunin et al. (2017). That is, by introducing new, non-diffusive reaction mechanisms considering chain-like reactions between reaction products and further nearby reactants, Jin and Garrod (2020) and Garrod et al. (2022) are able to produce reasonable COM gas phase abundances at cold conditions without the need to include tunneling. In that regard, Vasyunin et al. (2017) state that they had to assume efficient tunneling of H and H_2 at ice surfaces in order to produce reasonable COM abundances. However, they do not discuss how reasonable their assumption of high tunneling rates actually is based on experimental or theoretical data.

Some direct arguments against the validity of the models of Vasyunin et al. (2017) are found in Jin and Garrod (2020), where it is stated that the models of Vasyunin et al. (2017) are overproducing methanol, and would rely on high gas phase abundances of methanol to account for the gas phase abundances of larger COMs. This is however in direct conflict to what is actually stated in Vasyunin et al. (2017), where the authors argue that a very high abundance of methanol in the gas phase is not needed to reproduce observed abundances of other COMs. As already mentioned in section 4.1.1, Vasyunin et al. (2017) are discussing the overproduction of formaldehyde and methanol in their models, and argue that the RD efficiency or the surface production of these molecules might be too high – an issue that might be partly resolved with the inclusion of the observed backward reactions in the methanol reaction chain (4.5), described in Minissale et al. (2016b). Jin and Garrod (2020) further argue that the rate coefficient for the main reaction responsible for the formation of acetaldehyde in the gas phase (reaction 4.10) might be too high in Vasyunin et al. (2017), because it is extrapolated to 10 K from experimental data obtained at room temperature.

It appears an interesting approach to combine the RD treatment in Vasyunin et al. (2017), based on Minissale et al. (2016a), with the diffusion treatment in Jin and Garrod (2020) and Garrod et al. (2022). The testing of some gas phase COM formation routes is discussed in Jin and Garrod (2020). There, the authors report that including the major reactions for the formation of di-methyl ether and methyl formate in the gas phase, i.e., reactions (4.7), (4.14), and (4.16), respectively, are not efficient at the conditions considered in their model. They argue that gas phase methanol is still rather destroyed by ion-molecule reactions than via reaction (4.7), while the contribution to the CH_3O^* production from hydrogenation of H_2CO on grain surfaces is not discussed. Furthermore, Jin and Garrod (2020) only include

$$CH_3OH\,(g) + C(^3P)\,(g) \longrightarrow {CH_3}^*(g) + HCO^*(g) \tag{4.29}$$

in order to explain the formation of ${CH_3}^*$, which is one reaction route proposed in Shannon et al. (2013, 2014). However, Vasyunin et al. (2017) find that ${CH_3}^*$ is mostly produced by dissociative recombination of ${CH_5}^+$ and via reaction (4.15). As a result, Jin and Garrod (2020) report no significant production of di-methyl ether in the gas phase. Based on that, neither methyl formate is efficiently formed in the gas phase because it is directly linked to di-methyl ether through reaction 4.16. Here, Jin and Garrod (2020) only include

$$CH_3OCH_3\,(g) + Cl\,(g) \longrightarrow CH_3O{CH_2}^*(g) + HCl\,(g)\,, \tag{4.30}$$

to account for the $CH_3O{CH_2}^*$ production, following Balucani et al. (2015), but again, this is not what is found in Vasyunin et al. (2017), who report that $CH_3O{CH_2}^*$ is mainly formed via the destruction of di-methyl ether by OH^*, i.e., reaction (4.17), because chlorine is highly depleted in the gas phase at all times. In summary, Jin and Garrod (2020) do not clearly discuss or include the gas phase reactions found to be most dominant in Vasyunin et al. (2017), but only refer to reactions proposed and used in Vasyunin and Herbst (2013), Shannon et al. (2013, 2014), and Balucani et al. (2015).

A set of gas phase reactions well reflecting the one used in Vasyunin et al. (2017) is used in the main model of Garrod et al. (2022), although the authors do not discuss details of the included reaction routes to produce CH_3O^*

and $CH_3{}^*$. However, they discuss the formation routes for $CH_3OCH_2{}^*$, and state that they do not consider the formation of that radical via destruction of di-methyl ether by chlorine (and florine), but, among a few other reactions, its formation via destruction by OH^*. According to Tabs. (1) and (10) in Garrod et al. (2022), only including these gas phase reactions, without changing any other model assumptions, seems to have no significant effect on the overall modelled COM abundances in the gas phase. In that regard, the authors state that the gas phase reaction between CH_3O^* and $CH_3{}^*$ to form di-methyl ether (reaction 4.14) never exceeds 1 % of its total production (from the early collapse to the prestellar core stage). A similar trend is observed for the production of methyl formate from reactions between atomic oxygen and $CH_3OCH_2{}^*$ (reaction 4.16). One final conclusions of the authors is still that gas phase reactions appear to contribute moderately to COM production, although they do not dominate.

4.2 Distribution of COMs in Barnard 5

In a current project, we aim to set constraints on the COM formation scenarios discussed in the previous sections (i.e., COM formation in the gas phase vs. COM formation in the solid state). For that, we made pointed single-dish observations with the IRAM 30 m telescope towards two positions close to the B5 methanol hotspot, which was already introduced in section 3.1.2. As a recap, the region around the hotspot is not related to any ongoing star formation, although it is located in between two density peaks, which are however not related to gravitationally bound cores. Furthermore, the hotspot itself is characterized by an H_2 gas kinetic temperature of $\sim 7.5\,\mathrm{K}$ and an H_2 density of $\sim 2.3 \times 10^5\,\mathrm{cm}^{-3}$ (Taquet et al., 2017). That is, even though the hotspot is no prestellar core, morphologically, it is still characterized by comparable gas temperatures and densities. However, the dust temperature of $\sim 13\,\mathrm{K}$ (Carl et al., 2023) might be considered slightly higher compared to common (low-mass) prestellar core conditions.

At the hotspot, the gas phase abundance of methanol relative to H_2 ($\sim 2 \times 10^{-8}$; Carl et al., 2023; Taquet et al., 2017) is about an order of magnitude higher than what is observed towards other cold molecular cloud sources ($\sim 10^{-9}$; Punanova et al., 2022; Scibelli and Y. Shirley, 2020). In addition,

it is also higher compared to others positions in B5, hence the designation "hotspot" (Wirström et al., 2014). Furthermore, the gas phase abundance of water ($\sim 8\times10^{-9}$; Carl et al., 2023; Wirström et al., 2014), which is rarely targeted towards cold molecular cloud sources, is almost two magnitudes higher than what is observed towards the prestellar core L1544 ($\sim 1\times10^{-10}$; Caselli et al., 2012). Another position where gas phase abundances of methanol and water are high is observed further South in the B5 filament, close to the protostar B5-IRS1. However, the abundances of both molecules are lower compared to the abundances at the hotspot. While the presence of gas phase methanol and water close to B5-IRS1 could be explained by enhanced thermal desorption and photo-desorption, this does not apply for the hotspot position. Instead, very efficient non-thermal desorption mechanisms must be at work at that position (Taquet et al., 2017; Wirström et al., 2014).

As discussed in sections 1.2 and 4.1.2, there is little to no doubt that the formation of methanol in molecular clouds is largely dominated by surface reactions on ice-covered dust grains (e.g., Chuang et al., 2018; Garrod et al., 2022; Taquet et al., 2017; Vasyunin et al., 2017). The peak production of methanol starts when the accretion of CO onto grains becomes very high (at densities $> 10^5$ cm^{-3}), allowing for the efficient hydrogenation of CO, and the formation of methanol via reaction chain (4.5), in short: CO $\longrightarrow$ H_2CO $\longrightarrow$ CH_3OH. Therefore, if methanol is observed in the gas phase, this means that this is almost entirely the result of desorption from grain surfaces. Observations by Scibelli and Y. Shirley (2020) and Punanova et al. (2022) demonstrate that gas phase methanol is omnipresent in prestellar and starless core environments of the Taurus molecular cloud complex down to visual extinctions of $A_V = 3$, where CO ice starts to form. Thereby, as supported by theoretical models and experiments, reactive desorption (RD) is the most promising candidate to explain the widespread distribution of gas phase methanol in cold molecular clouds (e.g., Chuang et al., 2018; Garrod et al., 2022; Jin and Garrod, 2020; Minissale et al., 2016a; Vasyunin et al., 2017), especially in denser regions where cosmic ray (CR) desorption is inefficient. However, considering the methanol gas phase distribution along the whole B5 filament (see Fig. 1 in Wirström et al., 2014), it is hard to explain the strongly localized methanol peak at the hotspot position with conventionally considered non-thermal desorption mechanisms such as CR desorption and RD (Taquet et al., 2017;

Wirström et al., 2014). The high density at the hotspot ($> 10^5\,\mathrm{cm}^{-3}$) should not allow for an overly efficient CR desorption, while RD could only account for the very high methanol gas phase abundance if the production of methanol on grains has a localized maximum at the hotspot (at least if the underlying RD efficiency is assumed to be constant). However, a very high production rate of methanol would require a very high diffusion rate of hydrogen (assuming that hydrogen atoms are overabundant on grains), but considering the low dust temperature at the hotspot position ($\sim 13\,\mathrm{K}$), there is no reason to assume such a high diffusion rate. In addition, an elevated accretion rate of CO might also be considered as a reason for an elevated methanol formation rate. However, if it is assumed that CO is over-abundant on dust grains during and/or following the catastrophic CO freeze-out, the actual CO accretion rate should have no further impact on the methanol formation rate. On the other hand, if CO is not over-abundant, but transformed into methanol very efficiently, the production rate of methanol would be directly affected by the CO accretion rate. However, since the accretion rate is mostly a function of density, it is not expected to be significantly higher at the methanol peak than e.g., at the surrounding H_2 column density peaks.

As discussed in section 1.2, observations, experiments, and models show that the ice mantles around interstellar dust grains are layered structures. At densities $> 10^5\,\mathrm{cm}^{-3}$, when the freeze-out of CO onto grains becomes very high, the ice mantles are structured into (i) H_2O-rich inner layers, (ii) CO-rich intermediate layers, and (iii) CH_3OH-rich outer layers (e.g., Boogert et al., 2015; Chuang et al., 2022; Cuppen et al., 2009). The fact that not only methanol but also water is very abundant at the B5 hotspot position suggests that deeper ice layers are efficiently released into the gas phase as well[4]. However, as pointed out in Wirström et al. (2014), the gas phase ratio of methanol to water (~ 2.5) suggests that the desorption mechanism at the hotspot, though very efficient, is not causing complete mantle disruption (as the total ice composition is always dominated by water; e.g., Boogert et al., 2008, 2015). As further mentioned in Wirström et al. (2014), one possible

[4]Based on that, one could further assume that a lot of CO ice is also released back into the gas phase, which would suggest that the CO depletion factor at the hotspot might be lower than what could be expected at the prevalent density. Our recent observations with the Onsala 20 m telescope also include CO lines, such that this hypothesis can be tested.

option to explain the high localized gas phase abundances of methanol and water at the hotspot is that ice mantle material is released into the gas phase by grain-grain collisions, which might occur at an elevated rate due to a cloud-cloud collision at the larger scale. This desorption mechanism is not commonly considered in astrochemical models, but an attempt is made in Kalvāns and Silsbee (2022).

We argue that, regardless of the process that is actually causing the efficient desorption of ice species at the hotspot, other COMs and/or precursor molecules would be likewise affected as methanol and water. This makes the hotspot an excellent testbed for possible COM formation scenarios, if the gas phase abundances of methanol and other COMs are compared to abundances at offset positions from the hotspot, where the desorption is evidently less efficient. Based on that, we further argue that, if COMs are predominantly formed on grain surfaces, one should find COM abundances peaking alongside with methanol at the hotspot.

As mentioned in the beginning of this section, we observed two positions close to the hotspot with the IRAM 30 m telescope. The first position is close to the edge of the B5 filament, while the other position is the density peak East 189, located North-East of the hotspot (see Fig. 4.2). The two positions will be called B5-Edge and B5-East. We chose these positions to cover a range of H_2 densities, which are expected to increase from B5-Edge to the hotspot to B5-East. As summarized in Tab. 4.1, we targeted several transitions of acetaldehyde (CH_3CHO), di-methyl ether (CH_3OCH_3), and methyl formate (CH_3OCHO) in the frequency range $\sim$ 83.5 – 100.5 GHz. As mentioned in section 3.1.2, these three COMs are all detected at the hotspot by Taquet et al. (2017). We further targeted the $5_{-1} - 4_0$ transition of E-CH_3OH at $\sim$ 84.5 GHz. However, this transition turned out to be a weak maser line, so we observed another set of methanol transitions with the Onsala 20 m telescope in the range $\sim$ 95.9 – 108.9 GHz.

A first analysis of the data shows that acetaldehyde is detected towards B5-Edge and B5-East, while methyl formate and di-methyl ether are only detected at B5-East. Methyl formate is tentatively detected at B5-Edge as well, and we will try to confirm this detection by decreasing the noise level in our spectra

with additional observations towards that position (the observation proposal for the IRAM 30 m telescope is accepted). Column densities are calculated for the detected molecules (except methanol) for both positions, assuming LTE conditions and optically thin emission (see section 2.5.2). Using data from the Herschel Gould Belt Survey (HGBS[5]; André et al., 2010; Roy et al., 2014), H_2 column densities are derived for B5-Edge and B5-East as $\sim 0.8 \times 10^{22}\,\mathrm{cm}^{-2}$ and $\sim 1 \times 10^{22}\,\mathrm{cm}^{-2}$, respectively. The resulting gas phase abundances with respect to H_2 are shown in Fig. 4.3.

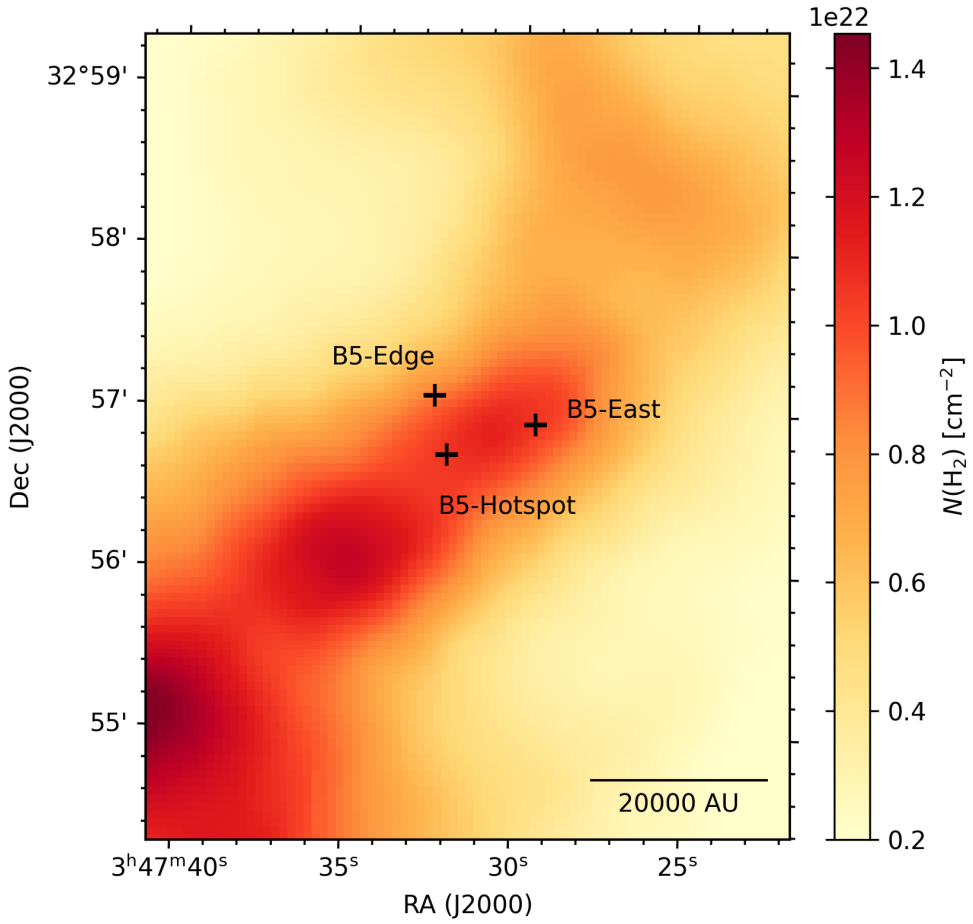

Figure 4.2: H_2 column density map for the region around the B5 methanol hotspot, created from HGBS data.

[5] http://www.herschel.fr/cea/gouldbelt/en/Phocea/Vie_des_labos/Ast/ast_visu.php?id_ast=66

Table 4.1: Targeted transitions of methanol (CH_3OH), acetaldehyde (CH_3CHO), di-methyl ether (CH_3OCH_3), and methyl formate (CH_3OCHO).

Molecule	Transition	ν [GHz]	Telescope
E-CH_3OH	$5_{-1} - 4_0$	84.52117	IRAM 30 m
A^+-CH_3OH	$2_1 - 1_1$	95.91431	OSO 20 m
E-CH_3OH	$2_{-1} - 1_{-1}$	96.73936	OSO 20 m
A^+-CH_3OH	$2_0 - 1_0$	96.74137	OSO 20 m
E-CH_3OH	$2_0 - 1_0$	96.74455	OSO 20 m
E-CH_3OH	$2_1 - 1_1$	96.75550	OSO 20 m
A^--CH_3OH	$2_1 - 1_1$	97.58280	OSO 20 m
E-CH_3OH	$0_0 - 1_{-1}$	108.89395	OSO 20 m
E-CH_3CHO	$2_{1,2} - 1_{0,1}$	83.58428	IRAM 30 m
A-CH_3CHO	$2_{1,2} - 1_{0,1}$	84.21975	IRAM 30 m
E-CH_3CHO	$5_{1,5} - 4_{1,3}$	98.86331	IRAM 30 m
A-CH_3CHO	$5_{1,5} - 4_{1,3}$	98.90094	IRAM 30 m
EE-CH_3OCH_3	$4_{1,4} - 3_{0,3}$	99.32525	IRAM 30 m
AA-CH_3OCH_3	$4_{1,4} - 3_{0,3}$	99.32607	IRAM 30 m
E-CH_3OCHO	$7_{2,6} - 6_{2,5}$	84.44917	IRAM 30 m
A-CH_3OCHO	$7_{2,6} - 6_{2,5}$	84.45475	IRAM 30 m
E-CH_3OCHO	$7_{3,4} - 6_{3,3}$	87.14328	IRAM 30 m
A-CH_3OCHO	$7_{3,4} - 6_{3,3}$	87.16129	IRAM 30 m
E-CH_3OCHO	$9_{1,9} - 8_{1,8}$	100.07861	IRAM 30 m
A-CH_3OCHO	$9_{1,9} - 8_{1,8}$	100.08054	IRAM 30 m
E-CH_3OCHO	$8_{1,7} - 7_{1,6}$	100.48224	IRAM 30 m
A-CH_3OCHO	$8_{1,7} - 7_{1,6}$	100.49068	IRAM 30 m
E-CH_3OCHO	$8_{2,6} - 7_{2,5}$	103.46657	IRAM 30 m
A-CH_3OCHO	$8_{2,6} - 7_{2,5}$	103.47866	IRAM 30 m

In accordance with Taquet et al. (2017), we find that LTE conditions are not met for methanol, so we plan to use the non-LTE radiative transfer model ALI to derive its column density (see section 2.5.5). This modeling effort has started but we do not yet have reliable results to include in the analysis. Eventually, the non-LTE modelling of methanol will also set constraints on the H_2 gas kinetic temperature and density at both positions, which will further help with the interpretation of the data, as well as with potential astrochemical modelling in the future. As mentioned in a footnote above, CO is also observed towards all three positions (B5-Hotspot, B5-Edge, and B5-East), and we plan to derive estimates for the CO depletion factor, which potentially provides further information about the ice desorption efficiency[6].

Even though (i) the methanol analysis is not finished yet, and (ii) we are expecting additional data for B5-Edge, what we found so far is that COM abundances are not peaking together with methanol at the hotspot. Instead, the abundances of COMs tend to peak at B5-East (see Fig. 4.3; most prominent for acetaldehyde and di-methyl ether), where the methanol abundance is presumably lower than at the hotspot, while the density is presumably higher. This is hard to explain when assuming that methanol and COMs are simultaneously formed on the surface of ice mantles, and released into the gas phase by the same desorption process. It could be however explained when it is instead assumed that COMs are formed in the gas phase with rates that depend on density and temperature. One could still question why expected peak abundances of COM precursor gas phase molecules at the hotspot would not lead to a COM peak at that position, given that the net production of a species directly depends on the abundances of its reactants. However, this could be explained based on the presumably lower density at the hotspot compared to B5-East (and the resulting lower two-body reactive collision rates), which could render the depletion of precursor molecules in the gas phase less efficient at the hotspot. In that sense, an underproduction of COMs at the methanol hotspot could be a time-effect, and therefore, due to a young "chemical" age of the source. In a future project, we aim to observe the radicals HCO^* and CH_3O^* towards the hotspot position (the observation proposal for the IRAM 30 m telescope is accepted). HCO^* is detected in the gas phase towards B5-

[6]Further information about the desorption efficiency could be obtained by studying the gas-to-ice ratio of species like H_2O, CO, and CH_3OH towards the hotspot position using e.g., the JWST.

Edge and B5-East, and from unpublished data for the hotspot, we know that it is also present at that position with roughly half the line intensity compared to B5-East. The CH_3O^* radical is detected towards a number of cold cores (Bacmann and Faure, 2016), and a detection or non-detection of that radical in the gas phase will further help to interpret the COM data for the region around the B5 methanol hotspot.

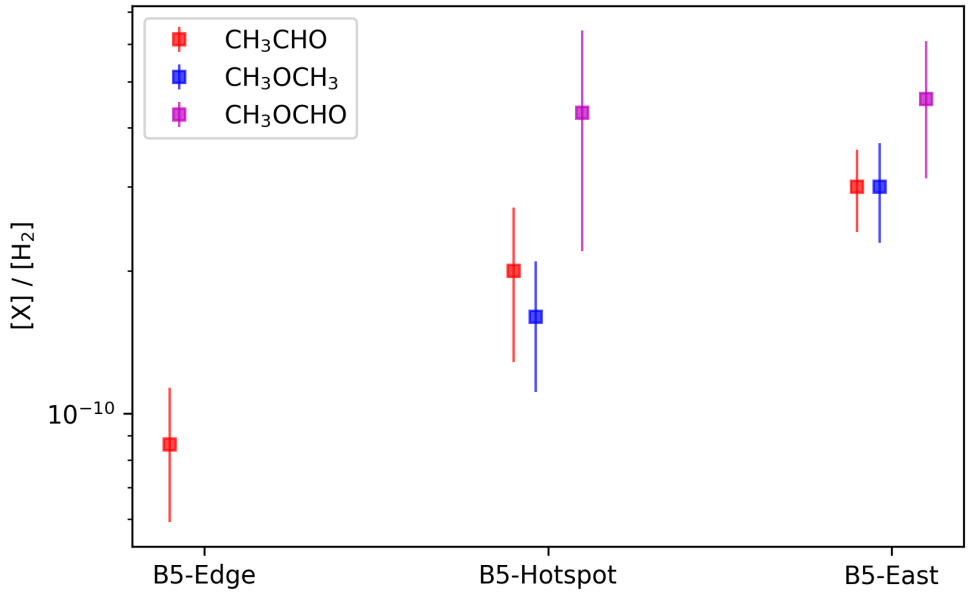

Figure 4.3: Gas phase abundances (relative to H_2) of acetaldehyde (CH_3CHO), di-methyl ether (CH_3OCH_3), and methyl formate (CH_3OCHO) towards B5-Edge, B5-Hotspot, and B5-East. A 15 % uncertainty is assumed for the H_2 column density, which is derived from HGBS data. For B5-Hotspot, column density data for CH_3OCH_3 and CH_3OCHO is taken from Taquet et al. (2017), and for CH_3CHO from Carl et al. (2023).

4.3 Future Work

In the previous section, a current observation project with the focus to study the distribution of COMs in the region around the B5 methanol hotspot was introduced. We aim to use these observations in order to set constraints on state-of-the-art COM formation models and scenarios for cold molecular cloud

sources. A key step in the data analysis process will be the non-LTE modelling of the methanol emission for all three positions, i.e., B5-Edge, B5-Hotspot, and B5-East.

Additional granted observation time with the IRAM 30 m telescope will enable us to (i) lower the noise level in our spectra for the position B5-Edge, to potentially confirm the detection of methyl formate at that position, and (ii) to target transitions of the radicals HCO^* and CH_3O^* towards the hotspot position, which will help with the interpretation of the COM data for the hotspot region.

Infrared observations towards a background source behind the hotspot could be used to derive gas-to-ice ratios of e.g., H_2O, CO, and CH_3OH. This would be of great value to better understand the nature and efficiency of the desorption process at that position.

Finally, we plan to use some astrochemical modelling for the case of the B5 hotspot region in order to (i) test some hypotheses about the desorption process and its efficiency in that area, and (ii) to test major COM formation scenarios for cold molecular cloud environments by comparison of model data to observational data for the B5 region, including gas phase abundances of methanol and larger COMs, water, CO, and some key radicals.

References

Acharyyam, K. et al. (2011). "The Effects of Grain Size and Grain Growth on The Chemical Evolution of Cold Dense Clouds". In: *The Astrophysical Journal* 732, p. 73. DOI: 10.1088/0004-637X/732/2/73.

Altwegg, K. et al. (2016). "Prebiotic chemicals—amino acid and phosphorus—in the coma of comet 67P/Churyumov-Gerasimenko". In: *Science Advances* 2, e1600285. DOI: 10.1126/sciadv.1600285.

André, P. et al. (2010). "From filamentary clouds to prestellar cores to the stellar IMF: Initial highlights from the Herschel Gould Belt Survey". In: *Astronomy and Astrophysics* 518, p. L102. DOI: 10.1051/0004-6361/201014666.

– (2014). "From Filamentary Networks to Dense Cores in Molecular Clouds: Toward a New Paradigm for Star Formation". In: *Protostars and Planets VI*. Ed. by H. Beuther et al., pp. 27–51. DOI: 10.2458/azu_uapress_9780816531240-ch002.

Atkins, P. et al. (2018). *Physical Chemistry - Quantum Chemistry, Spectroscopy, and Statistical Thermodynamics*. Oxford University Press.

Bacmann, A. et al. (2012). "Detection of complex organic molecules in a prestellar core: a new challenge for astrochemical models". In: *Astronomy and Astrophysics* 541, p. L12. DOI: 10.1051/0004-6361/201219207.

Bacmann, A. and Faure, A. (2016). "The origin of gas-phase HCO and CH_3O radicals in prestellar cores". In: *Astronomy and Astrophysics* 587, A130. DOI: 10.1051/0004-6361/201526198.

Balucani, N. et al. (2015). "Formation of complex organic molecules in cold objects: the role of gas-phase reactions." In: *Monthly Notices of the Royal Astronomical Society* 449, pp. L16–L20. DOI: 10.1093/mnrasl/slv009.

Bennett, J. et al. (2010). *Astronomie - Die kosmische Perspektive*. Pearson Studium.

Boogert, A.C.A. et al. (2008). "The c2d Spitzer Spectroscopic Survey of Ices around Low-Mass Young Stellar Objects. I. H_2O and the 5-8 μm Bands". In: *The Astrophysical Journal* 678, pp. 985–1004. DOI: 10.1086/533425.

– (2015). "Observations of the icy universe." In: *Annual Review of Astronomy and Astrophysics* 53, pp. 541–581. DOI: 10.1146/annurev-astro-082214-122348.

Borquez, E. et al. (2005). "An Investigation of Prebiotic Purine Synthesis from the Hydrolysis of HCN Polymers". In: *Origins of Life and Evolution of the Biosphere* 35, pp. 79–90. DOI: 10.1007/s11084-005-5945-9.

Botta, O. and Bada, J.L. (2002). "Extraterrestrial Organic Compounds in Meteorites". In: *Surveys in Geophysics* 23, pp. 411–467. DOI: 10.1023/A:1020139302770.

Breuer, D. and Moore, W.B. (2015). "Dynamics and Thermal History of the Terrestrial Planets, the Moon, and Io". In: *Treatise on Geophysics (Second Edition)*. Ed. by G. Schubert. Vol. 10: Physics of Terrestrial Planets and Moons. Elsevier Ltd., pp. 255–305.

Brinch, C. and Hogerheijde, M.R. (2010). "LIME - a flexible, non-LTE line excitation and radiation transfer method for millimeter and far-infrared wavelengths". In: *Astronomy and Astrophysics* 523, A25. DOI: 10.1051/0004-6361/201015333.

Callahan, M.P. et al. (2011). "Carbonaceous meteorites contain a wide range of extraterrestrial nucleobases". In: *Proceedings of the National Academy of Science* 108, pp. 13995–13998. DOI: 10.1073/pnas.1106493108.

Carl, T. et al. (2023). "Deep search for glycine conformers in Barnard 5". In: *Monthly Notices of the Royal Astronomical Society* 524, pp. 5993–6003. DOI: 10.1093/mnras/stad2017.

Caselli, P. et al. (1998). "A Proposed Modification of the Rate Equations for Reactions on Grain Surfaces". In: *The Astrophysical Journal* 495, pp. 309–316. DOI: 10.1086/305253.

– (2012). "First Detection of Water Vapor in a Pre-stellar Core". In: *The Astrophysical Journal Letters* 759, p. L37. DOI: 10.1088/2041-8205/759/2/L37.

Caselli, P. and Ceccarelli, C. (2012). *Our astrochemical heritage*. URL: doi.org/10.48550/arXiv.1210.6368.

Chang, Q. et al. (2007). "Gas-grain chemistry in cold interstellar cloud cores with a microscopic Monte Carlo approach to surface chemistry". In: *Astronomy and Astrophysics* 469, pp. 973–983. DOI: 10.1051/0004-6361:20077423.

Chapovsky, P.L. and Hermans, L.J.F. (1999). "Nuclear Spin Conversion in Polyatomic Molecules". In: *Annual Review of Physical Chemistry* 50, pp. 315–345. DOI: 10.1146/annurev.physchem.50.1.315.

Charnley, S.B. (1998). "Stochastic Astrochemical Kinetics". In: *The Astrophysical Journal Letters* 509, pp. L121–L124. DOI: 10.1086/311764.

– (2001). "Stochastic Theory of Molecule Formation on Dust". In: *The Atrophysical Journal Letters* 562, pp. L99–L102. DOI: 10.1086/324753.

Chuang, K.-J. et al. (2018). "Reactive Desorption of CO Hydrogenation Products under Cold Pre-stellar Core Conditions". In: *The Astrophysical Journal* 853, p. 102. DOI: 10.3847/1538-4357/aaa24e.

– (2022). "Formation of the Simplest Amide in Molecular Clouds: Formamide (NH_2CHO) and Its Derivatives in H_2O-rich and CO-rich Interstellar Ice Analogs upon VUV Irradiation". In: *The Astrophysical Journal* 933, p. 107. DOI: 10.3847/1538-4357/ac7320.

Cleaves, H.J. et al. (2008). "A Reassessment of Prebiotic Organic Synthesis in Neutral Planetary Atmospheres". In: *Origins of Life and Evolution of the Biosphere* 38, pp. 105–115. DOI: 10.1007/s11084-007-9120-3.

College Sidekick (2024). *Cosmic Dust*. Retrieval Date: 2024, Jan 13. URL: https://www.collegesidekick.com/study-guides/astronomy/cosmic-dust.

Condon, J.J. and Ransom, S.M. (2016). *Essential Radio Astronomy*. Princeton University Press.

Cooper, G. and Rios, A.C. (2016). "Enantiomer excesses of rare and common sugar derivatives in carbonaceous meteorites". In: *Proceedings of the National Academy of Science* 113, E3322–E3331. DOI: 10.1073/pnas.1603030113.

Cuppen, H.M. et al. (2009). "Microscopic simulation of methanol and formaldehyde ice formation in cold dense cores". In: *Astronomy and Astrophysics* 508, pp. 275–287. DOI: 10.1051/0004-6361/200913119.

– (2017). "Grain Surface Models and Data for Astrochemistry". In: *Space Science Reviews* 212, pp. 1–58. DOI: 10.1007/s11214-016-0319-3.

Cuppen, H.M. and Herbst, E. (2005). "Monte Carlo simulations of H_2 formation on grains of varying surface roughness". In: *Monthly Notices of the Royal Astronomical Society* 361, pp. 565–576. DOI: 10.1111/j.1365-2966.2005.09189.x.

– (2007). "Simulation of the Formation and Morphology of Ice Mantles on Interstellar Grains". In: *The Astrophysical Journal* 668, pp. 294–309. DOI: 10.1086/521014.

Dagdigian, P.J. (2019). "Excitation of Astrophysical Molecules". In: *Gas-Phase Chemistry in Space*. IOP Publishing, 7-1 to 7–29. DOI: 10.1088/2514-3433/aae1b5ch7.

de Jong, T. et al. (1980). "Hydrostatic models of molecular clouds." In: *Astronomy and Astrophysics* 91, pp. 68–84.

Draine, B.T. (2011). *Physics of the Interstellar and Intergalactic Medium*. Princeton University Press.

Drążkowska, J. et al. (2023). "Planet Formation Theory in the Era of ALMA and Kepler: from Pebbles to Exoplanets". In: *Protostars and Planets VII*. Ed. by S. Inutsuka et al. Vol. 534, p. 717. DOI: 10.48550/arXiv.2203.09759.

Ehrenfreund, P. and Charnley, S.B. (2000). "Organic Molecules in the Interstellar Medium, Comets, and Meteorites: A Voyage from Dark Clouds to the Early Earth". In: *Annual Review of Astronomy and Astrophysics* 38, pp. 427–483. DOI: 10.1146/annurev.astro.38.1.427.

Elsila, J.E. et al. (2009). "Cometary glycine detected in samples returned by Stardust". In: *Meteoritics and Planetary Science* 44, pp. 1323–1330. DOI: 10.1111/j.1945-5100.2009.tb01224.x.

ESA (2023). *ALMA/Hubble Composite Image of the Region Around the Young Star HL Tauri*. Retrieval Date: 2023, Dec 18. URL: https://www.eso.org/public/unitedkingdom/images/eso1436b/?lang.

Faure, A. (2019). "Molecular collisional excitation: theory, experiment and observations". In: *SF2A-2019: Proceedings of the Annual meeting of the French Society of Astronomy and Astrophysics*. Ed. by P. Di Matteo et al.

Ferus, M. et al. (2017). "Formation of nucleobases in a Miller-Urey reducing atmosphere". In: *Proceedings of the National Academy of Science* 114, pp. 4306–4311. DOI: 10.1073/pnas.1700010114.

Friberg, P. et al. (1988). "Methanol in dark clouds." In: *Astronomy and Astrophysics* 195, pp. 281–289.

Fuchs, G.W. et al. (2009). "Hydrogenation reactions in interstellar CO ice analogues. A combined experimental/theoretical approach". In: *Astronomy and Astrophysics* 505, pp. 629–639. DOI: 10.1051/0004-6361/200810784.

Furukawa, Y. et al. (2019). "Extraterrestrial ribose and other sugars in primitive meteorites". In: *Proceedings of the National Academy of Science* 116, pp. 24440–24445. DOI: 10.1073/pnas.1907169116.

Garrod, R.T. et al. (2007). "Non-thermal desorption from interstellar dust grains via exothermic surface reactions". In: *Astronomy and Astrophysics* 467, pp. 1103–1115. DOI: 10.1051/0004-6361:20066704.

Garrod, R.T. (2008). "A new modified-rate approach for gas-grain chemical simulations". In: *Astronomy and Astrophysics* 491, pp. 239–251. DOI: 10.1051/0004-6361:200810518.

– (2013). "A Three-phase Chemical Model of Hot Cores: The Formation of Glycine". In: *The Astrophysical Journal* 765, p. 60. DOI: 10.1088/0004-637X/765/1/60.

– (2019). "Simulations of Ice Chemistry in Cometary Nuclei". In: *The Astrophysical Journal* 884, p. 69. DOI: 10.3847/1538-4357/ab418e.

Garrod, R.T. et al. (2022). "Formation of Complex Organic Molecules in Hot Molecular Cores through Nondiffusive Grain-surface and Ice-mantle Chemistry". In: *The Astrophysical Journal Supplement Series* 259, p. 1. DOI: 10.3847/1538-4365/ac3131.

Gavino, S. et al. (2021). "Impact of size-dependent grain temperature on gas-grain chemistry in protoplanetary disks: The case of low-mass star disks". In: *Astronomy and Astrophysics* 654, A65. DOI: 10.1051/0004-6361/202038788.

Goldsmith, P.F. and Langer, W.D. (1999). "Population Diagram Analysis of Molecular Line Emission". In: *Astrophysical Journal* 517, pp. 209–225. DOI: 10.1086/307195.

Gordy, W. and Cook, R.L. (1984). *Microwave Molecular Spectra*. Wiley.

Griffiths, D.J. (1995). *Introduction to Quantum Mechanics*. Prentice Hall.

Gußmann, E. A. (1979). "D. MIHALAS: Stellar Atmospheres. Second Edition. W. H.FREEMAN & Co., San Francisco 1978. XX + 632 p., Price US $ 27.50". In: *Astronomische Nachrichten* 300, pp. 221–222. DOI: https://doi.org/10.1002/asna.19793000416.

Hadraoui, K. et al. (2019). "Distributed glycine in comet 67P/Churyumov-Gerasimenko". In: *Astronomy and Astrophysics* 630, A32. DOI: 10.1051/0004-6361/201935018.

Haken, H. and Wolf, H.C. (2006). *Molekülphysik und Quantenchemie*. Springer.

Hirota, E. (2011). *High-Resolution Spectroscopy of Transient Molecules*. Springer.

Hollas, J.M (1998). *High Resolution Spectroscopy*. Wiley.

– (2004). *Modern Spectroscopy*. Wiley.

Hoyle, F. and Wickramasinghe, N.C. (1977). "Prebiotic molecules and interstellar grain clumps". In: *Nature* 266, pp. 241–242. DOI: 10.1038/266241b0.

Hsieh, T.-H. et al. (2023). "PRODIGE - envelope to disk with NOEMA. II. Small-scale temperature structure and streamer feeding the SVS13A protobinary based on CH_3CN and DCN". In: *Astronomy and Astrophysics* 669, A137. DOI: 10.1051/0004-6361/202244183.

Hu, C.-H. et al. (1993). "Glycine Conformational Analysis". In: *Journal of the American Chemical Society* 115, pp. 2923–2929.

Hussmann, H. (2015). "Interiors and Evolution of Icy Satellites". In: *Treatise on Geophysics (Second Edition)*. Ed. by G. Schubert. Vol. 10: Physics of Terrestrial Planets and Moons. Elsevier Ltd., pp. 605–635.

Ioppolo, S. et al. (2021). "A non-energetic mechanism for glycine formation in the interstellar medium". In: *Nature Astronomy* 5, pp. 197–205. DOI: 10.1038/s41550-020-01249-0.

Jewell, P.R. (2002). "Millimeter Wave Calibration Techniques". In: *Single-Dish Radio Astronomy: Techniques and Applications*. Ed. by Snezana Stanimirovic et al. Vol. 278. Astronomical Society of the Pacific Conference Series, pp. 313–328.

Jiménez-Serra, I. et al. (2016). "The Spatial Distribution of Complex Organic Molecules in the L1544 Pre-stellar Core". In: *The Astrophysical Journal Letters* 830, p. L6. DOI: 10.3847/2041-8205/830/1/L6.

– (2020). "Toward the RNA-World in the Interstellar Medium—Detection of Urea and Search of 2-Amino-oxazole and Simple Sugars". In: *Astrobiology* 20. DOI: 10.1089/ast.2019.2125.

Jin, M. and Garrod, R.T. (2020). "Formation of Complex Organic Molecules in Cold Interstellar Environments through Nondiffusive Grain-surface and Ice-mantle Chemistry". In: *The Astrophysical Journal Supplement Series* 249, p. 26. DOI: 10.3847/1538-4365/ab9ec8.

Johansen, A. et al. (2021). "A pebble accretion model for the formation of the terrestrial planets in the Solar System". In: *Science Advances* 7, eabc0444. DOI: 10.1126/sciadv.abc0444.

Johnson, A.P. et al. (2008). "The Miller Volcanic Spark Discharge Experiment". In: *Science* 322, p. 404. DOI: 10.1126/science.1161527.

– (2009). "The Diversity of the Original Prebiotic Soup: Re-analyzing the Original Miller-Urey Spark Discharge Experiments". In: *Origins of Life and Evolution of the Biosphere* 30, pp. 240–241. DOI: 10.1007/s11084-009-9164-7.

Kalvāns, J. and Silsbee, K. (2022). "Icy molecule desorption in interstellar grain collisions". In: *Monthly Notices of the Royal Astronomical Society* 515, pp. 785–794. DOI: 10.1093/mnras/stac1792.

Koga, T. and Naraoka, H. (2017). "A new family of extraterrestrial amino acids in the Murchison meteorite". In: *Scientific Reports* 7, p. 636. DOI: 10.1038/s41598-017-00693-9.

Kvenvolden, K. et al. (1970). "Evidence for Extraterrestrial Amino-acids and Hydrocarbons in the Murchison Meteorite". In: *Nature* 228, pp. 923–926. DOI: 10.1038/228923a0.

Lambrechts, M. and Johansen, A. (2012). "Rapid growth of gas-giant cores by pebble accretion". In: *Astronomy and Astrophysics* 544, A32. DOI: 10.1051/0004-6361/201219127.

Lazcano, A. and Bada, J.L. (2003). "The 1953 Stanley L. Miller Experiment: Fifty Years of Prebiotic Organic Chemistry". In: *Origins of Life and Evolution of the Biosphere* 33, pp. 235–242. DOI: 10.1023/A:1024807125069.

Lee, C.-W. et al. (2009). "Formation of Glycine on Ultraviolet-Irradiated Interstellar Ice-Analog Films and Implications for Interstellar Amino Acids". In: *The Astrophysical Journal* 697, pp. 428–435. DOI: 10.1088/0004-637X/697/1/428.

Leiden University (2023). *LAMDA – Leiden Atomic and Molecular Database*. Retrieval Date: 2023, Dec 18. URL: https://home.strw.leidenuniv.nl/~moldata/.

Lique, F. et al. (2020). "Hyperfine excitation of SH^+ by H". In: *Astronomy and Astrophysics* 638, A72. DOI: 10.1051/0004-6361/202038041.

Lissauer, J.J. and de Pater, I. (2013). *Fundamental Planetary Science - Physics, Chemistry, and Habitability*. Cambridge University Press.

London South Bank University (2009). *Ortho-Water and Para-Water*. Retrieval Date: 2023, Oct 23. URL: https://water.lsbu.ac.uk/water/ortho_para_water.html.

Mangum, J.G. and Shirley, Y.L. (2015). "How to Calculate Molecular Column Density". In: *The Astronomical Society of the Pacific* 127, pp. 266–298. DOI: 10.1086/680323.

Marcelino, N. et al. (2007). "Discovery of Interstellar Propylene (CH_2CHCH_3): Missing Links in Interstellar Gas-Phase Chemistry". In: *The Astrophysical Journal Letters* 665, pp. L127–L130. DOI: 10.1086/521398.

Matthews, H.E. et al. (1985). "The detection of acetaldehyde in cold dust clouds." In: *The Astrophysical Journal* 290, pp. 609–614. DOI: 10.1086/163018.

Max-Planck-Gesellschaft (2023). *Voracious Stellar Embryos: Protostars Feed From Beyond Their Envelopes*. Retrieval Date: 2023, Dec 18. URL: https://www.mpg.de/20948720/protostars-feed-from-beyond-their-envelopes.

McClure, M.K. et al. (2023). "An Ice Age JWST inventory of dense molecular cloud ices". In: *Nature Astronomy* 7, pp. 431–443. DOI: 10.1038/s41550-022-01875-w.

Merino, N. et al. (2019). "Living at the Extremes: Extremophiles and the Limits of Life in a Planetary Context". In: *Frontiers in Microbiology* 10. DOI: 10.3389/fmicb.2019.00780.

Miller, S.L. (1953). "A Production of Amino Acids under Possible Primitive Earth Conditions". In: *Science* 117.3046, pp. 528–529. DOI: 10.1126/science.117.3046.528.

Minissale, M. et al. (2016a). "Dust as interstellar catalyst. I. Quantifying the chemical desorption process". In: *Astronomy and Astrophysics* 585, A24. DOI: 10.1051/0004-6361/201525981.

– (2016b). "Hydrogenation of CO-bearing species on grains: unexpected chemical desorption of CO". In: *Monthly Notices of the Royal Astronomical Society* 458, pp. 2953–2961. DOI: 10.1093/mnras/stw373.

Müller, H.S.P. et al. (2001). "The Cologne Database for Molecular Spectroscopy, CDMS". In: *Astronomy and Astrophysics* 370, pp. L49–L52. DOI: 10.1051/0004-6361:20010367.

– (2005). "The Cologne Database for Molecular Spectroscopy, CDMS: a useful tool for astronomers and spectroscopists". In: *Journal of Molecular Structure* 742, pp. 215–227. DOI: 10.1016/j.molstruc.2005.01.027.

NASA (2023a). *Europa: Facts*. Retrieval Date: 2023, Dec 16. URL: https://science.nasa.gov/jupiter/moons/europa/facts/.

– (2023b). *Exoplanet Exploration: Planets Beyond our Solar System*. Retrieval Date: 2023, Dec 16. URL: https://exoplanets.nasa.gov/.

– (2023c). *Jupiter Facts*. Retrieval Date: 2023, Dec 16. URL: https://science.nasa.gov/jupiter/facts/.

– (2023d). *Life in the Solar System? Meet the Neighbors*. Retrieval Date: 2023, Dec 16. URL: https://exoplanets.nasa.gov/news/1665/life-in-our-solar-system-meet-the-neighbors/.

– (2023e). *Titan: Facts*. Retrieval Date: 2023, Dec 16. URL: https://science.nasa.gov/saturn/moons/titan/facts/.

Natur'Eau Quant (2014). *Séparation eau "ortho" et eau "para"*. Retrieval Date: 2024, Jan 20. URL: https://marchenry.org/2014/03/19/separation-orthopara/.

Norwegian University of Science and Technology (2023). *Semi-Classical Radiation Theory*. Retrieval Date: 2023, Oct 13. URL: https://web.phys.ntnu.no/~stovneng/TFY4215_2019/lecturenotes/lecturenotes16.pdf.

Nuevo, M. et al. (2018). "Deoxyribose and deoxysugar derivatives from photoprocessed astrophysical ice analogues and comparison to meteorites". In: *Nature Communications* 9, p. 5276. DOI: 10.1038/s41467-018-07693-x.

Nyman, G. (2021). "Tunneling of Hydrogen and Deuterium Atoms on Interstellar Ices (I_h and ASW)". In: *Frontiers in Astronomy and Space Sciences* 8. DOI: 10.3389/fspas.2021.738264.

Oba, Y. et al. (2022). "Identifying the wide diversity of extraterrestrial purine and pyrimidine nucleobases in carbonaceous meteorites". In: *Nature Communications* 13, p. 2008. DOI: 10.1038/s41467-022-29612-x.

Palme, H. et al. (2014). "Solar System Abundances of the Elements". In: *Treatise on Geochemistry (Second Edition)*. Ed. by H.D. Holland and K.K. Turekian. Vol. 2: Planets, Asteriods, Comets and The Solar System. Elsevier Ltd., pp. 15–36.

Pearce, B.K.D. et al. (2017). "Origin of the RNA world: The fate of nucleobases in warm little ponds". In: *Proceedings of the National Academy of Science* 114, pp. 11327–11332. DOI: 10.1073/pnas.1710339114.

Pearce, B.K.D. and Pudritz, R.E. (2015). "Seeding the Pregenetic Earth: Meteoritic Abundances of Nucleobases and Potential Reaction Pathways". In: *The Astrophysical Journal* 807, p. 85. DOI: 10.1088/0004-637X/807/1/85.

Pineda, J.E. et al. (2020). "A protostellar system fed by a streamer of 10,500 au length". In: *Nature Astronomy* 4, pp. 1158–1163. DOI: 10.1038/s41550-020-1150-z.

Pross, A. (2016). *What is Life? How Chemistry Becomes Biology*. Oxford University Press.

Punanova, A. et al. (2022). "Methanol Mapping in Cold Cores: Testing Model Predictions". In: *The Astrophysical Journal* 927, p. 213. DOI: 10.3847/1538-4357/ac4e7d.

Rivilla, V.M. et al. (2016). "The First Detection of the Key Prebiotic Molecule PO in Star-Forming Regions". In: *The Astrophysical Journal* 826. DOI: 10.3847/0004-637X/826/2/161.

– (2020a). "ALMA and ROSINA detections of phosphorus-bearing molecules: the interstellar thread between star-forming regions and comets". In: *Monthly Notices of the Royal Astronomical Society* 492. DOI: 10.1093/mnras/stz3336.

– (2020b). "Prebiotic Precursors of the Primordial RNA World in Space: Detection of NH_2OH". In: *The Astrophysical Journal Letters* 899. DOI: 10.3847/2041-8213/abac55.

Roy, A. et al. (2014). "Reconstructing the density and temperature structure of prestellar cores from Herschel data: A case study for B68 and L1689B". In: *Astronomy and Astrophysics* 562, A138. DOI: 10.1051/0004-6361/201322236.

Royal Society of Biology (2023). *Eating Gamma Radiation for Breakfast*. Retrieval Date: 2023, Dec 16. URL: https://www.rsb.org.uk/biologist-features/eating-gamma-radiation-for-breakfast.

Rybicki, G.B. and Hummer, D.G. (1991). "An accelerated lambda iteration method for multilevel radiative transfer." In: *Astronomy and Astrophysics* 245, pp. 171–181.

Schöier, F.L. et al. (2005). "An atomic and molecular database for analysis of submillimetre line observations". In: *Astronomy and Astrophysics* 432. DOI: 10.1051/0004-6361:20041729.

Scibelli, S. and Shirley, Y. (2020). "Prevalence of Complex Organic Molecules in Starless and Prestellar Cores within the Taurus Molecular Cloud". In: *The Astrophysical Journal* 891, p. 73. DOI: 10.3847/1538-4357/ab7375.

Science News (2019). *Life Originated in Hydrothermal Vents, New Study Suggests*. Retrieval Date: 2024, Jan 9. URL: https://www.sci.news/biology/life-hydrothermal-vents-07772.html.

Shannon, R.J. et al. (2013). "Accelerated chemistry in the reaction between the hydroxyl radical and methanol at interstellar temperatures facilitated by tunnelling". In: *Nature Chemistry* 5, pp. 745–749. DOI: 10.1038/nchem.1692.

– (2014). "The fast C(3P) + CH3OH reaction as an efficient loss process for gas-phase interstellar methanol". In: *RSC Advances* 4, pp. 26342–26353. DOI: 10.1039/C4RA03036B.

Sipilä, O. et al. (2020). "Effect of grain size distribution and size-dependent grain heating on molecular abundances in starless and pre-stellar cores". In: *Astronomy and Astrophysics* 640, A94. DOI: 10.1051/0004-6361/202038353.

Taquet, V. et al. (2012). "Multilayer modeling of porous grain surface chemistry. I. The GRAINOBLE model". In: *Astronomy and Astrophysics* 538, A42. DOI: 10.1051/0004-6361/201117802.

Taquet, V. (2013). *Grain surface chemistry in star-forming regions*. URL: https://theses.hal.science/tel-00790641v1/document.

Taquet, V. et al. (2017). "Chemical complexity induced by efficient ice evaporation in the Barnard 5 molecular cloud". In: *Astronomy and Astrophysics* 607, A20. DOI: 10.1051/0004-6361/201630023.

Tennyson, J. and Faure, A. (2019). "Electron Collision Processes". In: *Gas-Phase Chemistry in Space*. IOP Publishing, 5-1 to 5–26. DOI: 10.1088/2514-3433/aae1b5ch5.

Tielens, A.G.G.M. et al. (1991). "Interstellar Solid CO: Polar and Nonpolar Interstellar Ices". In: *The Astrophysical Journal* 381, p. 181. DOI: 10.1086/170640.

Universität zu Köln (2024). *Molecules in Space*. Retrieval Date: 2024, Jan 10. URL: https://cdms.astro.uni-koeln.de/classic/molecules.

University of California San Diego (2023). *Blackbody Radiation*. Retrieval Date: 2023, Aug 7. URL: https://quantummechanics.ucsd.edu/ph130a/130_notes/node48.html.

University of California, Berkeley (1997). *Semiclassical Theory of Radiation*. Retrieval Date: 2023, Oct 23. URL: https://bohr.physics.berkeley.edu/classes/221/9697/sclthrad.pdf.

University of Puerto Rico at Arecibo (2023). *The Habitable Exoplanet Catalog*. Retrieval Date: 2023, Dec 16. URL: https://phl.upr.edu/projects/habitable-exoplanets-catalog.

University of St Andrews (2023). *Width of Spectral Lines*. Retrieval Date: 2023, Oct 25. URL: http://www-star.st-and.ac.uk/~kw25/teaching/nebulae/lecture08_linewidths.pdf.

Valdivia-Mena, M.T. et al. (2022). "PRODIGE - envelope to disk with NOEMA. I. A 3000 au streamer feeding a Class I protostar". In: *Astronomy and Astrophysics* 667, A12. DOI: 10.1051/0004-6361/202243310.

– (2023). "Flow of gas detected from beyond the filaments to protostellar scales in Barnard 5". In: *Astronomy and Astrophysics* 677, A92. DOI: 10.1051/0004-6361/202346357.

van der Tak, F.F.S. et al. (2007). "A computer program for fast non-LTE analysis of interstellar line spectra. With diagnostic plots to interpret observed line intensity ratios". In: *Astronomy and Astrophysics* 468, pp. 627–635. DOI: 10.1051/0004-6361:20066820.

van Dishoeck, E.F. et al. (2013). "Interstellar Water Chemistry: From Laboratory to Observations". In: *Chemical Reviews* 113, pp. 9043–9085. DOI: 10.1021/cr4003177.

Vastel, C. et al. (2014). "The Origin of Complex Organic Molecules in Prestellar Cores". In: *The Astrophysical Journal Letters* 795, p. L2. DOI: 10.1088/2041-8205/795/1/L2.

Vasyunin, A.I. et al. (2017). "Formation of Complex Molecules in Prestellar Cores: A Multilayer Approach". In: *The Astrophysical Journal* 842, p. 33. DOI: 10.3847/1538-4357/aa72ec.

Vasyunin, A.I. and Herbst, E. (2013). "Reactive desorption and radiative association as possible drivers of complex molecule formation in the cold interstellar medium". In: *The Astrophysical Journal* 769, p. 34. DOI: 10.1088/0004-637X/769/1/34.

Weiss, M.C. et al. (2016). "The physiology and habitat of the last universal common ancestor". In: *Nature Microbiology* 1. DOI: 10.1038/NMICROBIOL.2016.116.

Wilson, T.L. (2013). *Tools of Radioastronomy*. Springer.

Wirström, E.S. et al. (2014). "Cold Water Vapor in the Barnard 5 Molecular Cloud". In: *The Astrophysical Journal Letters* 788, p. L32. DOI: 10.1088/2041-8205/788/2/L32.

Yamamoto, S. (2017). *Introduction to Astrochemistry: Chemical Evolution from Interstellar Clouds to Star and Planet Formation*. Springer.

Yen, H.-W. et al. (2019). "HL Tau Disk in HCO^+ (3-2) and (1-0) with ALMA: Gas Density, Temperature, Gap, and One-arm Spiral". In: *The Astrophysical Journal* 880, p. 69. DOI: 10.3847/1538-4357/ab29f8.

Zeng, S. et al. (2021). "Probing the Chemical Complexity of Amines in the ISM: Detection of Vinylamine ($C_2H_3NH_2$) and Tentative Detection of Ethylamine ($C_2H_5NH_2$)". In: *The Astrophysical Journal Letters* 920. DOI: 10.3847/2041-8213/ac2c7e.

Part II

Papers

PAPER A

Deep search for glycine conformers in Barnard 5

Tadeus Carl, Eva S. Wirström, Per Bergman, Steven B. Charnley, Yo-Ling Chuang, Yi-Jehng Kuan

Published in: *Monthly Notices of the Royal Astronomical Society*, vol. 524, pp. 5993 – 6003, Jul. 2023
©DOI: https://doi.org/10.1093/mnras/stad2017

Monthly Notices of the ROYAL ASTRONOMICAL SOCIETY

MNRAS **524,** 5993–6003 (2023) https://doi.org/10.1093/mnras/stad2017
Advance Access publication 2023 July 17

Deep search for glycine conformers in Barnard 5

Tadeus Carl,[1]★ E. S. Wirström,[1] P. Bergman,[1] S. B. Charnley,[2] Y.-L. Chuang[3] and Y.-J. Kuan[3]

[1]*Onsala Space Observatory, Department of Space, Earth and Environment, Chalmers University of Technology, SE-439 92, Onsala, Sweden*
[2]*Astrochemistry Laboratory and the Goddard Center for Astrobiology, Mailstop 691, 8800 Greenbelt Road, Greenbelt, MD 20770, USA*
[3] *Department of Earth Sciences, National Taiwan Normal Univesity, No. 88, Ting-Chou Rd, Wen-Shan District, Taipei City, Taiwan 11677, China*

Accepted 2023 June 30. Received 2023 June 30; in original form 2023 May 25

ABSTRACT

One of the most fundamental hypotheses in astrochemistry and astrobiology states that crucial biotic molecules like glycine (NH_2CH_2COOH) found in meteorites and comets are inherited from early phases of star formation. Most observational searches for glycine in the interstellar medium have focused on warm high-mass molecular cloud sources. However, recent studies suggest that it might be appropriate to shift the observational focus to cold low-mass sources. We aim to detect glycine towards the so-called methanol hotspot in the Barnard 5 dark cloud. The hotspot is a cold source ($T_{\rm gas} \approx 7.5$ K) with yet high abundances of complex organic molecules (COMs) and water in the gas phase. We carried out deep pointed observations with the Onsala 20 m telescope, targeting several transitions of glycine conformers I and II (Gly-I and Gly-II) in the frequency range 70.2–77.9 GHz. No glycine lines are detected towards the targeted position, but we use a line stacking procedure to derive sensitive abundance upper limits w.r.t. H_2 for Gly-I and Gly-II, i.e. $\leq$(2–5) $\times$ 10^{-10} and $\leq$(0.7–3) $\times$ 10^{-11}, respectively. The obtained Gly-II upper limits are the most stringent for a cold source, while the Gly-I upper limits are mostly on the same order as previously measured limits. The measured abundances w.r.t. H_2 of other COMs at the B5 methanol hotspot range from 2 $\times$ 10^{-10} (acetaldehyde) to 2 $\times$ 10^{-8} (methanol). Hence, based on a total glycine upper limit of (2–5) $\times$ 10^{-10}, we cannot rule out that glycine is present but undetected.

Key words: astrobiology – astrochemistry – ISM: abundances – ISM: molecules.

1 INTRODUCTION

Glycine (NH_2CH_2COOH) is the simplest amino acid used in the metabolism of terrestrial lifeforms. Since its first detection in meteorites in the 1970s (Kvenvolden et al. 1970; Cronin & Pizzarello 1999; Ehrenfreund et al. 2001; Botta et al. 2002; Glavin et al. 2006; Koga & Naraoka 2017) it has been speculated that prebiotic materials have been delivered to Earth by smaller impacting bodies (Hoyle & Wickramasinghe 1977; Ehrenfreund & Charnley 2000). This hypothesis is supported by the identification of glycine in the comas of comets 81P/Wild 2 (Elsila, Glavin & Dworkin 2009) and 67P/Churyumov–Gerasimenko (Altwegg et al. 2016; Hadraoui et al. 2019), as well as in samples from asteroid (162173) Ryugu (Naraoka et al. 2023). There is general consensus that meteoric glycine is mainly the product of aqueous alteration in subsurface layers of the asteroidal host bodies (Lee et al. 2009; Ioppolo et al. 2021, and references therein). On the other hand, the study by Hadraoui et al. (2019) suggests that cometary glycine is more pristine and might indeed have an interstellar origin.

To test the claimed hypothesis, astronomers have searched for signs of interstellar amino acids, in particular glycine, for more than four decades (Brown et al. 1979; Hollis et al. 1980; Snyder et al. 1983; Berulis et al. 1985; Guélin & Cernicharo 1989; Combes, Rieu & Wlodarczak 1996; Ceccarelli et al. 2000; Hollis et al. 2003a, b; Kuan et al. 2003; Snyder et al. 2005; Cunningham et al. 2007; Jones et al. 2007; Belloche et al. 2008; Guélin et al. 2008; Drozdovskaya et al. 2019; Jiménez-Serra et al. 2020). However, no clear detection has been made to this day. Most studies have focused on high-mass star-forming regions (especially hot cores in Sgr B2 and Ori A), although some low-mass dark cloud sources have been included in the sample sets of Brown et al. (1979) and Snyder et al. (1983). Only Ceccarelli et al. (2000) and Drozdovskaya et al. (2019) investigated low-mass protostellar sources (hot corinos).

Hot cores with kinetic temperatures of 100–200 K are often the first choice when searching for complex organic molecules (COMs) due to the overall large amount of available material combined with a rich chemistry and line variety. In the case of glycine, the observational focus on hot cores has been justified by early theoretical (Sorrell 2001; Woon 2002; Garrod 2013) and experimental (Bernstein et al. 2002; Muñoz Caro et al. 2002; Holtom et al. 2005; Lee et al. 2009) studies, indicating that glycine could only form by means of energetic (UV/electron/thermal) processing of interstellar ices, involving temperatures >50 K. There is, however, increasing evidence that a shift of focus to cold (∼10 K) low-mass sources might be appropriate when searching for glycine.

It is known from observations since the 1980s that COMs like methanol (CH_3OH), acetaldehyde (CH_3CHO), or methyl formate (CH_3OCHO) can reach significant abundances in cold molecular cloud sources such as TMC-1, L1689B, L1544, and Barnard 5 (Matthews, Friberg & Irvine 1985; Friberg et al. 1988; Marcelino et al. 2007; Bacmann et al. 2012; Vastel et al. 2014; Jiménez-Serra

★ E-mail: tadeus.carl@chalmers.se

et al. 2016; Taquet et al. 2017). Based on that high degree of chemical complexity, Jiménez-Serra et al. (2014) tested the detectability of glycine with radiative transfer models for the prototypical pre-stellar core L1544, indicating that several glycine transitions with an upper level energy $E_u < 30$ K and an Einstein coefficient of spontaneous emission $A_{ul} \geq 10^{-6}$ s^{-1} can reach detectable intensities in cold sources. Furthermore, severe observational issues with hot cores, such as line blending and multiple velocity components, can be avoided when observing colder, quiescent sources with lower line densities and narrower line widths. In addition, a combined experimental and theoretical study by Ioppolo et al. (2021) has recently shown for the first time that glycine can form on the surface of interstellar ices at low temperatures (∼13 K) and in the absence of energetic irradiation. Experiments and modelling agree that the main route of formation is the radical–radical reaction

$$NH_2CH_2 + HOCO \longrightarrow NH_2CH_2COOH. \quad (1)$$

As many molecules, glycine has several stable conformational isomers with different zero-point energies. The two lowest-energy conformers of glycine are denoted with I and II (hereafter, Gly-I and Gly-II). The zero-point energy of Gly-II is approximately 1007 ± 101 K higher than that of the lower energy conformer Gly-I, while the electric dipole moment of Gly-II is approximately six times higher than that of Gly-I (Lovas et al. 1995). Since spectral intensity is proportional to the square of the dipole moment, the intensity of Gly-II is enhanced by a factor of approximately 36 over Gly-I. This leads to an anomalous high intensity ratio of both conformers, i.e. a much weaker rotational spectrum of Gly-I compared to Gly-II, despite the lower zero-point energy of Gly-I (cf. Snyder et al. 1983). For this reason, Gly-II was the first conformer to be spectroscopically identified in the laboratory (Brown et al. 1978; Suenram & Lovas 1978; Suenram & Lovas 1980). It is also for this reason that early searches for glycine in the interstellar medium (ISM; Brown et al. 1979; Snyder et al. 1983; Berulis et al. 1985) focused on transitions of Gly-II, while all later studies focused either on Gly-I or included transitions of both conformers.

Based on the spectroscopic properties of Gly-I and Gly-II, and on purely thermodynamic grounds, much higher abundances of Gly-I are expected over the whole molecular cloud temperature range (10–200 K). However, observations have shown that an equilibrium isomerization is not always established in molecular clouds, but rather that the high-energy conformer of a molecule can have much higher abundances than expected (García de la Concepción et al. 2022). In the case of formic acid (HCOOH), the gas phase abundance ratio of the high-energy *c*(*is*)-conformer to the low-energy *t*(*rans*)-conformer can reach values of 5–6 per cent, as found towards two dark cloud sources, Barnard 5 and L483, with kinetic temperatures of around 10 K (Taquet et al. 2017; Agúndez et al. 2019). Those ratios are several tens of orders of magnitude higher than predicted by gas phase isomerization models including ground-state quantum tunnelling effects (García de la Concepción et al. 2022). This indicates that some key isomerization mechanisms are not fully understood. Photoswitching mechanisms as proposed by Cuadrado et al. (2016) can likely be neglected in well-shielded dark cloud regions as B5 and L483. However, Taquet et al. (2017) suggest that the solid-state formation of molecules on interstellar ices can produce non-equilibrium isomerizations because the outcome of a surface reaction depends also on the relative orientation between a surface species and the incoming gas phase species (e.g. Rimola, Sodupe & Ugliengo 2012; Enrique-Romero et al. 2016). Furthermore, in the particular case of formic acid, it is assumed that one major route of solid-state formation is the reaction chain

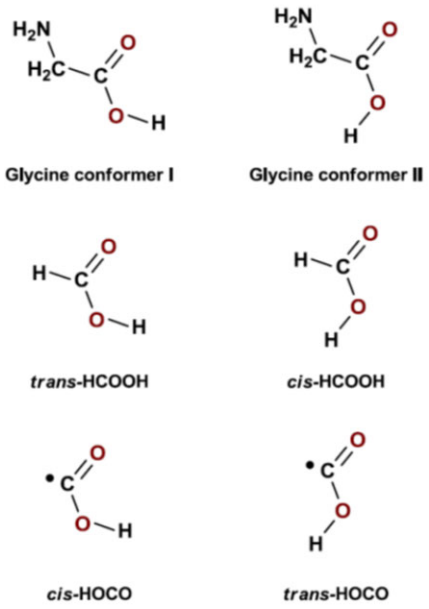

Figure 1. Schematic view of the conformers of parent and daughter molecules in the considered reactions that form glycine (NH_2CH_2COOH) and formic acid (HCOOH) on an interstellar ice surface. Left column: hydrogenation of *c*-HOCO leads to *t*-HCOOH, while the radical–radical reaction NH_2CH_2 + *c*-HOCO leads to Gly-I. Right column: hydrogenation of *t*-HOCO leads to *c*-HCOOH, and NH_2CH_2 + *t*-HOCO forms Gly-II. Credit: Jose Aponte.

$$CO + OH \longrightarrow HOCO, \quad (2)$$

$$HOCO + H \longrightarrow HCOOH, \quad (3)$$

with most of the HOCO radical formed in its low-energy *trans*-configuration (Goumans, Uppal & Brown 2008). However, the hydrogenation of *t*-HOCO leads to *c*-HCOOH, which can significantly increase the gas phase *cis*/*trans* ratio of formic acid, once desorbed from the grain surface. We argue that the same principles can lead to anomalously high Gly-II/Gly-I gas phase ratios in cold sources like B5, if it is assumed that glycine forms in the solid phase via reaction (1), and by noting that Gly-II is formed from reactions of *t*-HOCO and NH_2CH_2 (cf. Fig. 1). However, recent modelling work by Garrod et al. (2022) suggests that several other glycine formation routes can be very efficient at dark cloud conditions and potentially dominate over reaction (1). Of these, only the reaction of NH_2 (or of NH followed by H) with CH_2COOH could lead to glycine conformers I and II since the latter radical is itself formed from HOCO. Thus, in this case, the Gly-II/Gly-I ratio should also follow the *c*/*t*-HCOOH. Therefore, gas phase observations of the Gly-II/Gly-I ratio in cold sources could in principle be used to investigate the main formation routes of glycine at low temperatures.

Based on the above considerations, the methanol hotspot[1] in the Barnard 5 (hereafter B5) dark cloud (Perseus, $d = 302 \pm 21$ pc; Zucker et al. 2018) is a promising target to search for interstellar glycine. It is located approximately 0.55 pc to the northwest of the prominent class-I protostar IRS-1 (see maps in Wirström et al. 2014; Taquet et al. 2017). The location of the hotspot is neither

[1]Following Wirström et al. (2014), the term methanol 'hotspot' is used to indicate the position of the methanol intensity peak.

associated with a prestellar core nor a protostellar source (Wirström et al. 2014, and references therein). The detection of abundant water (8×10^{-9}) by Wirström et al. (2014) as well as methanol (2×10^{-8}) and other COMs ($\sim 10^{-10}$) by Taquet et al. (2017) confirms the chemical complexity of the region; abundances are relative to H_2. In addition, it is in this position that *c*-HCOOH has been detected at a relative abundance of 6 per cent as compared to *t*-HCOOH (Taquet et al. 2017). The H_2 column density and dust temperature towards the hotspot are estimated from data of the Herschel Gould Belt survey[2] (HGBS) as $N(H_2) = 1 \times 10^{22}\,cm^{-2}$ and $T_{dust} = 13\,K$, respectively[3] (André et al. 2010; Roy et al. 2014). Non-local thermodynamic equilibrium (LTE) radiative transfer calculations of methanol emission by Taquet et al. (2017) reveal a gas kinetic temperature of $T_{kin} = 7.5 \pm 1.5\,K$ and a gas density of $n(H_2) = (2.25 \pm 1.50) \times 10^5\,cm^{-3}$.

For our study, single-point observations were made with the Onsala 20 m telescope towards the B5 hotspot, with several Gly-I and Gly-II transitions targeted in the frequency range ~70–78 GHz. The observations are described in Section 2, and we present the resulting spectrum and the detected molecules in Section 3. Glycine was not detected, but we derive sensitive upper limits for both glycine conformers using spectral line stacking, as described in Section 4. In that section, we also present the column density calculation for other detected molecules. In Section 5, the derived glycine upper limits are compared to limits for other sources as well as to reported abundances of other COMs at the position of the B5 hotspot. We summarize our conclusions in Section 6.

2 OBSERVATIONS

Our LTE analysis using $T_{ex} = 7.5\,K$ predicts that a number of Gly-I and Gly-II transitions in the 4 mm band will have detectable peak intensities if the glycine abundance and distribution at the B5 hotspot is similar to other detected COMs (Taquet et al. 2017). The considered transitions are presented in Table 1 with their spectroscopic properties. Single point observations were carried out towards the B5 hotspot with the Onsala 20 m telescope at 70.2–77.9 GHz. We observed for a total of ~150 h in three observation runs in 2017, 2018, and 2022.

The receiver frontend was a 4 mm dual-polarization sideband-separating HEMT receiver (Walker et al. 2016). This frontend has common warm optics with the 3 mm system (Belitsky et al. 2015). In the 2017 observations, the centre frequency was 72 GHz, and in 2018, it was 76 GHz. In the 2022 observations, we used two settings with the centre frequencies from 2017 and 2018, referred to as S1 and S2, respectively. We used a symmetric dual-beam switching mode with a switching frequency of 1 Hz and a beam throw of 11 arcmin in azimuth. The half-power beamwidth at 74 GHz is 51 arcsec. We pointed the antenna towards 03:47:32.10 RA (J2000) and 32:56:43.0 Dec. (J2000). Pointing and focus accuracy was checked with observations of SiO masers at 86.2 GHz, and was found to be within 5 arcsec for the pointing. The receiver backend was a FFT spectrometer, consisting of four modules. To increase the effective observation time, we used the dual-polarization mode, covering about 2.5 GHz per module pair. This resulted in 4 GHz total bandwidth per frequency setting, with an overlap of about 1 GHz. The frequency resolution was 76.3 kHz, corresponding to a velocity resolution of 0.31 km s^{-1} at 74 GHz. The data was calibrated using the chopper-wheel method and the estimated calibration uncertainty was 10 per cent. In the 2017, 2018, and 2022 observations, the system noise temperature varied mostly within 195–450, 165–405, and 170–360 K, respectively, but for shorter periods of worse observing conditions it increased significantly above this.

We used the 20 m data reduction software XS for data reduction and correction for frequency- and elevation-dependent main beam efficiency and Doppler-shifted spectral resolution. Spectra with noise temperatures above 500 K were excluded. We combined our 2017 and 2018 data with our 2022-S1 and 2022-S2 data, respectively, and averaged the dual-polarization spectra weighted by their system temperature and integration time. We fitted and subtracted a linear baseline to line-free regions in the 2017-2022-S1 and 2018-2022-S2 averaged spectra, and combined them to one spectrum.

Table 1. Targeted Gly-I and Gly-II transitions and their spectroscopic properties, taken from CDMS (cdms.astro.uni-koeln.de; see also Ilyushin et al. 2005).

Transition	Frequency (GHz)	E_u (K)	A_{ul} (s^{-1})	g_u –
Gly-I				
$10_{3,7} - 9_{3,6}$	71.611 56	21.5	1.5×10^{-6}	63
$11_{2,10} - 10_{2\,9}$	71.646 39	22.4	1.6×10^{-6}	69
$10_{2,8} - 9_{2,7}$	71.910 30	20.2	1.6×10^{-6}	63
$12_{1,12} - 11_{1,11}$	72.559 35	23.3	1.8×10^{-6}	75
$12_{0,12} - 11_{0,11}$	72.601 11	23.3	1.8×10^{-6}	75
$11_{1,10} - 10_{1,9}$	72.841 25	22.3	1.7×10^{-6}	69
$6_{3,4} - 5_{2,3}$	73.503 46	9.9	3.5×10^{-7}	39
$11_{3,9} - 10_{3,8}$	74.923 44	24.7	1.8×10^{-6}	69
$4_{4,1} - 3_{3,0}$	75.795 27	8.6	7.2×10^{-7}	27
$4_{4,0} - 3_{3,1}$	75.802 14	8.6	7.2×10^{-7}	27
$11_{4,8} - 10_{4,7}$	75.922 23	27.1	1.8×10^{-6}	69
$11_{4,7} - 10_{4,6}$	76.913 70	27.2	1.8×10^{-6}	69
$6_{3,3} - 5_{2,4}$	77.199 06	9.9	3.7×10^{-7}	39
$12_{2,11} - 11_{2,10}$	77.652 29	26.1	2.1×10^{-6}	75
Gly-II				
$10_{3,8} - 9_{3,7}$	71.141 50	21.7	5.2×10^{-5}	63
$10_{6,5} - 9_{6,4}$	71.614 83	30.2	3.8×10^{-5}	63
$10_{6,4} - 9_{6,3}$	71.617 29	30.2	3.8×10^{-5}	63
$10_{5,6} - 9_{5,5}$	71.877 04	26.8	4.5×10^{-5}	63
$10_{5,5} - 9_{5,4}$	71.942 25	26.8	4.5×10^{-5}	63
$10_{4,7} - 9_{4,6}$	72.065 95	24.0	5.0×10^{-5}	63
$10_{4,6} - 9_{4,5}$	72.944 52	24.0	5.2×10^{-5}	63
$11_{2,10} - 10_{2,9}$	74.121 76	23.1	6.2×10^{-5}	69
$10_{2,8} - 9_{2,7}$	74.838 70	21.0	6.4×10^{-5}	63
$12_{1,12} - 11_{1,11}$	74.926 70	24.1	6.7×10^{-5}	75
$12_{0,12} - 11_{0,11}$	74.950 73	24.1	6.7×10^{-5}	75
$11_{1,10} - 10_{1,9}$	75.009 64	23.0	6.5×10^{-5}	69
$10_{3,7} - 9_{3,6}$	75.378 86	22.2	6.3×10^{-5}	63
$11_{3,9} - 10_{3,8}$	77.916 34	25.4	7.0×10^{-5}	69

3 RESULTING SPECTRUM AND LINE IDENTIFICATION

The resulting spectrum of our observations towards the B5 hotspot is shown in Fig. 2. The frequencies of the targeted Gly-I and Gly-II transitions from Table 1 are marked by solid green and blue lines, respectively. The selection of considered glycine transitions is described in more detail in Section 4.1. The RMS noise towards

[2] http://www.herschel.fr/cea/gouldbelt/en/Phocea/Vie_des_labos/Ast/ast_visu.php?id_ast=66

[3] We used $N(H_2) = 1 \times 10^{22}\,cm^{-2}$ to update the abundances derived for water and COMs in Wirström et al. (2014) and Taquet et al. (2017).

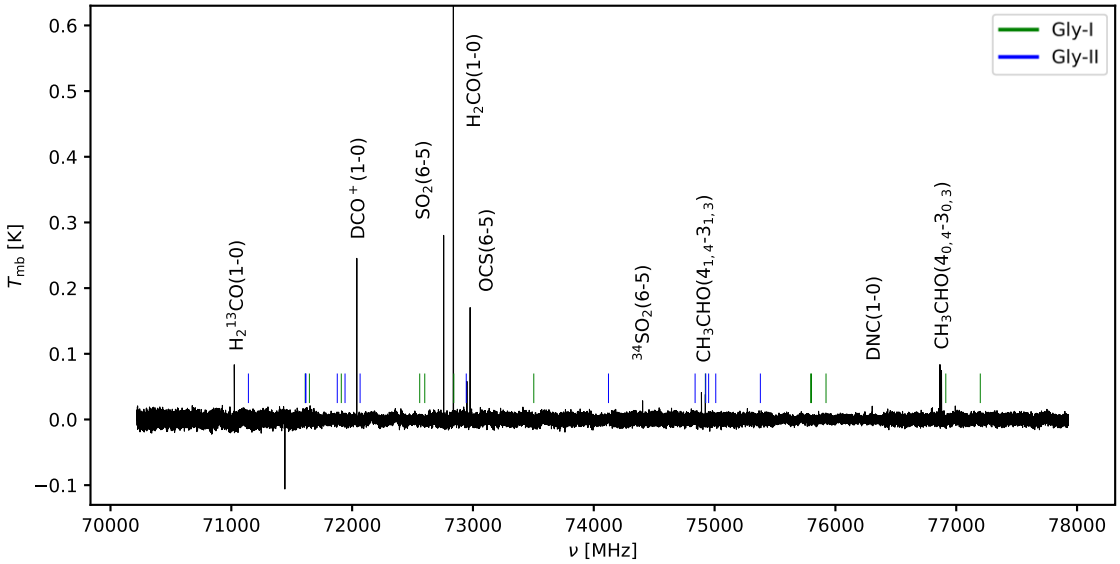

Figure 2. Spectrum towards the B5 methanol hotspot in the frequency range 70.2–77.9 GHz. The solid green and blue lines mark the frequencies of targeted Gly-I and Gly-II transitions, respectively. The peak intensity of the truncated H_2CO(1-0) line is at ∼1.22 K. The negative feature at ∼71.44 GHz and the positive feature at ∼72.95 GHz, left of the OCS(6-5) peak, are bad channels.

the low-frequency end of the spectrum is ∼6.2 mK. It decreases with frequency to reach ∼4.2 mK towards the high-frequency end. In regions where the backend modules overlap, around 72 and 76 GHz, there is a noticeable decrease in noise due to the spectral resampling resulting in an increase of the effective channel width.

None of the targeted glycine lines shows an intensity above the noise level but we use spectral line stacking to derive column density and abundance upper limits for Gly-I and Gly-II, separately. This is described in more detail in Section 4.1.

We do detect emission lines from acetaldehyde (CH_3CHO), formaldehyde (H_2CO; $H_2{}^{13}CO$), the DCO^+ ion, deuterated hydrogen isocyanide (DNC), carbonyl sulfide (OCS), and sulfur dioxide (SO_2; $^{34}SO_2$). The detected transitions are listed in column two of Table 2 together with their line width and integrated intensity (last two columns). The individual spectral lines with their Gaussian fits are shown in Fig. A1.

4 ANALYSIS

4.1 Glycine upper limits

Spectral line stacking is used to derive the highest sensitivity estimates possible for the column density upper limits of Gly-I and Gly-II. Our stacking method consists of four steps:

(1) identification of the presumably strongest transitions,
(2) extraction of spectra around the transition frequencies of the identified transitions,
(3) conversion of intensity scale to column density scale in all spectra, assuming LTE conditions,
(4) averaging of the obtained column density spectra.

Assuming LTE conditions and optically thin emission, the total, beam-averaged column density of a molecule can be written as

$$N_{\rm tot} = \frac{1}{C}\int T_{\rm mb}{\rm d}v, \tag{4}$$

where $\int T_{\rm mb}{\rm d}v$ is the integrated intensity and C is a constant, given as

$$C = \frac{hc^3}{8\pi k_{\rm B}}\frac{g_{\rm u}A_{\rm ul}}{\nu^2}\frac{\exp(-E_{\rm u}/T_{\rm ex})}{Q_{\rm rot}(T_{\rm ex})}\left[1-\frac{J_\nu(T_{\rm bg})}{J_\nu(T_{\rm ex})}\right]. \tag{5}$$

h is the Planck constant, c is the speed of light, $k_{\rm B}$ is the Boltzmann constant, $T_{\rm ex}$ is the excitation temperature, and $T_{\rm bg}$ is the CMB temperature. The line-specific spectroscopic parameters are the total degeneracy $g_{\rm u}$, Einstein coefficient for spontaneous emission $A_{\rm ul}$, transition (rest) frequency ν, upper state energy $E_{\rm u}$ (in Kelvin), and the rotational partition function $Q_{\rm rot}$ at $T = T_{\rm ex}$. Furthermore, $J_\nu(T)$ is the temperature equivalent of the specific intensity, given as

$$J_\nu(T) = \frac{h\nu}{k_{\rm B}}\left[\exp\left(\frac{h\nu}{k_{\rm B}T}\right)-1\right]^{-1}. \tag{6}$$

The last term in equation (5) is only needed if $T_{\rm ex}$ is comparable to $T_{\rm bg}$, which is the case for the B5 hotspot. According to equation (4), the column density in one spectral channel of width Δv is given by

$$N_{\rm tot}^{\rm ch} = \frac{T_{\rm A}^{\rm ch}\Delta v}{C}, \tag{7}$$

and for step (1), we estimate the antenna temperature in one channel ($T_{\rm A}^{\rm ch}$) for all Gly-I and Gly-II transitions in the frequency range 70.2–77.9 GHz. We assume $N_{\rm tot}^{\rm ch} = 3.6\times10^{12}\,{\rm cm}^{-2}$ for Gly-I and $N_{\rm tot}^{\rm ch} = 2.0\times10^{11}\,{\rm cm}^{-2}$ for Gly-II, and set $\Delta v = 0.4\,{\rm km\,s}^{-1}$ and $T_{\rm ex} = 7.5$ K, based on temperature estimates for the B5 methanol hotspot (Taquet et al. 2017). Only transitions for which $T_{\rm A}^{\rm ch} > T_{\rm lim}$ are considered, and we use 2 and 1 mK as temperature limits $T_{\rm lim}$ for Gly-I and Gly-II, respectively. The considered transitions are listed in Table 1, together with the spectroscopic parameters that feed into the constant C, i.e. $E_{\rm u}$, $A_{\rm ul}$, and $g_{\rm u}$. The rotational partition functions of Gly-I and Gly-II are 1350.38 and 1310.26 at $T = 9.375$ K, respectively (values from CDMS[4]; see also Ilyushin et al. 2005). Based on the theoretical temperature dependence for the rotational

[4] cdms.astro.uni-koeln.de

Table 2. Detected transitions with their spectroscopic and observed parameters; all uncertainties are 1σ values. Spectroscopic parameters are taken from CDMS (cdms.astro.uni-koeln.de) and JPL (spec.jpl.nasa.gov; only for CH_3CHO; see also Kleiner, Lovas & Godefroid 1996).

Molecule	Transition	ν (GHz)	E_u (K)	A_{ul} (s^{-1})	g_u	$Q_{rot}(9.375\,K)$	FWHM$^{(a)}$ ($km\,s^{-1}$)	$\int T_{mb}dv$ $^{(b)}$ ($mKkm\,s^{-1}$)
A − CH_3CHO	$4_{14} - 3_{13}$	74.891 67	11.3	1.3×10^{-5}	9$^{(c)}$	66.02$^{(d)}$	0.67 ± 0.07	30.2 ± 3.3
	$4_{04} - 3_{03}$	76.878 95	9.2	1.5×10^{-5}	9$^{(c)}$	66.02$^{(d)}$	0.51 ± 0.06	45.8 ± 2.8
E − CH_3CHO	$4_{14} - 3_{13}$	74.924 13	11.3	1.3×10^{-5}	9$^{(c)}$	66.02$^{(d)}$	0.75 ± 0.10	27.0 ± 2.7
	$4_{04} - 3_{03}$	76.866 43	9.3	1.5×10^{-5}	9$^{(c)}$	66.02$^{(d)}$	0.67 ± 0.03	60.8 ± 2.9
H_2CO	$1_{01} - 0_{00}$	72.837 94	3.5	8.2×10^{-6}	3	13.80	1.04 ± 0.04	1370.1 ± 3.8
$H_2{}^{13}CO$	$1_{01} - 0_{00}$	71.024 78	3.4	7.6×10^{-6}	3	14.13	0.77 ± 0.07	69.3 ± 4.9
DCO^+	$1 - 0$	72.039 31	3.5	2.3×10^{-5}	3	5.77	1.29 ± 0.06	331.6 ± 3.0
DNC	$1 - 0$	76.305 73	3.7	1.6×10^{-5}	3	5.47	1.92 ± 0.27	29.1 ± 2.4
OCS	$6 - 5$	72.976 77	12.3	1.1×10^{-6}	13	32.46	0.60 ± 0.03	102.2 ± 3.5
SO_2	$6_{0,6} - 5_{1,5}$	72.758 24	19.2	2.8×10^{-6}	13	33.07	0.70 ± 0.02	220.5 ± 4.0
$^{34}SO_2$	$6_{0,6} - 5_{1,5}$	74.404 57	19.1	3.0×10^{-6}	13	33.64	0.49 ± 0.13	14.0 ± 2.6

Notes. (*a*) Derived from Gaussian fits (see Fig. A1); (*b*) Derived by integration over line channels (see Fig. A1).
(*c*) We use $g_u = 2J + 1$ to be consistent with $Q_{rot}(T)$ from Nummelin et al. (1998).
(*d*) From Nummelin et al. (1998) for A-/E-species separated, i.e. $Q_{rot}(T) = 2.3 \times T^{3/2}$.

partition function of (a)symmetric-top molecules, we determine the partition function at T_{ex} as

$$Q_{rot}(T_{ex}) = Q_{rot}(T)\left(\frac{T_{ex}}{T}\right)^{3/2}. \quad (8)$$

As step (2), we extract spectra over 50 $km\,s^{-1}$ around the transition frequencies of the considered Gly-I and Gly-II transitions, and determine 1σ noise temperatures T^{σ}_{mb} in line-free regions (compare Figs A2 and A3). In order to obtain a single column density estimate from the obtained spectra, the individual spectroscopic line parameters must be included before averaging. In step (3), we do this by transferring the intensity axis of each spectrum to a column density axis by using

$$N_{tot}(v) = \frac{T_{mb}(v)\Delta v}{C}, \quad (9)$$

where $T_{mb}(v)$ is the observed main beam temperature. Finally, as step (4), we average the obtained column density spectra weighted by 1σ noise column density, which we calculate for all spectra as

$$N^{\sigma}_{tot} = \frac{T^{\sigma}_{mb}\Delta v}{C}. \quad (10)$$

The stacked column density spectra for Gly-I and Gly-II are shown in Fig. 3. Even in the stacked spectra, glycine is still not detected, but we use the obtained noise level to derive sensitive upper limits. In both spectra, the dashed blue line marks the 1σ column density noise level. The corresponding 3σ column density upper limits of Gly-I and Gly-II are presented in Table 3 together with the abundance upper limits relative to H_2.

4.2 Column densities of detected species

Column densities of H_2CO, $H_2{}^{13}CO$, DCO^+, DNC, OCS, SO_2, and $^{34}SO_2$ are calculated from equation (4), assuming LTE conditions and optically thin emission. The required spectroscopic parameters are given in Table 2, and we use equation (8) to determine the rotational partition functions at $T_{ex} = 7.5$ K. For the linear molecules DNC and OCS, we use the equivalent relation

$$Q_{rot}(T_{ex}) = Q_{rot}(T)\frac{T_{ex}}{T}. \quad (11)$$

In the case of the H_2CO(1-0) line, we expect the optically thin approximation to fail, and derive an estimate for the optical depth τ using the rare isotopologue method with

$$\frac{W_{12}}{W_{13}} = [1 - \exp(-\tau)]\left[1 - \exp\left(\frac{-\tau}{^{12}C/^{13}C}\right)\right]^{-1}, \quad (12)$$

where W_{12} and W_{13} are the integrated intensities of H_2CO(1-0) and $H_2{}^{13}CO$(1-0), respectively. We assume $^{12}C/^{13}C = 68$ for the local ISM, based on Milam et al. (2005). We get $\tau = 3.4$ and calculate the corrected column density of H_2CO using

$$N^{corr}_{tot} = \frac{\tau}{1 - \exp(-\tau)}N^{thin}_{tot}, \quad (13)$$

where N^{thin}_{tot} is the optically thin estimate.

The derived column densities are presented in Table 3, together with the molecular abundances relative to H_2.

4.3 Rotation diagram acetaldehyde

Following Goldsmith & Langer (1999), we perform a rotation diagram analysis for the four detected transitions of acetaldehyde (CH_3CHO), listed in Table 2, together with six transitions detected towards the B5 hotspot by Taquet et al. (2017). We assume optically thin emission and an LTE population of levels, and calculate the upper state column densities N_u as

$$N_u = \frac{8\pi k_B \nu^2}{A_{ul}hc^3}\int T_{mb}dv. \quad (14)$$

Plotting $\ln(N_u/g_u)$ against E_u and fitting the data linearly yields an excitation temperature of $T_{ex} = 5.8 \pm 0.8$ K and a total column density of $N_{tot} = (1.4 \pm 0.5) \times 10^{12}\,cm^{-2}$. Fitting the data for A- and E-species separately yields approximately the same result as fitting the data for both species combined, as expected from the low difference in ground state energy (0.1 K; Kleiner et al. 1996). When finding an excitation temperature so close to the CMB temperature ($T_{bg} = 2.73$ K) it is important to consider its influence on excitation using the correction term

$$C_{bg} = \left[1 - \frac{J_\nu(T_{bg})}{J_\nu(T_{ex})}\right]^{-1}. \quad (15)$$

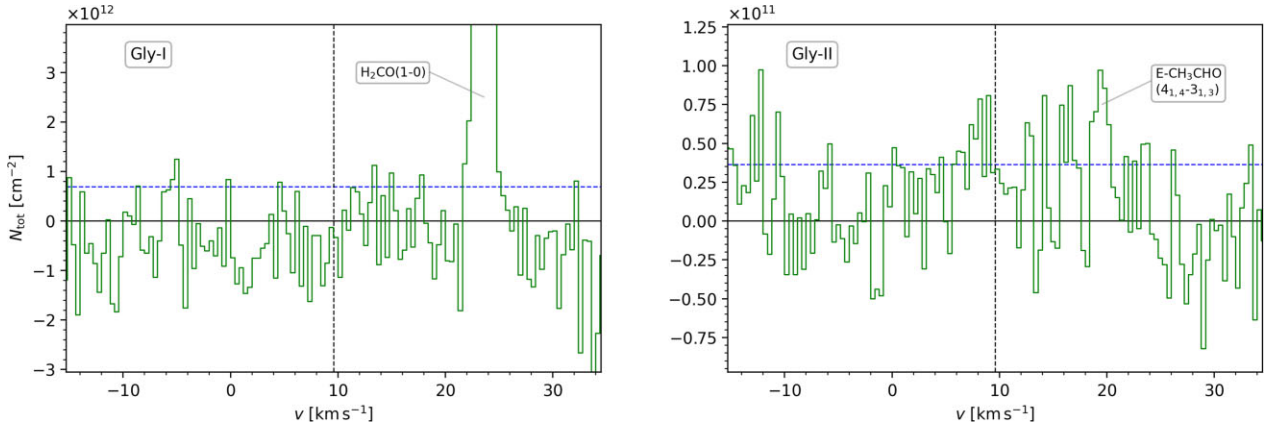

Figure 3. Stacked spectra for Gly-I (left) and Gly-II (right) in column density scale, determined from equation (9). In both spectra, the dashed blue line marks the 1σ column density noise level, and the dashed black line marks the LSR velocity of the B5 methanol hotspot. The column density peaks at $\sim 24\,\mathrm{km\,s^{-1}}$ (left) and $\sim 20\,\mathrm{km\,s^{-1}}$ (right) arise from the detected H_2CO(1-0) and $CH_3CHO(4_{1,4}\text{-}3_{1,3})$ transitions, respectively. The regions where the peaks appear are excluded from the RMS calculation (compare Figs A2 and A3).

Table 3. Beam-averaged column densities and abundances relative to H_2; uncertainties are 1σ values and upper limits are 3σ values. We use $N(H_2) = 1 \times 10^{22}\,\mathrm{cm^{-2}}$ from HGBS data (Roy et al. 2014).

Molecule	$N_{\rm tot}$ ($\mathrm{cm^{-2}}$)	$N_{\rm tot}/N(H_2)$
$CH_3CHO^{(a)}$	$(1.97 \pm 0.65) \times 10^{12}$	2×10^{-10}
H_2CO	$(4.14 \pm 0.01) \times 10^{13}$	4×10^{-9}
$H_2{}^{13}CO$	$(6.20 \pm 0.44) \times 10^{11}$	6×10^{-11}
DCO^+	$(4.14 \pm 0.04) \times 10^{11}$	4×10^{-11}
DNC	$(6.27 \pm 0.51) \times 10^{10}$	6×10^{-12}
OCS	$(1.31 \pm 0.04) \times 10^{13}$	1×10^{-9}
SO_2	$(2.48 \pm 0.04) \times 10^{13}$	3×10^{-9}
$^{34}SO_2$	$(1.54 \pm 0.28) \times 10^{12}$	2×10^{-10}
Gly-I	$\leq 4.6 \times 10^{12}$ (b)	$\leq 5 \times 10^{-10}$ (b)
	$\leq 2.1 \times 10^{12}$ (c)	$\leq 2 \times 10^{-10}$ (c)
	$\leq 1.6 \times 10^{12}$ (d)	$\leq 2 \times 10^{-10}$ (d)
Gly-II	$\leq 3.3 \times 10^{11}$ (b)	$\leq 3 \times 10^{-11}$ (b)
	$\leq 1.1 \times 10^{11}$ (c)	$\leq 1 \times 10^{-11}$ (c)
	$\leq 7.1 \times 10^{10}$ (d)	$\leq 7 \times 10^{-12}$ (d)

Notes. (*a*) $T_{\rm ex} = 5.7\,\mathrm{K}$, from CH_3CHO rotation diagram analysis. (*b*) $T_{\rm ex} = 5\,\mathrm{K}$; (*c*) $T_{\rm ex} = 7.5\,\mathrm{K}$; (*d*) $T_{\rm ex} = 10\,\mathrm{K}$.

The corrected upper state column density is then given by

$$N_{\rm u}^{\rm corr} = C_{\rm bg}\, N_{\rm u}. \tag{16}$$

Iterating the updated values of $N_{\rm u}^{\rm corr}$ and $T_{\rm ex}$, the asymptotic values of excitation temperature and total column density are $T_{\rm ex} = 5.7\,\mathrm{K}$ and $N_{\rm tot} = (2.0 \pm 0.6) \times 10^{12}\,\mathrm{cm^{-2}}$. The resulting abundance relative to H_2 is 2×10^{-10} (see Table 3). The final rotation diagram is shown in Fig. 4. For the calculation of total column density, we use the rotational partition function derived in Nummelin et al. (1998) as $Q_{\rm rot}(T) = 4.6 \times T^{3/2}$ for A- and E-species combined, and for $g_{\rm u} = 2J + 1$. Considering both species separately using the same iterative process as described gives an A/E ratio of 0.88, which is close to the expected ratio of unity.

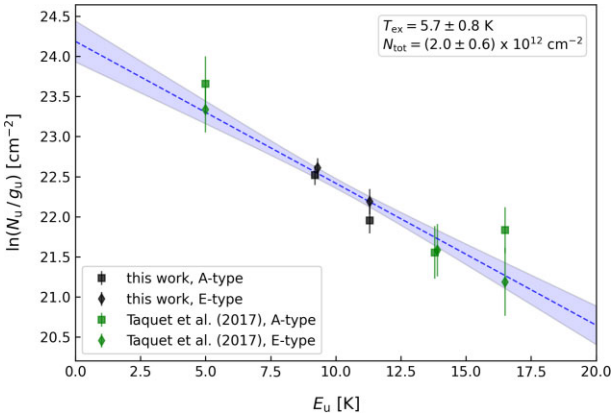

Figure 4. Rotation diagram for acetaldehyde (CH_3CHO) transitions detected in this work (black symbols) and in Taquet et al. (2017; green symbols) towards the B5 methanol hotspot. A- and E-type transitions are depicted as squares and diamonds, respectively. The best linear fit to the data is shown as dashed blue line with 1σ confidence interval (shaded blue area). Considering the influence of cosmic microwave background (CMB) radiation, the resulting excitation temperature is $5.7 \pm 0.8\,\mathrm{K}$, and the total column density is $(2.0 \pm 0.6) \times 10^{12}\,\mathrm{cm^{-2}}$.

5 DISCUSSION

The excitation temperature of $5.7 \pm 0.8\,\mathrm{K}$ obtained from the CH_3CHO data indicates possible sub-thermal excitation of the rotational levels of acetaldehyde at the position of the B5 hotspot (where the gas kinetic temperature is estimated from methanol lines as $T_{\rm kin} = 7.5 \pm 1.5\,\mathrm{K}$). Based on that, and in order to cover a larger range of possible excitation temperatures for glycine, we calculate two more sets of 3σ upper limits for 5 and 10 K (see Table 3). For the lower excitation limit of $T_{\rm ex} = 5\,\mathrm{K}$, the number of considered Gly-I and Gly-II transitions in the spectral line stacking reduces to two and 10, respectively, and the abundance upper limits increase to 5×10^{-10} and 3×10^{-11}. Conversely, for the higher excitation limit of $T_{\rm ex} = 10\,\mathrm{K}$, the number of considered Gly-I and Gly-II transitions increases to 18 and 16, respectively. The abundance upper limit of Gly-I remains at rounded 2×10^{-10}, while that of Gly-II decreases to 7×10^{-12}.

5.1 Glycine upper limits compared to other sources

Few previous attempts have been made to detect glycine towards cold low mass sources. The published upper limits we have identified

Table 4. Glycine upper limits (3σ) towards cold molecular cloud sources.

Source	Conformer	T_{ex} (K)	N_{upper} (cm^{-2})	$N_{upper}/N(H_2)$	Reference
L1544 Dust peak	Gly-I	5	5.8×10^{12}	1×10^{-10}	(1)
		10	3.3×10^{12}	6×10^{-11}	
L1544 Methanol peak	Gly-I	5	9.5×10^{12}	6×10^{-10}	(1)
		10	4.2×10^{12}	3×10^{-10}	
IRAS16293-2422	Gly-I	20	5.0×10^{12}	1×10^{-10}	(2)
L134	Gly-II	10	2.0×10^{12}	2×10^{-10}	(3), (4)[(a)]
TMC-1	Gly-II	7	3.0×10^{12}	2×10^{-10}	(5), (6)[(a)]
L183	Gly-II	7	4.5×10^{12}	2×10^{-10}	(5), (7)[(a)]

Notes (1) Jiménez-Serra et al. (2016); (2) Ceccarelli et al. (2000); (3) Snyder et al. (1983); (4) van der Werf et al. (1988); (5) Brown et al. (1979); (6) Spezzano et al. (2022); (7) Lattanzi et al. (2020)
(*a*) Reference for source H_2 column density.

are summarized in Table 4. 3σ upper limits[5] of Gly-II are reported for the dark clouds TMC-1 and L183 in Brown et al. (1979) as 3×10^{12} cm^{-2} and 4.5×10^{12} cm^{-2}, respectively, assuming $T_{ex} =$ 7 K for both sources. Another 3σ upper limit of Gly-II is reported in Snyder et al. (1983) for L134 as 2×10^{12} cm^{-2}, assuming $T_{ex} = 10$ K. Adopting the respective H_2 column densities towards TMC-1, L183, and L134 (2×10^{22}, 3×10^{22}, and 1×10^{22} cm^{-2}; van der Werf, Goss & Vanden Bout 1988; Lattanzi et al. 2020; Spezzano et al. 2022), the corresponding Gly-II abundance upper limits are presented in Table 4. Depending on the assumed excitation temperature at the B5 hotspot, the Gly-II abundance upper limit of this work is one to two orders of magnitude lower than those early estimates.

Jiménez-Serra et al. (2016) report two sets of 3σ upper limits for Gly-I towards the centre of the pre-stellar core L1544 and an offset position towards the shell-region where methanol emission is found to peak (see Table 4). The assumed excitation temperatures are 5 and 10 K. Based on typical COM excitation temperatures of ∼5–6 K, reported for the L1544 dust peak, the upper limit estimate for $T_{ex} = 5$ K might be better constrained at that position. It is on the same order than our Gly-I upper limit towards the B5 hotspot. At $T_{ex} = 10$ K, the upper limit at the L1544 dust peak becomes an order of magnitude lower than the limit at the B5 hotspot. Typical COM excitation temperatures at the L1544 methanol peak are reported as ∼5–8 K. At both excitation limits ($T_{ex} = 5$ and 10 K), the Gly-I abundance upper limit towards the B5 hotspot is slightly lower but on the same order as at the L1544 methanol peak. We note that the conditions at the L1544 methanol peak are presumably more similar to the B5 methanol hotspot than the conditions at the L1544 dust peak.

Another 3σ upper limit of Gly-I is reported for the cold (∼20 K) outer layer of the solar-type protostar IRAS16293-2422 in Ceccarelli et al. (2000) as 5×10^{12} cm^{-2}, i.e. 1×10^{-10} w.r.t. $N(H_2)$. The upper limit is obtained by averaging over three lines at around 101 GHz. However, the assumed excitation conditions in the envelope of IRAS16293-2422, though cold, are only marginally comparable to the case of the B5 hotspot because a difference of ≥10 K in excitation temperature is quite significant at low temperatures, and can change an upper limit by about an order of magnitude.

5.2 Glycine upper limits compared to COM abundances at the B5 hotspot

The acetaldehyde column density we derive in our study, i.e. $(2.0 \pm 0.6) \times 10^{12}$ cm^{-2}, is approximately 2.5 times lower than the estimate in Taquet et al. (2017), i.e. $(5.2 \pm 0.7) \times 10^{12}$ cm^{-2}. This discrepancy cannot be explained by the higher number of available data points for the rotation diagram analysis, but we are confident about the updated estimate.

The abundances of COMs relative to H_2 at the hotspot range from 2×10^{-10} for acetaldehyde and 4×10^{-10} for methyl formate to 2×10^{-8} for methanol; di-methyl ether is tentatively detected at 2×10^{-10} (Taquet et al. 2017). The most stringent, total abundance upper limit of glycine derived from the present observations (2×10^{-10} for $T_{ex} = 7.5$ K) is comparable to the abundance of the least abundant COM so far detected at the hotspot. Hence, given the present data, we can neither confirm nor rule out the presence of glycine in the gas phase at the B5 hotspot. If glycine is present but undetected, it is either less abundant than other COMs or has a more compact distribution or both.

6 CONCLUSIONS

Using the Onsala 20 m telescope, we performed a deep search for glycine towards the B5 methanol hotspot, which is a cold source ($T_k \approx 7.5$ K) with yet a significant amount of COMs in the gas phase (Taquet et al. 2017). We targeted several transitions of Gly-I and Gly-II in the frequency range ∼70–78 GHz. Our study is the first to search for a set of glycine transitions in this lower frequency range.

We did neither detect Gly-I nor Gly-II during our observations but derive sensitive upper limits for both conformers, using spectral line stacking and assuming LTE conditions and optically thin emission. Since, we did not detect glycine the hypothesis of a non-equilibrium Gly-II/Gly-I ratio similar to the case of *c*-HCOOH/*t*-HCOOH could not be tested. Our Gly-II upper limits towards the B5 hotspot are the most stringent obtained so far for a cold molecular cloud source. The obtained Gly-I limits are mostly on the same order as previously published limits towards comparable sources.

If glycine is present but undetected in the gas phase at the B5 hotspot it is either less abundant than other detected COMs in that source or has a more compact distribution or a combination thereof. We, therefore, do not rule out a future detection of glycine towards the B5 hotspot with higher-sensitivity instrumentation. Jiménez-Serra et al. (2014) calculate a detection limit of $\sim 1.5 \times 10^{-11}$ for glycine in cold molecular cloud sources. This limit has not yet been reached by any study searching for glycine.

ACKNOWLEDGEMENTS

The authors acknowledge support from Onsala Space Observatory for the provisioning of its facilities/observational support. The Onsala

[5]Reported are 2σ limits from which we derived 3σ values.

Space Observatory national research infrastructure is funded through Swedish Research Council grant No 2017-00648. This work was supported by Chalmers' Gender Initiative for Excellence (Genie) and the Goddard Center for Astrobiology. This research has made use of data from the Herschel Gould Belt Survey (HGBS) project (http://gouldbelt-herschel.cea.fr). The HGBS is a Herschel Key Programme jointly carried out by SPIRE Specialist Astronomy Group 3 (SAG 3), scientists of several institutes in the PACS Consortium (CEA Saclay, INAF-IFSI Rome and INAF-Arcetri, KU Leuven, MPIA Heidelberg), and scientists of the Herschel Science Center (HSC). We are grateful to Jose Aponte for preparing Fig. 1, to Henrik Olofsson for assistance with the observations and discussions regarding the data reduction, and to the anonymous reviewer whose comments helped to improve the content of the paper.

DATA AVAILABILITY

The data underlying this article will be shared on reasonable request to the corresponding author.

REFERENCES

Agúndez M., Marcelino N., Cernicharo J., Roueff E., Tafalla M., 2019, A&A, 625, A147
Altwegg K. et al., 2016, Sci. Adv., 2, e1600285
André P. et al., 2010, A&A, 518, L102
Bacmann A., Taquet V., Faure A., Kahane C., Ceccarelli C., 2012, A&A, 541, L12
Belitsky V. et al., 2015, A&A, 580, A29
Belloche A., Menten K., Comito C., Müller H. S. P., Schilke P., Ott J., Thorwirth S., Hieret C., 2008, A&A, 482, 179
Bernstein M., Dworkin J., Sandford S., Cooper G., Allamandola L., 2002, Nature, 416, 401
Berulis I., Winnewisser G., Krasnov V., Sorochenko R., 1985, Sov. Astron. Lett., 11, 251
Botta O., Glavin D., Kminek G., Bada J., 2002, Orig. Life Evol. Biosph., 32, 143
Brown R. et al., 1979, MNRAS, 186, 5P
Brown R., Godfrey P., Storey J., Bassez M., 1978, J. Chem. Soc. Chem. Commun., 13, 547
Ceccarelli C., Loinard L., Castets A., Faure A., Lefloch B., 2000, A&A, 355, 1129
Combes F., Rieu N.-Q., Wlodarczak G., 1996, A&A, 308, 618
Cronin J., Pizzarello S., 1999, Adv. Space Res., 23, 91
Cuadrado S., Goicoechea J. R., Roncero O., Aguado A., Tercero B., Cernicharo J., 2016, A&A, 596, L1
Cunningham M. et al., 2007, MNRAS, 376, 1201
Drozdovskaya M. N., van Dishoeck E. F., Rubin M., Jørgensen J. K., Altwegg K., 2019, MNRAS, 490, 50
Ehrenfreund P., Charnley S., 2000, ARA&A, 38, 483
Ehrenfreund P., Glavin D., Botta O., Cooper G., Bada J., 2001, Proc. Natl. Acad. Sci., 98, 2138
Elsila J., Glavin D., Dworkin J., 2009, Meteorit. Planet. Sci., 44, 1323
Enrique-Romero J., Rimola A., Ceccarelli C., Balucani N., 2016, MNRAS, 459, L6
Friberg P., Madden S., Hjalmarson A., Irvine W., 1988, A&A, 195, 281
García de la Concepción J. et al., 2022, A&A, 658, A150
Garrod R. T., Jin M., Matis K. A., Jones D., Willis E. R., Herbst E., 2022, ApJS, 259, 1
Garrod R., 2013, ApJ, 765, 29
Glavin D., Dworkin J., Aubrey A., Botta O., Doty J. H., Martins Z., Bada J. L., 2006, Meteorit. Planet. Sci., 41, 889
Goldsmith P. F., Langer W. D., 1999, ApJ, 517, 209
Goumans T., Uppal M., Brown W., 2008, MNRAS, 384, 1158
Guélin M., Brouillet N., Cernicharo J., Combes F., Wooten A., 2008, Astrophys. Space Sci., 313, 45
Guélin M., Cernicharo J., 1989, in Winnewisser G., Armstrong J., eds, Lecture Notes in Physics, Vol. 331, The Physics and Chemistry of Interstellar Molecular Clouds . Springer-Verlag, Berlin
Hadraoui K. et al., 2019, A&A, 630, 1
Hollis J., Pedelty J., Snyder L., Jewell P. R., Lovas F. J., Palmer P., Liu S.-Y., 2003a, ApJ, 588, 353
Hollis J., Pedelty J., Boboltz D., Liu S.-Y., Snyder L. E., Palmer P., Lovas F. J., Jewell P. R., 2003b, ApJ, 596, L235
Hollis J., Snyder L., Suenram R., Lovas F., 1980, ApJ, 241, 1001
Holtom P., Bennett C., Osamura Y., Mason N., Kaiser R., 2005, ApJ, 626, 940
Hoyle F., Wickramasinghe N., 1977, Nature, 270, 701
Ilyushin V., Alekseev E., Dyubko S., Motiyenko R., Lovas F., 2005, J. Mol. Spectrosc., 231, 15
Ioppolo S. et al., 2021, Nat. Astron., 5, 197
Jiménez-Serra I. et al., 2020, Astrobiology, 20, 1048
Jiménez-Serra I. et al., 2016, ApJL, 830, L6
Jiménez-Serra I., Testi L., Caselli P., Viti S., 2014, ApJL, 787, L33
Jones P., Cunningham M., Godfrey P., Cragg D., 2007, MNRAS, 374, 579
Kleiner I., Lovas F. J., Godefroid M., 1996, J. Phys. Chem. Ref. Data, 25, 1113
Koga T., Naraoka H., 2017, Sci. Rep., 7, 636
Kuan Y.-J., Charnley S., Huang H.-C., Tseng W.-L., Kisiel Z., 2003, ApJ, 593, 848
Kvenvolden K., Lawless J., Pering K., Peterson E., Flores J., Ponnamperuma C., Kaplan I. R., Moore C., 1970, Nature, 228, 923
Lattanzi V., Bizzocchi L., Vasyunin A. I., Harju J., Giuliano B. M., Vastel C., Caselli P., 2020, A&A, 633, A118
Lee C.-W., Kim J.-K., Moon E.-S., Minh Y., Kang H., 2009, ApJ, 697
Lovas F. J., Kawashima Y., Grabow J. U., Suenram R. D., Fraser G. T., Hirota E., 1995, ApJ, 455, L201
Marcelino N., Cernicharo J., Agúndez M., Roueff E., Gerin M., Martin-Pintado J., Mauersberger R., Thum C., 2007, ApJ, 665, L127
Matthews H., Friberg P., Irvine W., 1985, ApJ, 290, 609
Milam S. N., Savage C., Brewster M. A., Ziurys L. M., Wyckoff S., 2005, ApJ, 634, 1126
Müller H. S. P., Schlöder F., Stutzki J., Winnewisser G., 2005, J. Mol. Struct., 742, 215
Müller H. S. P., Thorwirth S., Roth D. A., Winnewisser G., 2001, A&A, 370, L49
Muñoz Caro G. et al., 2002, Nature, 416, 403
Naraoka H. et al., 2023, Science, 379, abn9033
Nummelin A., Dickens J. E., Bergman P., Hjalmarson A., Irvine W. M., Ikeda M., Ohishi M., 1998, A&A, 337, 275
Pickett H. M., Poynter R. L., Cohen E. A., Delitsky M. L., Pearson J. C., Müller H. S. P., 1998, JQSRT, 60, 883
Rimola A., Sodupe M., Ugliengo P., 2012, ApJ, 754, 24
Roy A. et al., 2014, A&A, 562, A138
Snyder L. et al., 2005, ApJ, 619, 914
Snyder L., Hollis J., Suenram R., Lovas F. J., Brown L. W., Buhl D., 1983, ApJ, 268, 123
Sorrell W., 2001, ApJ, 555, L129
Spezzano S. et al., 2022, A&A, 657, A10
Suenram R., Lovas F., 1978, J. Mol. Spectrosc., 72, 372
Suenram R., Lovas F., 1980, J. Am. Chem. Soc., 102, 9
Taquet V., Wirström E., Charnley S., Faure A., López-Sepulcre A., Persson C. M., 2017, A&A, 607, 14
van der Werf P. P., Goss W. M., Vanden Bout P. A., 1988, A&A, 201, 311
Vastel C., Ceccarelli C., Lefloch B., Bachiller R., 2014, ApJL, 795, 6
Walker G. W., Kalinauskaite E., McCarthy D. N., Trappe N. A., Murphy A., Helldner L., Pantaleev M. G., Flygare J., 2016, in Holland W. S., Zmuidzinas J., eds, SPIE Conf. Ser. Vol. 9914, Millimeter, Submillimeter, and Far-Infrared Detectors and Instrumentation for Astronomy VIII. SPI, Bellingham, p. 99142V
Wirström E., Charnley S. B., Persson C. M., Buckle J. V., Cordiner M. A., Takakuwa S., 2014, ApJL, 788, 6
Woon D., 2002, ApJ, 571, L177
Zucker C., Schlafly E. F., Speagle J. S., Green G. M., Portillo S. K. N., Finkbeiner D. P., Goodman A. A., 2018, ApJ, 869, 83

APPENDIX A: ADDITIONAL FIGURES

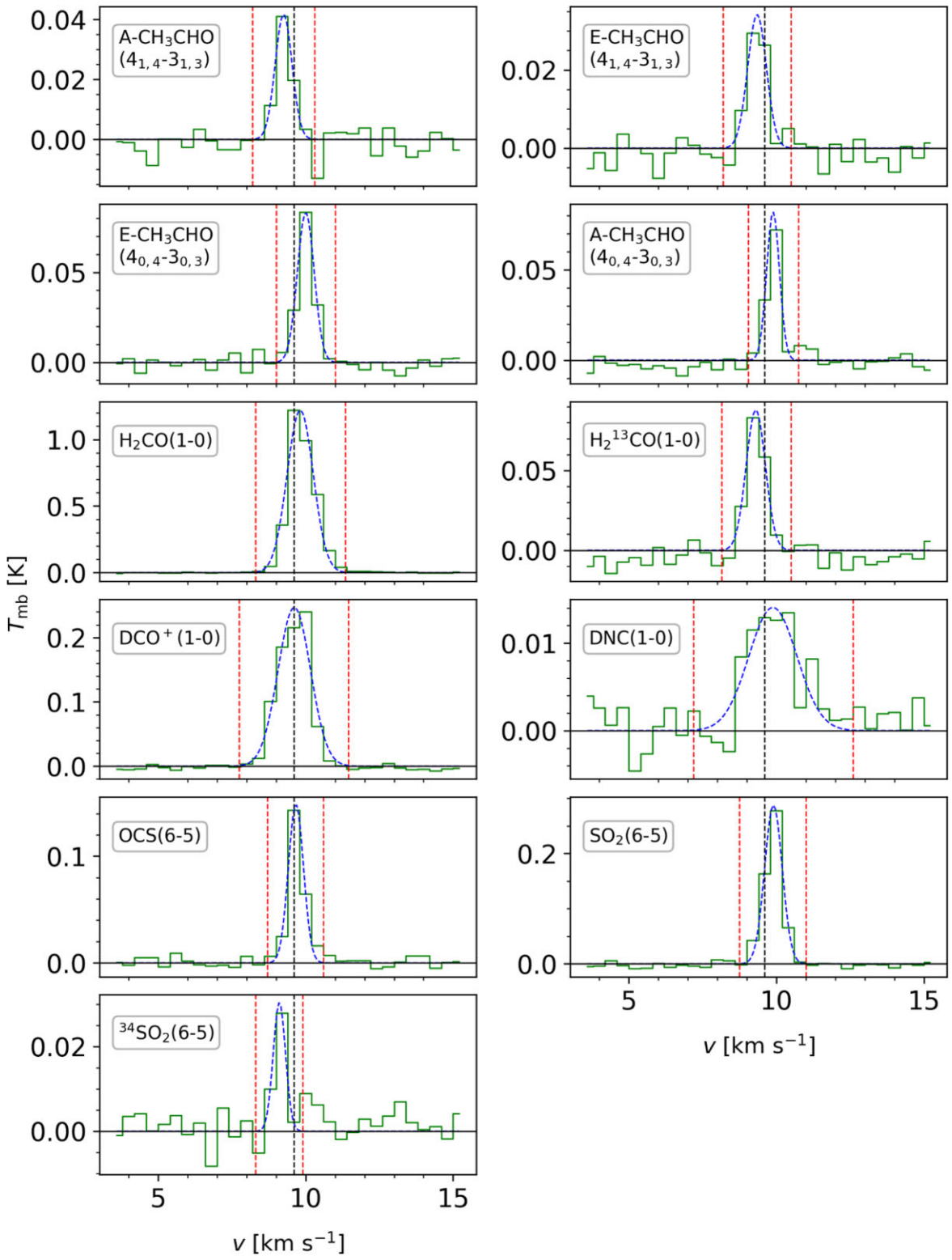

Figure A1. Spectral lines of non-targeted molecular transitions observed in the frequency range 70.2–77.9 GHz towards the B5 methanol hotspot. In all panels, the dashed blue line shows the Gaussian fit of the spectral line, and the dashed black line marks the LSR velocity of the hotspot. The dashed red lines mark the boundaries for the integrated intensity calculation.

Figure A2. Spectra around transition frequencies of targeted Gly-I transitions. The red regions mark the ranges for the calculation of the RMS noise temperature. The dashed black line marks the LSR velocity of the B5 methanol hotspot.

Figure A3. Spectra around transition frequencies of targeted Gly-II transitions. The red regions mark the ranges for the calculation of the RMS noise temperature. The dashed black line marks the LSR velocity of the B5 methanol hotspot.

This paper has been typeset from a TEX/LATEX file prepared by the author.